# DEVELOPMENT AND FUNCTIONAL CHARACTERIZATION OF COMPLEX IN VITRO MODELS OF THE BLOOD-BRAIN BARRIER

by

ADITYA BHALERAO

A dissertation submitted in partial fulfillment of the
requirements for the degree of

DOCTOR OF PHILOSOPHY IN BIOLOGICAL AND BIOMEDICAL SCIENCES

2025

Oakland University
Rochester, Michigan

Doctoral Advisory Committee:

Luca Cucullo, Ph.D., Chair
Zijuan Liu, Ph.D.
Mohamed Al-Shabrawey, Ph.D.

*To Snehal and Vihaan*

ACKNOWLEDGMENTS

First, I am deeply grateful to my advisor, Dr. Luca Cucullo, for his exceptional mentorship and unwavering support throughout my Ph.D. journey. He gave me the freedom to explore my ideas, encouraged me to take risks, and always stood by me during challenging times. His patience, guidance, and belief in my abilities have shaped me not only as a scientist but also as a person. I truly could not have asked for a better mentor.

I would also like to extend my sincere gratitude to my committee members, Dr. Liu and Dr. Al-Shabrawey, for their time and insightful feedback, which have contributed immensely to my academic growth. I am also deeply grateful for the opportunity to intern at GSK within the Complex In Vitro Models team. I thank my colleagues, Prabhakar, Prasanna, Sai, Madison, and others for their time, thoughtful feedback, and encouragement, which have been invaluable in strengthening my research and shaping the direction of this dissertation.

On a personal note, my deepest gratitude goes to my wife, Snehal, who believed in me, encouraged me, and made this journey possible. Her constant support, encouragement, and companionship have made the challenges lighter and the successes more meaningful. To my son, Vihaan, you have been my brightest source of joy and motivation. I am also deeply thankful to my parents and family for their unconditional love, prayers, and support across the miles. Finally, I would like to thank my dear friends, Sharavan and Itishree, who have been mentors, friends, and family to me throughout this journey.

- *Aditya Bhalerao*

# PREFACE

The blood-brain barrier (BBB) is a highly specialized and dynamic interface that preserves central nervous system homeostasis by regulating the selective transport of molecules between the brain and peripheral circulation. Its disruption is a defining feature of many neurological disorders, including viral infections, neurodegeneration, and cerebrovascular injury. However, progress in understanding BBB pathophysiology and developing effective therapeutic strategies has been constrained by the limitations of existing experimental models.

This dissertation, titled "*Development and Functional Characterization of Complex In Vitro Models of the Blood–Brain Barrier*", presents a series of studies aimed at advancing BBB modeling and functional assessment. The work encompasses the development of innovative in vitro systems, assay methodologies, and disease simulations designed to address critical challenges in the field.

*Chapter 1* introduces recent advances in the development of in vitro BBB models, highlighting the growing sophistication of culture systems, from traditional Transwell to microfluidic and organ-on-chip platforms. These evolving technologies provide an essential foundation for interrogating BBB function. In *Chapter 2*, I investigated the impact of HIV-1 gp120, a viral protein implicated in neuropathogenesis, and its role in disrupting BBB integrity. This work underscores the importance of modeling infection-driven neurovascular injury. *Chapter 3* details the design and characterization of a BBB-on-a-chip model, integrating multiple cell types and dynamic flow to more closely replicate physiological conditions. *Chapter 4* focuses on assay development for

permeability testing, providing a platform for evaluating the transport and functional delivery of BBB-targeted nanocarriers. Collectively, these studies contribute to the establishment of robust, human-relevant BBB models that enable mechanistic investigations, therapeutic screening, and translational applications. The approaches and findings presented in this dissertation aim to provide a foundation for future research focused on supporting drug discovery and development efforts for neurological disease.

# ABSTRACT

DEVELOPMENT AND FUNCTIONAL CHARACTERIZATION OF COMPLEX IN VITRO MODELS OF THE BLOOD-BRAIN BARRIER

by

Aditya Bhalerao

Adviser: Dr. Luca Cucullo, Ph.D.

The blood–brain barrier (BBB) is a specialized structure that protects the brain but also makes it difficult for many drugs to reach the central nervous system. To better understand how the BBB works and to develop ways to deliver treatments to the brain, researchers need reliable lab-based models that closely mimic how the barrier functions in the human body.

This dissertation focuses on developing, characterizing and functionally testing in-vitro models of the BBB using a combination of primary cells and cells derived from stem cells. The models include co-cultures of brain endothelial cells, astrocytes, and pericytes, which are important components of the neurovascular unit (NVU). A major part of the work involved developing a microfluidic chip-based model that allows the endothelial cells to grow under flow, simulating blood flow in the brain.

The model was tested for how well it could mimic natural barrier properties, including integrity, transport functions, and small molecule permeability. Compared to traditional methods, the new model showed better accuracy and could more reliably predict how drugs might behave in the human brain. We also tested our model's ability to support

studies on Central Nervous System (CNS) targeted therapeutic delivery via receptor-mediated transcytosis.

Overall, this work presents functional and translationally relevant BBB models that can be used to study brain diseases and test potential new treatments in the lab before moving to animal or human studies.

TABLE OF CONTENTS

LIST OF TABLES

LIST OF FIGURES

LIST OF ABBREVIATIONS

| | |
|---|---|
| BBB | Blood-Brain Barrier |
| CNS | Central Nervous System |
| NVU | Neurovascular Unit |
| EC | Endothelial Cells |
| TJ | Tight Junction |
| P-gp | P-glycoprotein |
| BCRP | Breast cancer resistance protein |
| MRPs | Multidrug resistance-related proteins |
| NADPH | Nicotinamide adenine dinucleotide phosphate |
| TBI | Traumatic Brain Injury |
| MS | Multiple Sclerosis |
| HTS | High Throughput Screening |
| SS | Shear Stress |
| TEER | Trans-Endothelial Electrical Resistance |
| DIV | Dynamic In Vitro |
| SOD | Superoxide Dismutase |
| APP | Amyloid precursor protein |
| PSEN1 | Presenilin 1 |
| HD | Huntington's Disease |
| PD | Parkinson's Disease |
| MPTP | 1-methyl-4-phenyl-1,2,3,6-tetrahydropyridine |
| ROI | Region of Interest |
| iPSC | induced Pluripotent Stem Cells |
| FITC | Fluorescein isothiocyanate |
| IVIVC | in vitro in vivo correlations |
| VEGF | Vascular endothelial growth factor |
| MALDI | Matrix-assisted laser desorption/ionization |
| HBMEC | Human brain microvascular endothelial cells |
| HBP | Human pericytes |
| HO | Human oligodendrocytes |
| HN | Human neurons |
| GLUT | Glucose transporter |
| ECM | Extracellular Matrix |
| RBE4 | Rat brain endothelial cells |
| HM | Human microglia |
| HA | Human astrocytes |
| CAD | Computer aided design |
| ABS | Acrylonitrile butadiene styrene |
| PLA | Polyactic acid |
| PA | Polyamide |
| PC | Polycarbonate |
| PTM | Printed Transfer Molding |
| FDM | Fused Deposition Modeling |

| | |
|---|---|
| SLA | Stereolithography |
| SLS | Selective Laser Sintering |
| DLP | Digital light processing |
| LDM | Liquid deposition modelling |
| FEAM | Fiber encapsulation additive manufacturing |
| BBB | Blood-Brain Barrier |
| NaF | Sodium fluorescein |
| 3D | 3 Dimensional |
| iBMECs | Human brain microvascular endothelial cells derived from iPSCs |
| UPLC | Ultra Performance Liquid Chromatography |
| LC-MS | Liquid chromatography and mass spectrometry |
| CsA | Cyclosporin A |
| α-SMA | Alpha-smooth muscle actin |
| GFAP | Glial fibrillary acidic protein |
| R123 | Rhodamine 123 |
| PDMS | Polydimethylsiloxane |
| ZO-1 | Zona Occludens-1 |
| ROS | Reactive oxygen species |
| HIV | Human Immunodeficiency Virus |
| AIDS | Acquired Immune Deficiency Syndrome |
| CVD | Cardiovascular disease |
| MTT | 3-(4,5-dimethylthiazol-2-yl)-2,5-diphenyltetrazolium bromide |
| PBS | Phosphate-buffered saline |
| BSA | Bovine serum albumin |
| NRF2 | Nuclear factor-E2 related Factor-2 |
| OCR | Oxygen consumption rate |
| AMT | absorptive-mediated transcytosis |
| RMT | receptor-mediated transcytosis |
| QC | Quality Control |
| TfR | Transferrin Receptor |
| CD98hc | Cluster of Differentiation 98 heavy chain |
| TEM | Transmission Electron Microscopy |
| ELISA | Enzyme-Linked Immunosorbent Assay |

# CHAPTER ONE

# INTRODUCTION TO THE BLOOD–BRAIN BARRIER AND ITS IN VITRO MODELING APPROACHES

The blood-brain barrier (BBB) is a fundamental component of the central nervous system. Its functional and structural integrity is vital in maintaining the homeostasis of the brain microenvironment. On the other hand, the BBB is also a major hindering obstacle for the delivery of effective therapies to treat disorders of the Central Nervous System (CNS). Over time, various model systems have been established to simulate the complexities of the BBB. The development of realistic in vitro BBB models that accurately mimic the physiological characteristics of the brain microcapillaries in situ is of fundamental importance not only in CNS drug discovery but also in translational research. The neurovascular unit (NVU) is the functional and structural ensemble of brain endothelial cells, pericytes, astrocytes, neurons, and extracellular matrix components that together regulate cerebral blood flow, maintain the BBB, and ensure proper neuronal function. Successful modeling of the NVU would provide an invaluable tool that would aid in dissecting out the pathological factors, mechanisms of action, and corresponding targets prodromal to the onset of CNS disorders. The field of BBB in vitro modeling has seen many radical changes in the last few years with the introduction of novel technologies and methods to improve existing models and develop new ones. The development of CNS organoids, organ-on-chip, spheroids, 3D printed microfluidics, and other innovative technologies have the potential to advance the field of BBB and NVU modeling. Therefore, in this chapter, we summarize the advances and progress in the design and application of functional BBB platforms in vitro with a particular focus on rapidly advancing technologies.

## Background: Structure and Functions of the BBB

The BBB consists of highly specialized vascular endothelial cells (EC) lining the brain micro vessels in juxtaposition with closely associated pericytes [1], extracellular matrix components, and astrocytic end-feet processes [2]. Along with other cells such as neurons and microglia, this cellular milieu modulates the BBB properties, supports its viability and functions [3]. At the brain microvascular level, the BBB functions as a highly dynamic and active interface between the systemic circulation and the CNS. The BBB maintains a stable brain environment to protect the CNS from unsolicited cells, bacteria, viruses, and potentially harmful substances (either endogenous or exogenous) apart from protecting against systemic fluctuations. The BBB also regulates the transport of essential molecules and nutrients necessary to maintain the optimal CNS environment and support neuronal activities [4]. The BBB responds to many physiological and pathological cues, including rheological changes [5], inflammatory stimuli, oxidative stress [6], diabetes, and hypercholesterolemia [7–10], acute brain injury [3], etc. The intrinsically unique and utmost complex functional interaction between the BBB endothelium and the surrounding cellular milieu (including astrocytes, pericytes, neurons, microglia, myocytes

as well as specialized cellular compartments such as endothelial glycocalyx [11, 12] has been termed "neurovascular unit" [2, 13]. In addition, the basement membrane, which exerts essential functions in cellular support and signal transduction, arises from the extracellular matrix (ECM) proteins secreted by ECs and astrocytes [14, 15]. Unlike their peripheral counterparts, the BBB endothelial cells are characterized by limited pinocytosis, the relative absence of fenestrations, and asymmetrical expression (lumen versus albumen) of trans-membrane transport and efflux systems regulating the traffic of substances between the blood and the brain parenchyma [16]. Transmembrane inter-endothelial TJ proteins (e.g., occludin, claudins, etc.) restrict the paracellular flux of ions and hydrophilic solutes across the BBB [17] resulting in high electrical resistance with readings≥1800 Ω $cm^2$; measured in situ in rats [18]. TJs also work as a "fence" that limits the free movement of lipids and proteins within the plasma membrane between the apical and the basal surface. Thus, water-soluble nutrients and other biologically vital substances (including amino acids, d-glucose, mono-carboxylic acids, etc. [16]. are delivered into the brain by specialized carrier-mediated transport systems [16] (see Fig. 1.1).

Furthermore, other prominent protein families, such as adherens junctions (AJ) and gap junctions (GJ), play significant roles in intercellular adhesion and communication, respectively, and are integral to BBB tightness [11]. In addition to the TJs, the BBB endothelium expresses a host of efflux transporters (including P-glycoprotein—Pgp [19], breast cancer resistance protein—BCRP [20], and multidrug resistance-related proteins MRPs [21] as well as cytochrome P450 (e.g., CYP3A4, NADPH-CYP P450 reductase, etc.) [22] and Phase II detoxifying enzymes (such as UGT1A4), which help protect the brain from potentially harmful substances [19]. However, on the negative side, the same defense mechanisms that protect the brain from harmful substances also present a major obstacle for drug delivery into the CNS. Recent studies have shown that approximately 98% of small-molecule and 100% of large molecule drugs cannot cross the BBB [23, 24]. Thus, the BBB is also a critical barrier hampering the treatment of major neurological disorders [25].

**BBB Dysfunction in Neurological Disorders**

Historically dysfunctions of the BBB are associated with the onset and progression of different neurological disorders including Alzheimer's disease [26], epilepsy [27], stroke [28, 29], multiple sclerosis [30], traumatic brain injury [31], amyotrophic lateral sclerosis [32] as well as schizophrenia [33]. Observed changes include alterations in BBB permeability [34, 35], caused by disruption and/ or structural alteration of TJ proteins [36]. This process can be associated with the degradation of the basement membrane [37] and altered expression of efflux pumps leading to the extravasation of plasma proteins [38, 39]. The effect can lead to the infiltration of serum components and immune cells into the CNS parenchyma, loss of CNS homeostasis, and damage to the surrounding brain tissue. Similar to stroke, traumatic brain injuries (TBIs) cause both immediate and delayed dysfunction of the BBB, leading to inflammation [40] and the rapid activation of the coagulation cascade [41]. In short, TBI can promote post-traumatic intravascular

coagulation followed by a significant reduction of blood flow in the pericontusional brain tissue, thus setting the stage for a condition closely resembling a post-ischemic injury. It is noteworthy to mention that in the case of several diseases, it is still debatable whether the disease conditions are caused due to a disruption of the BBB or whether the disruption of the BBB is the result of the disease condition (e.g., epilepsy). Even though BBB leakage is observed preclinically in most circumstances, the degree of leakage has been found to vary from widespread leakage to localized small leaks in different brain regions. By contrast, BBB dysfunction has been established as a critical early event in relapsing–remitting inflammatory MS progression [42, 43]. In comparison, BBB breakdown and enhanced permeability precede and leads to infiltration of encephalitogenic T cells, monocytes, and likely B cells into the brain. Furthermore, therapeutic options to improve the BBB have proven to limit MS disease progression [44, 45], thus establishing a robust cause-effect link between loss of BBB viability and MS.

**Translational Gap Between Animal Studies and Human Disease**

The widespread failures in clinical trials associated with neurological disorders have resulted in questions on whether the existing preclinical animal models are genuinely reflective of the human condition [46]. It is widely accepted that close interactions of pericyte, and brain endothelial cells are necessary for the optimal function of BBB [47]. However, Mihajlica et al. recently demonstrated that pericyte deficient mice ($Pdgfb^{ret/ret}$) produced similar values for $K_{in}$ for Diazepam, oxycodone, and paliperidone compared to control mice. There are no changes in the transport mechanisms between the diseased and control conditions. There are also significant discrepancies in animal models of different neurodegenerative and cerebrovascular disorders. In the case of Alzheimer's disease (AD), genetically engineered mice expressing the mutant genes for both APP and PSEN1 (here collectively termed APP/PS1 mice) yielded valuable insights into the mechanisms and consequences of amyloid deposition in the intact brain.

There are also reports where animal models of disease have shown no BBB disruptions in certain neurological disorders, whereas other studies have shown BBB disruptions in those specific disease models [48]. These conflicting findings simply raise more questions than answers. Recently, Nga-Bien Ly et al. reported that there is no difference in BBB integrity between wildtype control and humanized Alzheimer's disease animal models [49], whereas other groups' findings suggested otherwise [50, 51]. It should be noted that increased BBB permeability through gadolinium leakage was observed in the hippocampus of patients with mild cognitive impairment (MCI) and several grey and white matter regions in early Alzheimer's disease (AD) patients. However, the degree of disruption may vary from patient to patient, since only 25% of patients with MCI and 45–78% of early AD patients were found to have brain microbleeds [52–54]. In this respect, AD animal models have also had limited success in predicting clinical outcomes. It is now being argued that these disease models are mostly reflective of the asymptomatic phase of the disease [55]. In the case of amyotrophic lateral sclerosis (ALS), transgenic mice having a G39A mutant form of human superoxide dismutase (SOD1) showed no differences in permeability across disease model and wild type control groups for both

small molecule and large molecule markers [56]. Regarding Huntington's disease (HD), current rodent models provide a poor representation of the disease course and outcomes [57, 58]. Discrepancies related to animal models of different neurological disorders have been discussed below in brief:

*Alzheimer's disease (AD)* - Characterizing various forms of Mendelian dementia such as familial AD (FAD) mutations in the amyloid precursor protein (APP) or presenilin 1 (PSEN1) genes significantly improved our understanding of AD pathogenesis. Studies have also shown RAGE, and LRP balance plays a significant role in amyloid-beta transport into and out of the brain through the BBB [59]. A reduction in brain LRP levels may also play a role in amyloid-beta peptide accumulation [60]. Genetically engineered mice expressing the mutant genes for both APP and PSEN1 yielded essential insights into the mechanisms and consequences of amyloid deposition in the intact brain. However, to this day, the AD animal models have been unable to predict success in the clinic. For example, the Tg2576 model strain, which is based on a single FAD transgene, confirmed the relationship between amyloid pathology and impaired performance on cognitive tests in a preclinical experiment. Tg2576 mice have been improved or cured more than 300 times using different molecules. Yet none of these remarkable preclinical findings seem to transition to the clinical phase. It is now being argued that these disease models only helped address the early/ asymptomatic stage of the disease [55].

*Huntington's disease (HD)* - HD is an autosomal dominant inherited invariably fatal disorder. It results in mutated Huntington proteins that aggregate in different neurons. Over the course of the disease, there is significant neuronal cell loss, and patients show typical phenotypic hallmarks such as cognitive deficits, personality disorder, and hyperkinetic movements [61]. Studies have found that the BBB is disrupted in an animal model of HD (R6/2). Corresponding morphological changes were also observed in post-mortem tissues from human patients [62, 63]. Similar findings, however, are yet to be seen in live human subjects. To date, over 25 transgenic rodent models of HD have been used, yet none are able to effectively reproduce the neurodegeneration features and disease progression patterns that has been clinically observed [57, 58].

*Parkinson's disease (PD)* - This is a movement, and cognitive disorder with many pathologic hallmarks, including the formation of proteinaceous inclusions inside neurons, called Lewy Bodies and loss of dopaminergic neurons in the Substantia Nigra pars compacta [64]. PD has been found to be associated with multiple mutations. However, no single genetic anomaly was proven to be causing PD. The disease is thought to be linked to a range of polygenetic and environmental factors. 1-methyl-4-phenyl-1,2,3,6-tetrahydropyridine (MPTP) is a lipophilic compound and crosses the BBB easily and was found to induce symptoms and pathology of PD in animal models [65]. However, the injury-induced models mimic nigrostriatal dopamine deficiency but do not recapitulate the slow, progressive, and degenerative nature of the disease in humans. Whereas in clinical trials, the interventions are usually administered over a prolonged period of time, putative neuroprotective agents were being delivered at similar doses and schedules as an

acute Parkinson's disease-like lesion, which was induced in the typical underlying animal studies [66].

*Stroke* - Stroke incidence increases with age, and patients commonly have other comorbidities that might increase their stroke risk, which complicates the clinical progression and affect the functional outcome. Up to 75% of acute stroke patients have hypertension, and 68% have hyperglycemia as comorbidities [67]. On the contrary, only 10% of focal ischemia studies used animals having hypertension, and less than 1% used animals had induced diabetes. The preclinical studies also are mostly performed in young animals. This latter is because achieving appropriate infarct volumes in older animals as well as animals that have additional disease conditions using conventional techniques (such as middle cerebral artery occlusion) is quite tricky and prone to high variabilities. The animals used in different stroke models are usually young and mostly males. More than 95% of the studies were done on rodents. Larger animals that would be biologically closer to humans are rarely used [68]. Most preclinical studies also fail to acknowledge the delay between the identification of symptoms of stroke and the start of treatment, which is typically a couple of hours for most stroke patients. Also concerning the post-stroke assessment of BBB integrity as well as in other conditions where the integrity of the barrier might be compromised, gadolinium-based studies of microvascular integrity performed have shown limited sensitivity to detect low levels of extravasations across the BBB [69]. The facts discussed above highlight the urgent need to utilize technology that would better represent the disease conditions in humans.

**Beyond the Transwell: Dynamic Modeling and Measurement of BBB Permeability**

In recent years, significant steps had been taken toward developing physiological BBB-on-chip models. These recently described advanced microfluidic models provided 3D structure, cell–cell interaction, and the exposure to shear stress that resulted in better barrier function compared to conventional transwell models [70–73]. Moreover, they have characterized the dynamic permeability of drugs/markers, which make them more like in vivo permeability studies compared to the Transwell system [70, 72, 74]. However, there are still challenges ahead for developing in vitro model of BBB due to different designs of models and quantitative protocols. We can see the difference in the design and size of microchannels, shear stress, cell types, and permeability measurements in Table 1. Based on the versatility of BBB-on-chip technology, the comparison of these models would be complicated. The BBB maintains a unique homeostatic environment within the CNS and plays a critical role in mass transfer between the circulatory system and brain tissue. Therefore, permeability measurements in BBB on-chip models and data comparison with corresponding in vivo studies are usually performed as a means of understanding whether the model can surrogate for the in vivo study and whether an appropriate in vitro to in vivo correlation can be established. In the following part, we will provide more information regarding the process of measuring permeability in BBB-on-chips.

The permeability results of recent in vitro models have been reported in Table 1. Defining quantitative standards for barrier function is difficult for in vitro models since all quantitative data comes from animal models. The permeability values are described as the permeability coefficients of an analyte (cm/s) for passive transport. These values can be compared with in vivo values due to their independence to the analyte concentration, flow rate, and channel size. The values were obtained by injecting different molecular weight markers having fluorescent labels into the vascular channel and calculating mass conservation based on the number of fluorescent molecules outside the vessels. Equation (1) can be used to obtain the permeability of different fluorescent molecules for advanced 3D models.

$$p = (1 / \Delta I) * (V / A\_(surface)) * (dI/dt)$$

here, V is the tissue volume, A (surface) is the surface area of all vessels in the selected ROI (region of interest). ΔI is the maximum fluorescence intensity of the vascular channel, and (dI/dt) is the rate of increase in fluorescence intensity as solute exits into the tissue compartment. Afterward, the permeability coefficient of the endothelial barrier can be calculated from the measured permeability coefficient (P total) and the permeability coefficient measured in a device without endothelium P (blank) as follows.

$$P\_endo = (1 / P\_total) - (1 / P\_blank)$$

Therefore, the obtained endothelial permeability coefficient can be compared with other permeability coefficients of the same analyte in vivo or other platforms, including the Transwell system. Recently published studies related to the use of induced pluripotent stem cells (iPSC)-in microfluidic BBB platforms have found that these cells, under suitable culture conditions, temporarily developed into a BBB phenotype with permeability values close to that measured in vivo. In one study of tissue-engineered BBB micro vessels incorporating iPSC-derived human BMECs, the permeability of Lucifer yellow was reported to be $2–3\times10^{-7}$ cm/s [71] which was close to values reported in a rat model earlier [75]. In another study of a 3D self-organized microvascular model of the human BBB with endothelial cells, pericytes and astrocytes, the permeability 40 kDa FITC-dextran under mono-, co-, and tri-culture conditions were 6.6, 2.5, and $0.89\times10^{-7}$ cm/s, respectively. These results show that the presence of co and tri-culture reduces the permeability of analyte. Similar results were obtained for 10 kDa FITC-dextran: 12, 4.8, and $2.2\times10^{-7}$ cm/s, respectively. These values where comparable to those measured in vivo in rat cerebral microcirculation ($3.1\pm1.3\times10^{-7}$ cm/s for a 10 kDa FITC-dextran) [76], ($1.37\pm0.26\times10^{-7}$ cm/s for a 40 kDa FITC-dextran) [77]. Moreover, the permeability study of different molecular weight fluorescent-labeled dextran tracers in recent study of iPSC-BMECs in 3D microfluidic chip with presence of primary astrocyte and pericytes was deficient and the permeability values inversely correlated with the size of the tracer (average $P_{app}$=8.9, 1.1, and $0.24\times10^{-8}$ cm/s for 3, 10, and 70 kDa dextrans, respectively) [70]. The above studies indicate that the models are moving in the right direction for proper in vitro in vivo correlations (IVIVC), something that was not feasible utilizing the transwell systems. Based on the translational challenges as well

as ethical concerns and economic implications of small and large animal testing, it has become very crucial to develop a humanized BBB model encompassing the cell typologies represented in the NVU. These humanized models could help us properly understand changes in the NVU in disease conditions. There are also some reported devices trying to replicate the neurovascular unit and disease conditions [78–80]. However, we are still not there yet where we can produce diseased BBB conditions that will contain iPSC-derived endothelial cells, astrocytes, pericytes, and neurons in advanced in vitro models. Hopefully, with further improvements in techniques, we will be able to get there soon. Noteworthy is the fact that most research groups are still using large molecule Dextrans for measuring passive permeability, which technically should not be able to get into the BBB in vivo at all in naïve conditions. Only Searson's group recently reported a study utilizing Lucifer yellow and 10 kDa Dextran, where the 10 kDa Dextran did not permeate the barrier at all. There are some reports where the models have been used in conditions representing brain inflammation [70]. However, we still must improve these models further to effectively produce disease models that would perfectly represent in vivo conditions.

**Importance of Developing In Vitro Models of Human BBB**

To date, various in vitro BBB models have been developed and characterized in terms of barrier tightness, expression of BBB specific proteins, and usefulness for physiological and pharmacological studies [3, 81]. Traditionally the transwell systems utilizing immortalized endothelial cells were not producing tight barriers and had low TEER values. Higher molecular weight markers such as FITC dextran were used regularly for such systems since the lower molecular weight markers would pass through relatively quickly. As discussed earlier, animal models do not always recapitulate the human BBB physiology or a disease condition (including pathological characteristics such as onset, progression, etc.). Unavoidable interspecies differences are likely to play a major role. For example, works done by Terasaki et al., using QTAP technology clearly demonstrated that the mouse BBB is different from the human BBB [82]. Furthermore, intraspecies variabilities can equally impact data reproducibility thus affective the translational relevance of the results [83]. Tentative in vitro models based on immortalized human brain endothelial cells have also been proposed in static or dynamic conditions [40, 84]: these models recapitulate at least some of the expected characteristics of the BBB, like high level expression of BBB-expressed receptors and transporters. Therefore, "humanizing" the in vitro BBB platforms using human derived cells, may circumvent the translational limitations of current models and provide a complementary tool to support existing in vivo approaches. However, one of the major limiting factors to reproduce a "humanized" in vitro model to study neurological disease or disease state includes the availability of human brain tissues for cell isolation. This is quite difficult to procure and mostly originate from either post-mortem specimen (including fetal tissue) or patient-derived surgical resections. This latter, although may not represent the actual conditions in the native state.

Although most in vitro BBB models currently available are based on primary cultures of cerebral endothelial cells, endothelial progenitor cells (EPCs) might be other alternatives that present a specific phenotype of EC [85]. In these systems, cord blood-derived hematopoietic stem cells are used to generate a reproducible and stable human BBB model where the cells are initially differentiated into endothelial cells (ECs). Following the differentiation process, these ECs are then prompted to develop BBB properties by co-culture with pericytes [86]. These models were found to form much tighter barriers that can mimic human BBB integrity. However, there are still challenges ahead for developing the in vitro model of BBB due to different designs of models and quantitative protocols. Key features of recent microfluidic and 3D printed models of BBB has been summarized in Table 1. Although cell culture-based in vitro models are useful tools to study the regulatory mechanisms modulating the physiology and function of the BBB as well as assess the passage and transport mechanisms of putative brain penetrating drugs, reproducing the BBB properties in its entirety remains a significant and still unresolved challenge [87]. Different approaches have been used to mimic the BBB in vitro, and this includes static and dynamic (flow-capable) platforms, as well as the use of different cell types such as primary cells, immortalized cell lines, and, more recently, stem cells. In addition to using different cell types, cell cultures for BBB modeling have grown in structural complexity ranging from basic monocultures to multiple culture systems such as co-culture and tri-culture settings [17, 19]. The transwell system is one of the most commonly used tools as a BBB in vitro model. Although being very user-friendly and relatively easy to setup (Transwells also offer moderate scalability and high throughput screening—HTS—capabilities [40, 41]), there are substantial limitations inherent to the use of these platforms that need to consider. These include the two-dimensional structure, absence of enabling endothelial exposure to shear stress, and "edge effects" where areas of the transwell walls surrounding the membrane are intrinsically very permeable [41, 44, 45] (see Fig. 1.2a). Further technological advances were then introduced to enable exposure of the BBB endothelium to physiological shear stress (SS), whereas SS modulates endothelial morphology [88], but also their function and physiological responses paving the way toward the development of the so-called "Dynamic Models." Artificial hollow fiber constructs made of thermoplastic polymers such as polysulfone, polypropylene, etc., were initially used for the construction of brain micro vessels and other CNS vascular beds [89] where EC-glia co-culture could be arranged to mimic the spatial and topographical distribution of these cells in situ resembling the anatomy of brain micro vessels [90]. Under these controlled hemodynamic conditions combined with exposure to glial cells, ECs acquire more stringent BBB properties than those observed static platforms, including high TEER [40], cell polarization, and expression of specialized transporters [90] and efflux systems [40, 91] (see Fig. 1.2b). However, the enthusiasm for the add on advantages brought by this dynamic in vitro-BBB (DIV-BBB) platform is hampered by additional drawbacks inherent to its design and construction. Since the model relies on the use of capillary-like tubes structures surrounded by a larger enclosure, no practical way exists to monitor the cells cultured on or within the artificial micro vessels. The relatively large diameter of the capillaries compared to proper brain micro vessels was more representative of larger vascular beds like distal pre- and post-capillary segments. The DIV-BBB platform required a relatively large volume of

reagents and high quantities of cells (on the magnitude of $>10^6$) for culture initiation, thus affecting the cost, and the model per se does not have high throughput screening (HTS) capabilities. Furthermore, the system setup was quite complex, requiring a significant amount of time, resources, and technical skills than conventional platforms (e.g., Transwells) [91, 92]. Moreover, the most dynamic and realistic in vitro BBB model, microfluidic devices, requires specific equipment and technical skills mostly confined to the lab environment that developed the platform. These constraining factors, unfortunately, limit the adoption and further development of these models for basic and translational research [87] (see also Fig. 1.2c). In-silico models have also been developed to estimating structure–activity relationships for the BBB permeation of drug compounds based on their physicochemical properties [93–95]. Although these models are inexpensive, less time consuming, and high throughput screening methods for novel compounds in the drug discovery process, results obtained using computer simulation must be verified by in vivo experiments [96].

**Advances in BBB In Vitro Modeling**

*Organoids* - An organoid is an in vitro organotypic preparation consisting of various cells grown together under appropriate conditions to generate a miniature artificial version of an organ of interest, including the brain [97]. BBB organoids consist of human primary brain endothelial cells, astrocytes, and pericytes [98] assembling under low-adherence conditions into a multicellular structure resembling the blood–brain barrier [99]. One of the important characteristics of this model is that within the organoid, each of the cell types is directly in contact with one another, which plays a pivotal role in maintaining BBB integrity as well as function [100]. It has also been demonstrated from various studies that organoid shows better characteristics of BBB, which includes enhanced tight junctions, adherens junctions, and efflux pump expression compared to more traditional static culture systems. Additionally, lack of paracellular permeability, high drug efflux, and receptor-mediated transcytosis infer a realistic barrier function to the organoids [98]. Furthermore, using an organoid in vitro BBB model consisting of ECs, astrocytes, and pericytes, a recent study reported high expression of TJs proteins, VEGF dependent permeability, receptor-mediated transcytosis of angiopep-2, as well as activity of efflux pumps. On the other hand, the transwell model exhibited a lower level of BBB regulatory proteins, and the differentiation between the transportation of angiopep-2 and a control peptide was not possible. In this experiment, two different detection approaches, namely confocal fluorescence microscopy and MALDI mass spectrometry imaging, were used as a screening tool [98]. More recently, Pham et al. have developed a human vascularized cerebral organoid model utilizing a patient's iPSCs to study the BBB under normal and pathological conditions in health and disease [101]. To sum up, organoid BBB models seem to offer several advantages over other conventional in vitro BBB platforms, including but not limited to HTS due to ease of culture, simplicity, low requirement of reagents, and miniature size [87]. The throughput of this model can be further improved through integration with automated microscopy and robotics-assisted mass spectrometry technologies. Cost-effectiveness and reproducibility make this model more acceptable and attractive to implement in research as well. Considering the advantages offered by

BBB organoids-based in vitro models, it is evident that the technology provides an efficient method for studying drug transport through the BBB and practical support for the development of brain-targeting drugs for the treatment of CNS diseases [98]. Nevertheless, organoids have some limitations, as well. The issues of inter-samples variability and high processing time are not negligible. One of the critical drawbacks of organoids is the absence of essential types of cells, including glia, microglia, oligodendrocytes, vasculature, etc. Moreover, the timescale of human development, lack of microglia, regional inputs, and myelination may hinder neurons maturation, thus limiting its utilities for specific disease models [87, 102]. Furthermore, methods of barrier function analyses from two dimensional cultures will have to be adjusted to the analysis of 3D organoid structures. Few attempts have been made to develop this methodology to assess the permeability of a compound in a 3D organoid and so far, these methods have been primarily developed for measurements of the barrier permeability in intestinal organoids [103].

*Human Cortex Spheroids* - Focusing on the drawbacks of conventional organoid in vitro BBB model, recently, the development of a 3D spheroid model of BBB has been reported. This model more closely mimics the human brain tissue since it is comprised of six cell types found within the brain cortex. These cell types include human brain microvascular endothelial cells (HBMEC), human pericytes (HBVP), human astrocytes (HA), human microglia (HM), human oligodendrocytes (HO) and human neurons (HN), with endothelial cells enclosing the brain parenchymal cells. Induced pluripotent stem cells (iPSC) were used to derive the cells which could help narrow the gap in achieving an ideal in vitro BBB model for clinical applications in studies aimed to understand neurological diseases. Interaction between BBB and adjacent brain cells provides a platform to evaluate the ability of a novel drug to cross the BBB and its effect on microglia, oligodendrocytes as well as neurons, which is crucial for studying neurodegenerative conditions including amyotrophic lateral sclerosis, multiple sclerosis, stroke, Alzheimer's disease. High cell viability was found to be maintained up to 21 days in the spheroid model containing six cell types, which is useful in evaluating long term effects of drug toxicity [104]. Expression of P-gp and GLUT-1 proteins were also identified as these proteins have a pivotal role in expelling unwanted chemical from the brain tissue and transport glucose into the brain tissue respectively and abnormalities in these proteins lead to different diseases [104–107]. Expression of tight junctions, adherens junctions, and proteins associated with adherens junction was also identified to avert the free paracellular diffusion of substances into the brain parenchyma. Additionally, it was also found that tight and adherens junction protein localization was disrupted by hypoxia, thus supporting the usefulness of this model to study ischemia. BBB selectivity was also evaluated by measuring the effect of mercury ions in brain parenchyma by assessing cell viability [104]. Considering the characteristics and features of this model, we can state that, human cortex spheroid in vitro BBB model may provide some additional advantages over conventional organoids and can be a suitable platform for studies related to drug discovery, disease modeling, and neurotoxicity. However, further structural consideration to identify the production and proper deposition of extracellular matrix proteins of BBB and analysis of effects on individual cell types to

evaluate cell-specific function is needed, which will make this model more acceptable to study different neurological diseases [104]. A more comprehensive description of CNS-related organoid models, including similar techniques, protocols, use, and limitations, has been recently published by Pacitti et al. elsewhere [101].

*3D ECM-based Models* - One of the significant hurdles in the field of in vitro modeling that current technologies have been trying to overcome is that of providing a quasi-physiological microenvironment to promote the BBB development of realistic physiological properties and responses to endogenous as well as exogenous stimuli [108, 109]. 3D in vitro tissue models are currently available for a variety of organs and tissues (including muscle, bone, liver, and cardiac tissues) [110]. The use of this technology is now making a modest appearance in cerebrovascular and BBB research, as well. In the specific case, the brain microcapillaries are grown on self-polymerizing extracellular matrix protein (ECM) scaffolds where the BBB cellular components can develop close interactions with one another while being exposed to trophic factors along quasi-physiological biochemical gradients (see Fig. 1.3). High-resolution confocal microscopy and/or other 3D imaging techniques such as multiphoton microscopy and optical coherence tomography can be used to monitor the dynamic changes of cells cultured in the 3D ECM microenvironments. However, the adoption of this technology in BBB research is still limited due to the complexity of developing an in vivo-like matrix architecture, where the omission of even minor ECM constituents can potentially alter the matrix property and thus architectural assembly processes of the microvasculature. These platforms are currently confined to basic research with relatively low translational/pharmaceutical appeal due to several factors including high complexity, lack of HTS capabilities, consistent reproducibility, etc.

*Microfluidics via 3D printing* - In recent years, in the field of biomedical research, microfluidics has emerged as a promising alternative due to its high throughput, automation capabilities, and low fabrication and operation costs [111]. However, current microfluidic devices have relied on multi-step lithographic processes, which are time-consuming and complicated. In order to solve this critical issue, currently, 3D-printing (additive manufacturing) is becoming an alternative approach to microfluidic fabrication with complex architectures, avoiding multi-step processing with a wide range of materials [112–114]. In fact, 3D printing, as digital fabrication technology, is a process of adding elements to fabricate objects from 3D model data, layer by layer, enabling precise construction of complex objects directly from a computer-aided design (CAD) software [115]. Indeed, 3D printed microfluidic technology provides researchers with several advantages over traditional fabrication techniques including the ability to build channels with unprecedented shape and complexity that are uniform and reproducible at minimal operating cost and time (reduced from weeks to a few hours), product complexity, reduction of user error, precisely controlled size, interconnectivity and geometry, flexibility and throughput [112, 116–118]. A similar procedure is used in most 3D printing processes for manufacturing solid structures from digital designs. Briefly, the intended product is digitally rendered in 3D with computer-aided design (CAD) software, and then 3D designs are converted to the stereolithography file format (STL), describing

the external surface of a 3D model [116]. The data is then further sliced into a build file of 2D layers and sent to the 3D printing machine [115]. Raw materials such as thermoplastic polymers (including acrylonitrile butadiene styrene—ABS, polylactic acid—PLA, polyamide—PA, and polycarbonate PC), natural polymers, and biocompatible synthetic polymers [114, 116, 119–123] are processed into filaments or granules. Then binder solutions are added and solidified automatically in a layer-by-layer manner to produce the desired product. After printing, products may require polishing, drying, sintering, or other post-processing steps. Unprinted materials will also be harvested and recycled for continued use in the printing process [124]. Various printing techniques have been utilized for microfluidic applications. The leading 3D set up processes for microfluidic systems are 3D Printed Transfer Molding (PTM), Fused Deposition Modeling (FDM), Stereolithography (SLA), Direct Ink Writing, and Selective Laser Sintering (SLS) [124–126]. Recently, several new techniques have been developed for 3D printing, including Poly jet, digital light processing (DLP), liquid deposition modeling (LDM), and fiber encapsulation additive manufacturing (FEAM) [127– 130]. Although these methods have more material selections or less processing time, only a few studies have been conducted to assess the viability of these techniques to manufacture microfluidic systems, due to their high cost and complexity compared to traditional 3D printing methods. A more comprehensive description of 3D printing techniques, protocols, use, and limitations has also been recently published by Sivandzade et al. elsewhere [22]. Despite the potential advantages provided by 3D printing fabrication processes in BBB modeling, the technology is not yet mature, with several limitations that still hinder its widespread adoption. For example, the lack of high-throughput 3D-bioprinted tissue models for research makes this technology not yet suitable for drug discovery and toxicology studies. The complexity of the tissue to be reproduced increases exponentially the complexity of the technical challenges that need to be overcome. These include conjugating multiple elements such as fabrication materials, cell types, cell distribution as well as loading of the necessary biological factors to maintain cell viability, and construction of the tissue scaffold itself. However, to advance this up and coming technology, any further will require the integration of multiple fields of research, including engineering, biomaterials science, cell biology, physics, and medicine. An additional variable to consider (and a potential challenge) for the development of viable and clinically relevant in vitro model is the type of cells used in the setup. More specifically, whether these are primary cells, cell lines, or induced pluripotent stem cells (which are then differentiated into the desired phenotype), each type of cell has advantages and disadvantages, which are analyzed below.

**Advantages and Disadvantages of Cell Lines and Primary Cultures**

Animal and human-derived cell lines have been developed as biological surrogates for BBB modeling. One attractive feature of these cells over primary cultures is their relative affordability and (to some extent) their capability of retaining their differentiating properties over multiple passages. Only a few immortalized human endothelial cell lines (HCMEC/D3 [84], HMEC-1 [131], TY08 [132], hBMEC [133], and BB19 [134]) have been developed and reported in BBB modeling. Highly purified populations of cultured

human brain (human brain microvascular endothelial cells—HBMEC), unfortunately, are quite expensive if acquired from commercial sources. Unfortunately, the high level of technical skill necessary to isolate these cells as well as long term viability after few passages makes their use limited to few laboratories in the field. Isolation of these cells from the native brain tissue also requires advanced technical skills (isolation and purification processes are labor-intensive), time, and a viable source. Human specimens provide features specific to a variety of neurological etiologies that otherwise would be near impossible to recapitulate in cell lines or animal brain-derived (rodent, porcine, or bovine) primary cultures. However, primary cells may provide an attractive alternative in a sophisticated set-up. Regarding Spheroid, hBMEC, pericytes, and astrocytes spontaneously form into a multicellular spheroid in co-culture under low-adherence conditions and self-assemble into a modular organization that resembles the BBB [98]. Needless to say, spheroids provide each cell type to interact with one another, which has been reported to play a pivotal role in the maintenance of BBB integrity and function [99]. In the microfluidic platform, hBMEC might be superior due to its shallow cell requirement.

**Human-induced Pluripotent Stem Cells (hiPSCs)**

Even though HBMECs are not yet a realistic (cost-effective) alternative to the use of cell lines for industrial (pharmaceutical) screening (such as testing permeability, toxicity, etc.) and testing of novel drugs, they have unmatched value for basic and translational research. Next to these primary cells, recent advancement in the field of BBB modeling has brought forward the use of human iPSCs [135, 136]. In recent years, with improvements in understanding of differentiation pathways, induced Pluripotent stem cells (iPSCs) are now regularly differentiated to different cell types for co-culture models in microfluidic devices as well as 3D printed models [137]. 3D structure, cell–cell interaction, and the exposure of shear stress result in better barrier function compared to conventional transwell models. iPSCs-based BBB models are the first human BBB models with in vivo like paracellular barrier properties [138]. Thus, these cells may hold enormous potential for the development of preclinical disease models as well as species-dependent differences [139]. The unique advantage of using iPSCs is their ability to generate a representative model of patients from which they have been originated [140]. Additionally, recent advances in gene editing techniques provide exciting opportunities in disease modeling using iPSCs, although these methods still have hindrances like epigenetic reprogramming and loss of patient-specific epigenetic signature [141]. iPSCs technology has some major limitations so that the risk of tumor formation is present due to the use of viral infections and low efficiency of reprogramming during the production of these cells. [142]. On the other hand, an existing limitation of the model is the narrow experimental window provided by iPSC-derived cells, which generally tend to de-differentiate quite rapidly under in vitro culture conditions. Moreover, the cell differential procedure depends upon various random and permanent insertion of transcription factors. Overall, iPSCs- could be applied in the construction of 3D models such as spheroids or organoids in order to support the development of a brain vasculature within these models [139]. Other future 3D models based on iPSCs might use cultivation in or on plastic

scaffolds or hydrogels with defined 3D structures. Further development in the field and specifically in the cell differentiation processes and culture stabilization will undoubtedly further the availability and use of these cells in this and other fields of research.

## REFERENCES


1. Shimizu F, Nishihara H, Kanda T. Blood–brain barrier dysfunction in immuno-mediated neurological diseases. Immunol Med. 2018;41(3):120–8.
2. Abbott NJ. Blood–brain barrier structure and function and the challenges for CNS drug delivery. J Inherit Metab Dis. 2013;36(3):437–49.
3. Abbott NJ, et al. Structure and function of the blood–brain barrier. Neurobiol Dis. 2010;37(1):13–25.
4. Fernández-López D, et al. Blood–brain barrier permeability is increased after acute adult stroke but not neonatal stroke in the rat. J Neurosci. 2012;32(28):9588–600.
5. Cai Z, et al. Role of blood–brain barrier in Alzheimer's disease. J Alzheimer's Dis. 2018;63(4):1223–34.
6. Vargas-Osorio Z, et al. Multifunctional superparamagnetic stiff nanoreservoirs for blood brain barrier applications. Nanomaterials. 2019;9(3):449.
7. Van Dyken P, Lacoste B. Impact of metabolic syndrome on neuroinflammation and the blood–brain barrier. Front Neurosci. 2018;12:930.
8. Prasad S, et al. Impact of cigarette smoke extract and hyperglycemic conditions on blood–brain barrier endothelial cells. Fluids Barriers CNS. 2015;12:18.
9. Prasad S, et al. Diabetes mellitus and blood–brain barrier dysfunction: an overview. J Pharmacovigil. 2014;2(2):125.
10. Acharya NK, et al. Diabetes and hypercholesterolemia increase blood–brain barrier permeability and brain amyloid deposition: beneficial effects of the LpPLA2 inhibitor darapladib. J Alzheimers Dis. 2013;35(1):179–98.
11. Stamatovic SM, et al. Junctional proteins of the blood–brain barrier: new insights into function and dysfunction. Tissue Barriers. 2016;4(1):e1154641.
12. Abdullahi W, Tripathi D, Ronaldson PT. Blood–brain barrier dysfunction in ischemic stroke: targeting tight junctions and transporters for vascular protection. Am J Physiol Cell Physiol. 2018;315(3):C343–56.
13. Sivandzade F, Bhalerao A, Cucullo L. Cerebrovascular and neurological disorders: protective role of NRF2. Int J Mol Sci. 2019;20(14):3433.
14. Baeten KM, Akassoglou K. Extracellular matrix and matrix receptors in blood–brain barrier formation and stroke. Dev Neurobiol. 2011;71(11):1018–39.
15. Xu L, Nirwane A, Yao Y. Basement membrane and blood–brain barrier. Stroke Vasc Neurol. 2019;4(2):78–82.
16. Li J, et al. Mild hypothermia alleviates brain oedema and blood–brain barrier disruption by attenuating tight junction and adherens junction breakdown in a swine model of cardiopulmonary resuscitation. PLoS ONE. 2017;12(3):e0174596.
17. Gomes MJ, et al. Cell-based in vitro models for studying blood–brain barrier (BBB) permeability. Concepts and models for drug permeability studies. Amsterdam: Elsevier; 2016. p. 169–88.
18. Butt AM. Effect of inflammatory agents on electrical resistance across the blood–brain barrier in pial microvessels of anaesthetized rats. Brain Res. 1995;696(1–2):145–50.
19. Kaisar MA, et al. New experimental models of the blood–brain barrier for CNS drug discovery. Expert Opin Drug Discov. 2017;12(1):89–103.
20. Galla H-J. Monocultures of primary porcine brain capillary endothelial cells: still a functional in vitro model for the blood-brain-barrier. J Control Release. 2018;285:172–7. 21. Alluri H, et al. A mouse controlled cortical impact model of traumatic brain injury for studying blood–brain barrier dysfunctions. Traumatic and ischemic injury. Berlin: Springer; 2018. p. 37–52.
22. Sivandzade F, et al. NRF2 and NF-B interplay in cerebrovascular and neurodegenerative disorders: molecular mechanisms and possible therapeutic approaches. Redox Biol. 2019;21:101059.
23. Helms HC, et al. In vitro models of the blood–brain barrier: an overview of commonly used brain endothelial cell culture models and guidelines for their use. J Cereb Blood Flow Metab. 2016;36(5):862–90.

24. Pardridge WM. Drug transport across the blood–brain barrier. J Cereb Blood Flow Metab. 2012;32(11):1959–72.
25. Agoston DV. Bench-to-bedside and bedside back to the bench; seeking a better understanding of the acute pathophysiological process in severe traumatic brain injury. Front Neurol. 2015;6:47.
26. Grammas P. A damaged microcirculation contributes to neuronal cell death in Alzheimer's disease. Neurobiol Aging. 2000;21(2):199–205.
27. van Vliet EA, et al. Blood–brain barrier leakage may lead to progression of temporal lobe epilepsy. Brain. 2007;130(Pt 2):521–34.
28. Kuroiwa T, et al. The biphasic opening of the blood–brain barrier to proteins following temporary middle cerebral artery occlusion. Acta Neuropathol. 1985;68(2):122–9.
29. Hornig CR, et al. Changes in CSF blood–brain barrier parameters in ischaemic cerebral infarction. J Neurol. 1983;229(1):11–6.
30. Zivadinov R, Alexander SJ, Minagar A. Vascular pathology of multiple sclerosis. Neurol Res. 2012;34(8):735–7.
31. Logsdon AF, et al. Role of microvascular disruption in brain damage from traumatic brain injury. Compr Physiol. 2015;5(3):1147–60.
32. Zhong Z, et al. ALS-causing SOD1 mutants generate vascular changes prior to motor neuron degeneration. Nat Neurosci. 2008;11(4):420–2.
33. Greene C, et al. Dose-dependent expression of claudin-5 is a modifying factor in schizophrenia. Mol Psychiatry 2018;23(11):2156–66.
34. Zenaro E, Piacentino G, Constantin G. The blood–brain barrier in Alzheimer's disease. Neurobiol Dis. 2017;107:41–56.
35. Eichler AF, et al. The biology of brain metastases—translation to new therapies. Nat Rev Clin Oncol. 2011;8(6):344.
36. Barrette AM, Bouhaddou M, Birtwistle MR. Integrating transcriptomic data with mechanistic systems pharmacology models for virtual drug combination trials. ACS Chem Neurosci. 2017;9(1):118–29.
37. Moya ML, et al. A reconfigurable in vitro model for studying the blood–brain barrier. Ann Biomed Eng. 2019;48(2):780–793. https://doi. org/10.1007/s10439-019-02405-y.
38. Chen Y, Liu L. Modern methods for delivery of drugs across the blood– brain barrier. Adv Drug Deliv Rev. 2012;64(7):640–65.
39. Sweeney MD, Sagare AP, Zlokovic BV. Blood–brain barrier breakdown in Alzheimer disease and other neurodegenerative disorders. Nat Rev Neurol. 2018;14(3):133.
40. Cucullo L, et al. Immortalized human brain endothelial cells and flow-based vascular modeling: a marriage of convenience for rational neurovascular studies. J Cereb Blood Flow Metab. 2008;28(2):312–28.
41. Cucullo L, et al. The role of shear stress in Blood–Brain Barrier endothelial physiology. BMC Neurosci. 2011;12(1):40.
42. Revesz T, et al. A comparison of the pathology of primary and secondary progressive multiple sclerosis. Brain. 1994;117(4):759–65.
43. Kamphuis WW, et al. The blood–brain barrier in multiple sclerosis: microRNAs as key regulators. CNS Neurol Disord Drug Targets. 2015;14(2):157–67.
44. Hudecz D, et al. Reproducibility in biological models of the blood– brain barrier. Eur J Nanomed. 2014;6(3):185–93.
45. Czupalla CJ, Liebner S, Devraj K. In vitro models of the blood–brain barrier. Cerebral angiogenesis. Berlin: Springer; 2014. p. 415–37.
46. van der Worp HB, et al. Can animal models of disease reliably inform human studies? PLoS Med. 2010;7(3):e1000245.
47. Sweeney MD, Ayyadurai S, Zlokovic BV. Pericytes of the neurovascular unit: key functions and signaling pathways. Nat Neurosci. 2016;19(6):771–83.
48. Mihajlica N, Betsholtz C, Hammarlund-Udenaes M. Rate of smallmolecular drug transport across the blood–brain barrier in a pericyte-deficient state. Eur J Pharm Sci. 2018;124:182–7.
49. Bien-Ly N, et al. Lack of widespread BBB disruption in Alzheimer's disease models: focus on therapeutic antibodies. Neuron. 2015;88(2):289–97.

50. Hartz AM, et al. Amyloid-beta contributes to blood–brain barrier leakage in transgenic human amyloid precursor protein mice and in humans with cerebral amyloid angiopathy. Stroke. 2012;43(2):514–23.
51. Bell RD, et al. Apolipoprotein E controls cerebrovascular integrity via cyclophilin A. Nature. 2012;485(7399):512–6.
52. van de Haar HJ, et al. Neurovascular unit impairment in early Alzheimer's disease measured with magnetic resonance imaging. Neurobiol Aging. 2016;45:190–6.
53. van de Haar HJ, et al. Blood–brain barrier leakage in patients with early Alzheimer disease. Radiology. 2016;281(2):527–35.
54. Montagne A, et al. Brain imaging of neurovascular dysfunction in Alzheimer's disease. Acta Neuropathol. 2016;131(5):687–707.
55. Zahs KR, Ashe KH. 'Too much good news'—are Alzheimer mouse models trying to tell us how to prevent, not cure, Alzheimer's disease? Trends Neurosci. 2010;33(8):381–9.
56. Boswell CA, et al. Vascular physiology and protein disposition in a preclinical model of neurodegeneration. Mol Pharm. 2013;10(5):1514–21.
57. Pouladi MA, Morton AJ, Hayden MR. Choosing an animal model for the study of Huntington's disease. Nat Rev Neurosci. 2013;14(10):708–21.
58. Chang R, et al. Transgenic animal models for study of the pathogenesis of Huntington's disease and therapy. Drug Des Dev Ther. 2015;9:2179–88.
59. Deane R, Wu Z, Zlokovic BV. RAGE (yin) versus LRP (yang) balance regulates alzheimer amyloid beta-peptide clearance through transport across the blood–brain barrier. Stroke. 2004;35(11 Suppl 1):2628–31.
60. Deane R, Sagare A, Zlokovic BV. The role of the cell surface LRP and soluble LRP in blood–brain barrier Abeta clearance in Alzheimer's disease. Curr Pharm Des. 2008;14(16):1601–5.
61. Howland DS, Munoz-Sanjuan I. Mind the gap: models in multiple species needed for therapeutic development in Huntington's disease. Mov Disord. 2014;29(11):1397–403.
62. Drouin-Ouellet J, et al. Cerebrovascular and blood–brain barrier impairments in Huntington's disease: potential implications for its pathophysiology. Ann Neurol. 2015;78(2):160–77.
63. Di Pardo A, et al. Impairment of blood–brain barrier is an early event in R6/2 mouse model of Huntington Disease. Sci Rep. 2017;7:41316.
64. Jagmag SA, et al. Evaluation of models of Parkinson's disease. Front Neurosci. 2015;9:503.
65. Mikkelsen M, et al. MPTP-induced Parkinsonism in minipigs: a behavioral, biochemical, and histological study. Neurotoxicol Teratol. 1999;21(2):169–75.
66. Kimmelman J, et al. Launching invasive, first-in-human trials against Parkinson's disease: ethical considerations. Mov Disord. 2009;24(13):1893–901.
67. van der Worp HB, Raaijmakers TW, Kappelle LJ. Early complications of ischemic stroke. Curr Treat Options Neurol. 2008;10(6):440–9.
68. Sena E, et al. How can we improve the pre-clinical development of drugs for stroke? Trends Neurosci. 2007;30(9):433–9.
69. Choi JW, Moon WJ. Gadolinium deposition in the brain: current updates. Korean J Radiol. 2019;20(1):134–47.
70. Park TE, et al. Hypoxia-enhanced Blood–Brain Barrier Chip recapitulates human barrier function and shuttling of drugs and antibodies. Nat Commun. 2019;10(1):2621.
71. Linville RM, et al. Human iPSC-derived blood–brain barrier microvessels: validation of barrier function and endothelial cell behavior. Biomaterials. 2019;190–191:24–37.
72. Wang YI, Abaci HE, Shuler ML. Microfluidic blood–brain barrier model provides in vivo-like barrier properties for drug permeability screening. Biotechnol Bioeng. 2017;114(1):184–94.
73. Adriani G, et al. A 3D neurovascular microfluidic model consisting of neurons, astrocytes and cerebral endothelial cells as a blood–brain barrier. Lab Chip. 2017;17(3):448–59.
74. Modarres HP, et al. In vitro models and systems for evaluating the dynamics of drug delivery to the healthy and diseased brain. J Control Release. 2018;273:108–30.
75. Easton AS, Sarker MH, Fraser PA. Two components of blood–brain barrier disruption in the rat. J Physiol. 1997;503(Pt 3):613–23.
76. Yuan W, et al. Non-invasive measurement of solute permeability in cerebral microvessels of the rat. Microvasc Res. 2009;77(2):166–73.

77. Shi L, et al. Quantification of blood–brain barrier solute permeability and brain transport by multiphoton microscopy. J Biomech Eng. 2014;136(3):031005.
78. Vatine GD, et al. Modeling psychomotor retardation using iPSCs from MCT8-deficient patients indicates a prominent role for the blood–brain barrier. Cell Stem Cell. 2017;20(6):831–843.e5.
79. Shin Y, et al. Blood–brain barrier dysfunction in a 3D in vitro model of Alzheimer's disease. Adv Sci. 2019;6(20):1900962.
80. Vatine GD, et al. iPSC-derived blood–brain barrier chips enable disease modeling and personalized medicine applications. Cell Stem Cell. 2019;24(6):995–1005.e6.
81. Wilhelm I, Krizbai IA. In vitro models of the blood–brain barrier for the study of drug delivery to the brain. Mol Pharm. 2014;11(7):1949–63.
82. Uchida Y, et al. Quantitative targeted absolute proteomics of human blood–brain barrier transporters and receptors. J Neurochem. 2011;117(2):333–45.
83. Uchida Y, et al. A study protocol for quantitative targeted absolute proteomics (QTAP) by LC-MS/MS: application for inter-strain differences in protein expression levels of transporters, receptors, claudin-5, and marker proteins at the blood–brain barrier in ddY, FVB, and C57BL/6J mice. Fluids Barriers CNS. 2013;10(1):21.
84. Weksler B, Romero IA, Couraud PO. The hCMEC/D3 cell line as a model of the human blood brain barrier. Fluids Barriers CNS. 2013;10(1):16.
85. Boyer-Di Ponio J, et al. Instruction of circulating endothelial progenitors in vitro towards specialized blood–brain barrier and arterial phenotypes. PLoS ONE. 2014;9(1):e84179.
86. Cecchelli R, et al. A stable and reproducible human blood–brain barrier model derived from hematopoietic stem cells. PLoS ONE. 2014;9(6):e99733.
87. Bergmann S, et al. Blood–brain-barrier organoids for investigating the permeability of CNS therapeutics. Nat Protoc. 2018;13(12):2827–43.
88. Ballermann BJ, Ott MJ. Adhesion and differentiation of endothelial cells by exposure to chronic shear stress: a vascular graft model. Blood Purif. 1995;13(3–4):125–34.
89. Palmiotti CA, et al. In vitro cerebrovascular modeling in the 21st century: current and prospective technologies. Pharm Res. 2014;31(12):3229–50.
90. Cucullo L, et al. A new dynamic in vitro model for the multidimensional study of astrocyte–endothelial cell interactions at the blood–brain barrier. Brain Res. 2002;951(2):243–54.
91. Naik P, Cucullo L. In vitro blood–brain barrier models: current and perspective technologies. J Pharm Sci. 2012;101(4):1337–54.
92. Booth R, Kim H. Characterization of a microfluidic in vitro model of the blood–brain barrier (μBBB). Lab Chip. 2012;12(10):1784–92.
93. Miranda A, et al. Computational modeling in glioblastoma: from the prediction of blood–brain barrier permeability to the simulation of tumor behavior. Fut Med Chem. 2018;10(1):121–31.
94. Gao Z, et al. Predict drug permeability to blood–brain-barrier from clinical phenotypes: drug side effects and drug indications. Bioinformatics. 2016;33(6):901–8.
95. Toropov AA, et al. QSAR model for blood–brain barrier permeation. J Pharmacol Toxicol Methods. 2017;88:7–18.
96. Brown JA, et al. Recreating blood–brain barrier physiology and structure on chip: a novel neurovascular microfluidic bioreactor. Biomicrofluidics. 2015;9(5):054124.
97. Pacitti D, Privolizzi R, Bax BE. Organs to cells and cells to organoids: the evolution of in vitro central nervous system modelling. Front Cell Neurosci. 2019;13:129.
98. Cho CF, et al. Blood–brain-barrier spheroids as an in vitro screening platform for brain-penetrating agents. Nat Commun. 2017;8:15623.
99. Urich E, et al. Multicellular self-assembled spheroidal model of the blood brain barrier. Sci Rep. 2013;3:1500.
100. Cecchelli R, et al. Modelling of the blood–brain barrier in drug discovery and development. Nat Rev Drug Discov. 2007;6(8):650–61.
101. Pham MT, et al. Generation of human vascularized brain organoids. NeuroReport. 2018;29(7):588–93.
102. Akhtar AA, et al. Organoid and organ-on-a-chip systems: new paradigms for modeling neurological and gastrointestinal disease. Curr Stem Cell Rep. 2017;3(2):98–111.

103. Bardenbacher M, et al. Permeability analyses and three dimensional imaging of interferon gamma-induced barrier disintegration in intestinal organoids. Stem Cell Res. 2019;35:101383.
104. Nzou G, et al. Human cortex spheroid with a functional blood brain barrier for high-throughput neurotoxicity screening and disease modeling. Sci Rep. 2018;8(1):7413.
105. Jiao Y, et al. Acute effects of 1-methyl-4-phenyl-1,2,3,6-tetrahydropyridine (MPTP) or paraquat on core temperature in C57BL/6J mice. J Parkinsons Dis. 2015;5(2):389–401.
106. Pearson TS, et al. Phenotypic spectrum of glucose transporter type 1 deficiency syndrome (Glut1 DS). Curr Neurol Neurosci Rep. 2013;13(4):342.
107. Wang D, Pascual JM, De Vivo D. Glucose transporter type 1 deficiency syndrome, In: Adam MP, et al., editors. GeneReviews((R)). Seattle; 1993.
108. Wolburg H, et al. Brain endothelial cells and the glio-vascular complex. Cell Tissue Res 2009;335(1):75–96.
109. Fidler IJ. The role of the organ microenvironment in brain metastasis. Semin Cancer Biol 2011;21(2):107–12.
110. Elliott NT, Yuan F. A review of three-dimensional in vitro tissue models for drug discovery and transport studies. J Pharm Sci 2011; 100(1):59–74.
111. Villegas M, et al. Fabricating smooth PDMS microfluidic channels from low-resolution 3D printed molds using an omniphobic lubricantinfused coating. Anal Chim Acta. 2018;1000:248–55.
112. Hampson S, et al. 3D printed microfluidic device with integrated optical sensing for particle analysis. Sens Actuators B Chem. 2018;256:1030–7.
113. Gaal G, et al. Simplified fabrication of integrated microfluidic devices using fused deposition modeling 3D printing. Sens Actuators B Chem. 2017;242:35–40.
114. Lee J-Y, An J, Chua CK. Fundamentals and applications of 3D printing for novel materials. Appl Mater Today. 2017;7:120–33.
115. Wang X, et al. 3D printing of polymer matrix composites: a review and prospective. Compos B Eng. 2017;110:442–58.
116. Norman J, et al. A new chapter in pharmaceutical manufacturing: 3D-printed drug products. Adv Drug Deliv Rev. 2017;108:39–50.
117. Lewis PL, Green RM, Shah RN. 3D-printed gelatin scaffolds of differing pore geometry modulate hepatocyte function and gene expression. Acta Biomaterialia. 2018;69:63–70.
118. Hwang Y, Paydar OH, Candler RN. 3D printed molds for non-planar PDMS microfluidic channels. Sens Actuators A. 2015;226:137–42.
119. Tymrak B, Kreiger M, Pearce JM. Mechanical properties of components fabricated with open-source 3-D printers under realistic environmental conditions. Mater Des. 2014;58:242–6.
120. Tran P, et al. Bimaterial 3D printing and numerical analysis of bioinspired composite structures under in-plane and transverse loadings. Compos B Eng. 2017;108:210–23.
121. Melnikova R, Ehrmann A, Finsterbusch K. 3D printing of textile-based structures by fused deposition modelling (FDM) with different polymer materials. In: IOP conference series: materials science and engineering. IOP Publishing; 2014.
122. Kim K, et al. 3D optical printing of piezoelectric nanoparticle–polymer composite materials. ACS Nano. 2014;8(10):9799–806.
123. Tayebi L, et al. 3D-printed thick structured gelatin membrane for engineering of heterogeneous tissues. Mater Lett. 2018;217:39–43.
124. Sochol RD, et al. 3D printed microfluidics and microelectronics. Microelectron Eng. 2018;189:52–68.
125. Ho CMB, et al. 3D printed microfluidics for biological applications. Lab Chip. 2015;15(18):3627–37.
126. Li J, Rossignol F, Macdonald J. Inkjet printing for biosensor fabrication: combining chemistry and technology for advanced manufacturing. Lab Chip. 2015;15(12):2538–58.
127. Ge Q, et al. Active origami by 4D printing. Smart Mater Struct. 2014;23(9):094007.
128. Cooperstein I, Layani M, Magdassi S. 3D printing of porous structures by UV-curable O/W emulsion for fabrication of conductive objects. J Mater Chem C. 2015;3(9):2040–4.
129. Postiglione G, et al. Conductive 3D microstructures by direct 3D printing of polymer/carbon nanotube nanocomposites via liquid deposition modeling. Compos A Appl Sci Manuf. 2015;76:110–4.
130. Saari M, et al. Fiber encapsulation additive manufacturing: an enabling technology for 3D printing of electromechanical devices and robotic components. 3D Print Addit Manuf. 2015;2(1):32–9.

131. Ades EW, et al. HMEC-1: establishment of an immortalized human microvascular endothelial cell line. J Investig Dermatol. 1992;99(6):683–90.
132. Sano Y, et al. Establishment of a new conditionally immortalized human brain microvascular endothelial cell line retaining an in vivo blood– brain barrier function. J Cell Physiol. 2010;225(2):519–28.
133. Stins MF, Badger J, Sik Kim K. Bacterial invasion and transcytosis in transfected human brain microvascular endothelial cells. Microb Pathog. 2001;30(1):19–28.
134. Prudhomme JG, et al. Studies of Plasmodium falciparum cytoadherence using immortalized human brain capillary endothelial cells. Int J Parasitol. 1996;26(6):647–55.
135. Lian X, et al. Efficient differentiation of human pluripotent stem cells to endothelial progenitors via small-molecule activation of WNT signaling. Stem Cell Rep. 2014;3(5):804–16.
136. Patel R, Page S, Al-Ahmad AJ. Isogenic blood–brain barrier models based on patient-derived stem cells display inter-individual differences in cell maturation and functionality. J Neurochem. 2017;142(1):74–88.
137. Lippmann ES, et al. Modeling the blood–brain barrier using stem cell sources. Fluids Barriers CNS. 2013;10(1):2.
138. Roux GL, et al. Proof-of-concept study of drug brain permeability between in vivo human brain and an in vitro iPSCs-human blood–brain barrier model. Sci Rep. 2019;9(1):16310.
139. Neuhaus W. Human induced pluripotent stem cell based in vitro models of the blood–brain barrier: the future standard? Neural Regen Res. 2017;12(10):1607.
140. Barkho BZ, Zhao X. Adult neural stem cells: response to stroke injury and potential for therapeutic applications. Curr Stem cell Res Ther. 2011;6(4):327–38.
141. Bagchi S, et al. In-vitro blood–brain barrier models for drug screening and permeation studies: an overview. Drug Des Dev Ther. 2019;13:3591.
142. Yamanaka S, Blau HM. Nuclear reprogramming to a pluripotent state by three approaches. Nature. 2010;465(7299):704.
143. Brown TD, et al. A microfluidic model of human brain (muHuB) for assessment of blood brain barrier. Bioeng Transl Med. 2019;4(2):e10126.
144. Grifno GN, et al. Tissue-engineered blood–brain barrier models via directed differentiation of human induced pluripotent stem cells. Sci Rep. 2019;9(1):13957.
145. Jamieson JJ, et al. Role of iPSC-derived pericytes on barrier function of iPSC-derived brain microvascular endothelial cells in 2D and 3D. Fluids Barriers CNS. 2019;16(1):15.
146. Campisi M, et al. 3D self-organized microvascular model of the human blood–brain barrier with endothelial cells, pericytes and astrocytes. Biomaterials. 2018;180:117–29.
147. Wang JD, et al. Organization of endothelial cells, pericytes, and astrocytes into a 3D microfluidic in vitro model of the blood–brain barrier. Mol Pharm. 2016;13(3):895–906.
148. Partyka PP, et al. Mechanical stress regulates transport in a compliant 3D model of the blood–brain barrier. Biomaterials. 2017;115:30–9.
149. Herland A, et al. Distinct contributions of astrocytes and pericytes to neuroinflammation identified in a 3D human blood–brain barrier on a chip. PLoS ONE. 2016;11(3):e0150360.
150. Walter FR, Valkai S, Kincses A, Petneházi A, Czeller T, Veszelka S, Ormos P, Deli MA, Dér A. A versatile lab-on-a-chip tool for modeling biological barriers. Sens Actuators B Chem. 2016;222:10.
151. Kim JA, et al. Collagen-based brain microvasculature model in vitro using three-dimensional printed template. Biomicrofluidics. 2015;9(2):024115.
152. Deosarkar SP, et al. A novel dynamic neonatal blood–brain barrier on a chip. PLoS ONE. 2015;10(11):e0142725.
153. Sellgren KL, Hawkins BT, Grego S. An optically transparent membrane supports shear stress studies in a three-dimensional microfluidic neurovascular unit model. Biomicrofluidics. 2015;9(6):061102.
154. Prabhakarpandian B, et al. SyM-BBB: a microfluidic blood brain barrier model. Lab Chip. 2013;13(6):1093–101.
155. Achyuta AK, et al. A modular approach to create a neurovascular uniton-a-chip. Lab Chip. 2013;13(4):542–53.
156. Griep LM, et al. BBB on chip: microfluidic platform to mechanically and biochemically modulate blood–brain barrier function. Biomed Microdevices. 2013;15(1):145–50.

157. Cucullo L, et al. A dynamic in vitro BBB model for the study of immune cell trafficking into the central nervous system. J Cereb Blood Flow Metab. 2011;31(2):767–77.

# TABLES

| Date published | Microvessel/endothelial compartment size | Material and membrane | Biological coating | Endothelial cell type | Additional cells in co-culture (type) | Barrier permeability tracer | Permeability measurement (cm/s) | TEER (Ω $cm^2$) | Shear stress (dyne/$cm^2$) | Ref# |
|---|---|---|---|---|---|---|---|---|---|---|
| 2019 | Microfluidic device (200 μM width, 100 μM height) | PDMS | Human fibronectin (300 μg/ml) | Immortalized human cerebrovascular endothelial cells (hcmec\D3) | Astrocytes cultured in basolateral compartment | 10 kDa and 70 kDa FITC dextran | 10 kDa FITC dextran: $15 \times 10^{-6}$ cm/s<br>70 kDa FITC dextran: $3.7 \times 10^{-6}$ cm/s | NA | 2.73 | [143] |
| 2019 | 150 μM | PDMS | Collagen type IV and Fibronectin | BMECs derived from human iPSCs | N/A | Lucifer yellow, Alexa 647 conjugated 10 kDa dextran | Lucifer yellow: $5–6 \times 10^{-7}$<br>Alexa 647 conjugated 10 kDa dextran: below detection limit | 2000–4000 | 1 | [144] |
| 2019 | (Two channels) 2 cm long and 1 mm wide; top and bottom channels were 1 and 0.2 mm high | PDMS), 2-channel, separated from a parallel vascular microchannel by a porous (2 μm diameter), polyethylene terephthalate (PET) membrane | Collagen type IV and fibronectin | iPS-BMVECs | Primary human pericytes and astrocytes | Fluorescent labeled of dextran tracers (3, 10, or 70 kDa) | 8.9, 1.1, and $0.24 \times 10^{-8}$ cm/s for 3,10, and 70 kDa | 24,000[a] | 6 | [70] |
| 2019 | 150 μm | Collagen type 1 rat (hydrogel) | Collagen type IV and fibronectin | iPS-BMVECs | NA | Lucifer yellow, Rhodamine 123 (R123), and 10 kDa dextran | LY = $2.84 \pm 0.41 \times 10^{-7}$ cm/s<br>R123 = $1.32 \pm 0.16 \times 10^{-7}$ cm/s<br>The permeability of 10 kDa dextran in dhBMEC microvessels was below the detection limit | NA | 4 | [71] |
| 2019 | Cylindrical template rod (150 μm) | Collagen type 1 rat hydrogel | Collagen type IV and fibronectin | Human iPSC-ECs | Human iPSC-pericyte | Lucifer yellow, and 10 kDa dextran | LY = $4 \times 10^{-7}$ cm/s<br>The permeability of 10 kDa dextran was below the detection limit | NA | 4 | [145] |
| 2018 | Self orgnized less than 100 μm | Fibrin gel | Fibronectin | Human iPSC-ECs | Primary human pericytes and astrocytes | 40 and 10 kDa FTIC-dextrans | Of $8.9 \times 10^{-8}$ cm/s and $2.2 \times 10^{-7}$ cm/s for 40 kDa and 10 kDa FTICdextran, | NA | NA | [146] |

| Date published | Microvessel/endothelial compartment size | Material and membrane | Biological coating | Endothelial cell type | Additional cells in co-culture (type) | Barrier permeability tracer | Permeability measurement (cm/s) | TEER (Ω $cm^2$) | Shear stress (dyne/$cm^2$) | Ref# |
|---|---|---|---|---|---|---|---|---|---|---|
| 2017 | Microfluidic chip with fluidic channels (190 μM height and 920 μM width) | PDMS, hydrogel channel is 580 μM wide while the fluidic channel is 920 μM wide. Endothelial cells seeded in the fluid channels. Astrocyte and Neurons mixed in collagen-1 and perfused in the hydrogel channels | Poly-d-Lysine | HUVEC or hcmec\D3 | Primary cortical neuron from rat, primary astrocytes from rat | 10 kDa Oregon green 488 dextran, 70 kDa Texas red dextran | 10 kDa Oregon green 488 dextran in HUVEC: $7 \times 10^{-5}$ cm/s<br>70 kDa Texas Red Dextran in HUVEC: $5 \times 10^{-5}$ cm/s<br>10 kDa Oregon green 488 dextran in hcmec\D3: $1 \times 10^{-5}$ cm/s<br>70 kDa Texas Red Dextran in hcmec\D3: $0.25 \times 10^{-5}$ cm/s | NA | NA | [73] |
| 2017 | Microfluidic device (width 2 mm and height of 0.2, 0.6 and 1 mm) | PDMS with polyester membrane (0.4 μM) | Fibronectin solution | Immortalized mouse endothelial cells (Bend3) | Immortalized mouse pericytes adhering to polyester membrane on 2nd channel and mouse astrocyte type I clone on the bottom of 2nd channel | 10 kDa Oregon green 488 dextran 70 kDa Texas red dextran | Monoculture: HUVEC: $7 \times 10^{-5}$ cm/s (10 kDa), $5 \times 10^{-5}$ cm/s (70 kDa) hcmec\D3 | Single culture: ~ 134<br>Bi culture: ~ 260<br>Triculture: ~ 310 | NA | [147] |
| 2017 | (300 μm * 160μm) | Polycarbonate insert with 04 μm pore size | Collagen type IV and fibronectin | Human iPSC-ECs | Rat primary astrocytes | 4, 20 and 70 KDa FITC-dextrans | 4 kDa = $10^{-7}$ and 20 and 70 was close to$10^{-8}$ cm/s | 2000–4000 | 0.25 | [72] |
| 2017 | 180 μm cylindrical rod | Collagen type I hydrogel in PDMS | Collagen | (hCMEC/D3) | Human astrocytes | 4 kDa FITC-dextran | $0.8 \times 10^{-6}$ cm/s | 200-1000 | 0.5 | [148] |
| 2016 | PDMS with collagen hydrogel inside (1 mm * 1 mm) | Collagen type 1 rat | NA | Primary human endothelial cells | Primary human pericytes and astrocytes | 3 kDa fluorescent dextran | $2–4 \times 10^{-6}$ cm/s | NA | 1 | [149] |
| 2016 | Two rectangular PDMS channels with 3.7 cm × 0.2 cm × 0.2 cm size | Polycarbonate membrane with a thickness of 23 μm and a pore size 0.45 μm | Rat tail collagen | hCMEC/D3 | NA | Sodium fluorescein (376 Da), 4 kDa FITC-dextran, f Evans blue-labeled albumin (67 kDa) | Sodium fluorescein = $1.57 \times 10^{-6}$cm/s<br>4 kDa Dextran = $1.32 \times 10^{-6}$<br>Evans blue = $0.15 \times 10^{-6}$cm/s | 28 | 0.15 | [150] |

| Date published | Microvessel/endothelial compartment size | Material and membrane | Biological coating | Endothelial cell type | Additional cells in co-culture (type) | Barrier permeability tracer | Permeability measurement (cm/s) | TEER (Ω $cm^2$) | Shear stress (dyne/$cm^2$) | Ref# |
|---|---|---|---|---|---|---|---|---|---|---|
| 2016 | Two rectangular PDMS channels with 3.7 cm × 0.2 cm × 0.2 cm size | Polycarbonate membrane with a thickness of 23 μm and a pore size 0.45 μm | Rat tail collagen | Primary rat brain endothelial cells | Rat primary pericytes and astroglia | Sodium fluorescein (376 Da), 4 kDa FITC-dextran, f Evans blue-labeled albumin (67 kDa) | Sodium fluorescein = $1.15 \times 10^{-6}$cm/s 4 kDa Dextran = $0.20 \times 10^{-6}$ Evans blue = $0.04 \times 10^{-6}$cm/s | 114.2 | 0.15 | [150] |
| 2015 | Microfluidic chip with vascular channel having 100 μM height | PDMS, 0.2 μM Polycarbonate membrane | Laminin | Primary hBMVEC | Primary astrocytes, and pericytes plus neurons differentiated from hiPSCs | 10 kDa and 70 kDa FITC Dextran | Not measured. Only absolute fluorescence measured | Custom built impedance measurement (~ 12,000[a]) | NA | [96] |
| 2015 | 3D printed vessels having 235 and 260 μM diameters | 3D co-printing Vero White Plus-FullCure 835 resin as main framework and poly-vinyl alcohol (PVA) as a dissolvable support material | Fibronectin | Bend3 cells | N/A | 40 kDa FITC dextran | $2.27 \times 10^{-7}$ cm/s | NA | NA | [151] |
| 2015 | Rectangular PDMS channel (6.3 mm × 100 μm) | PDMS | Fibronectin | Neonatal rat brain capillary endothelial cells | Primary cultures of neonatal rat astrocytes | 10 and 70 kDa fluorescent dextran | $2.9 \pm 1.0 \times 10^{-6}$ | 150-180 | $3.8 \times 10^{-3}$ | [152] |
| 2015 | Rectangular PDMS channel (1 mm × 150 μm) | PDMS | Collagen IV–fibronectin | bEnd3 | Immortalized mouse astrocyte C8D1A | 70 KDa dextran | $5.9 \times 10^{-7}$ cm/s | NA | 5 | [153] |
| 2013 | Rectangular PDMS channel (200 μm × 100 μm) | PDMS | Fibronectin | Rat brain EC (RBE4 cells) | N/A | 3 and 5 KD FITC-dextran | Relative comparison only | NA | NA | [154] |
| 2013 | PDMS channel (100 μM × 500 μM) | PDMS | Fibronectin | Rat brain EC (RBE4 cells) | E18 rat cortical cells | 3 kDa Alexa fluor-dextran | Relative comparison only | NA | NA | [155] |
| 2012 | Rectangular PDMS channel with a length of 1 cm, a width of 500 μm and a depth of 100 μm | Polycarbonate membrane with a thickness of 10 μm and a pore size of 0.4 μm | Rat collagen type I | (hCMEC/D3) | N/A | N/A | N/A | 120 | 5.8 | [156] |

| Date published | Microvessel/endothelial compartment size | Material and membrane | Biological coating | Endothelial cell type | Additional cells in co-culture (type) | Barrier permeability tracer | Permeability measurement (cm/s) | TEER (Ω cm$^2$) | Shear stress (dyne/cm$^2$) | Ref# |
|---|---|---|---|---|---|---|---|---|---|---|
| 2011 | 11 hollow polypropylene fibers (600 ± 90 μM) inside a sealed chamber (the extraluminal space) accessible by ports | Polypropylene with transcapillary pores (2 to 4 μM) | Fibronectin | Normal adult human brain microvascular endothelial cells | Human adult astrocytes | Sucrose, phenytoin and diazepam | Sucrose: $3.16 \times 10^{-6}$, phenytoin: $6.75 \times 10^{-5}$, diazepam: $6.88 \times 10^{-3}$ cm/s | ~ 500 on the 21st day | 4 | [157] |
| 2002 | 11 hollow polypropylene fibers (600 ± 90 μM) inside a sealed chamber (the extraluminal space) accessible by ports | Polypropylene hollow fiber apparatus with 12 μM pores | Fibronectin | Bovine aortic endothelial cells (BAEC) | Rat glial cell tumor line | N/A | N/A | 500 | NA | [90] |

"N.A." shows that the specified aspect has not been measured or reported
[a] Indicates the TEER value reported were not normalized based on the surface area of the microfluidic chip

FIGURES

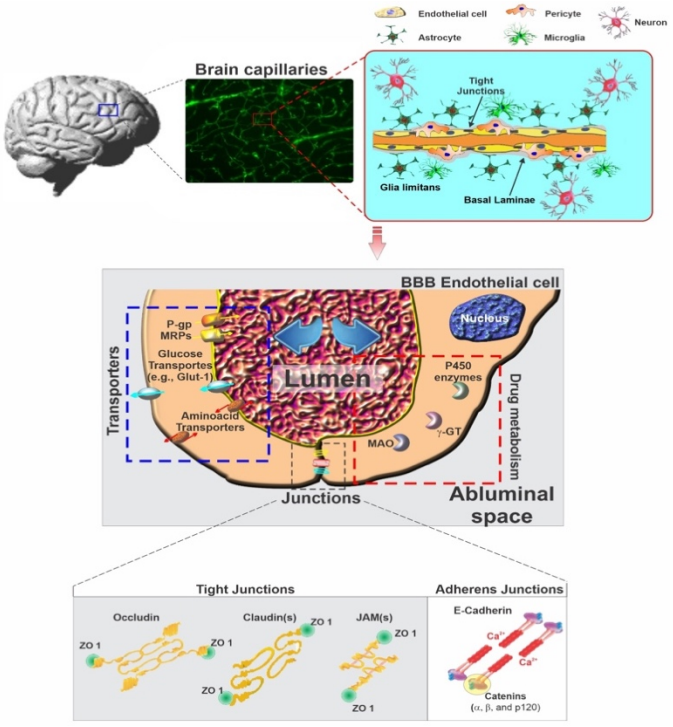


Fig. 1.1 Schematic view of a typical brain microcapillary. Note that the passage of substances across the BBB endothelium is controlled by a multimodal barrier system; (1) gating barrier (tight junctions) which prevents paracellular diffusion of polar molecules. Note that the adherens junction play the critical role of keeping the cell membrane of

adjacent endothelial cells close together, thus allowing for the formation of the tight junctional bindings; (2) transport barrier which includes number of active efflux systems (P-gp, MRPs, etc.) with affinity for lipophilic substances; (3) metabolic/enzymatic barrier (cytochrome P450 enzymes, MAO, etc.) which catalyze the oxidation/metabolism of organic substrates including xenobiotic substances such as drugs and other potentially toxic chemicals.

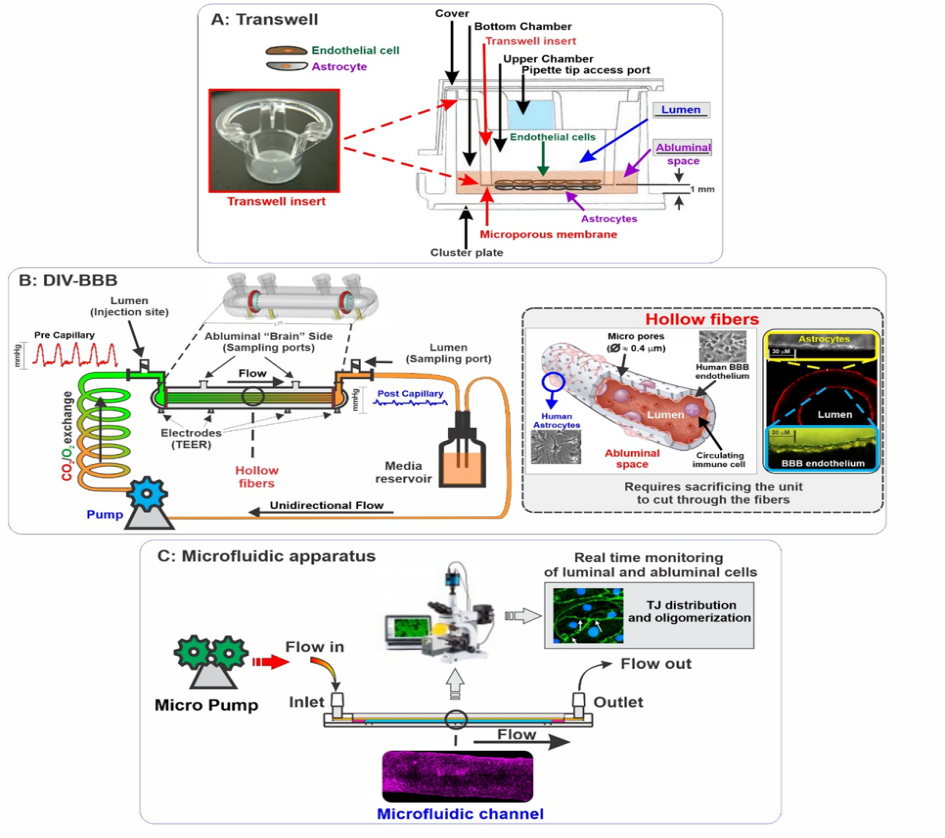


Fig. 1.2 Side by side schematic view of various in vitro BBB platforms. A) The Transwell apparatus which consists of a vertical side by side diffusion system across a semipermeable microporous membrane. The membrane allows for free passage of nutrients and diffusible factors between the luminal and abluminal compartments. Depending on the membrane's pore size, cell extravasation across the compartments can be enabled. B) Dynamic in vitro BBB model (DIV-BBB). This platform relies on the use of hollow fibers to simulate the architecture of a blood vessel. The hollow fiber can be pre-coated with specific coating factor to enable the adhesion of endothelial cells (generally on the luminal surface of the fiber) and astrocytes or other NVU cell types on the abluminal surface in juxtaposition to the endothelium. A pulsatile pump generates the medium flow across the system, mimicking the blood flow traveling inside the blood vessel. The bundle of hollow fibers is suspended inside a sealed chamber. The artificial

capillaries are in continuity with a medium source through a flow path consisting of gas-permeable silicone tubing. Ports positioned on either side of the module allow access to the luminal and abluminal compartments. The system allows generating rheological conditions like those observed in vivo. It also allows for the perfusion and circulation of immune cells as required. C) Schematic illustrations of a typical microfluidic platform. The system recapitulates the characteristic of a DIV-BBB but to a much smaller scale. Most of these platforms also enable visual assessment of the cell environment through visual microscopy (including fluorescent, and confocal) to assess cell morphology, distribution, cell contact, etc. Some of the limitations inherent to microfluidic systems include the very small sampling size (for qualitative quantitate assessments) and lack of availability to other researchers with very few exceptions.

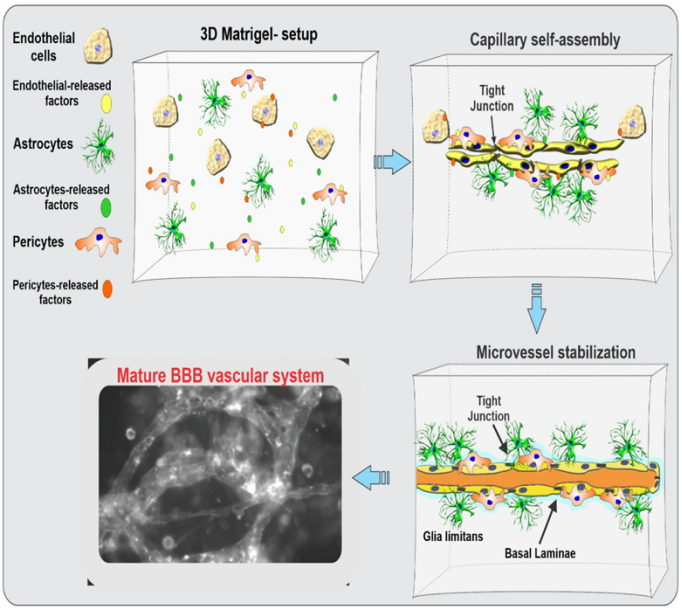


Fig. 1.3 Schematic representation of a 3D ECM-based in vitro BBB model. This platform enables culturing multiple cell types (related to a specific organ system) at once. The formation of natural gradients of biological factors (either introduced into the matrix and/or naturally produced by the cells in culture) promotes a host of physiological responses (including cell migration, interaction, and differentiation) culminating with the self-assembly of microvascular processes and the formation of a network of capillary-like structures in vitro.

# CHAPTER TWO

# HIV-1 GP120 AND TOBACCO SMOKE SYNERGISTICALLY DISRUPT THE INTEGRITY OF THE BLOOD-BRAIN BARRIER

In the United States, the Centers for Disease Control and Prevention (CDC) terms HIV and tobacco use among the ten most important public health challenges we face today. In the last decade, there has been a remarkable decrease in the number of deaths due to HIV/AIDS, especially after the widespread availability and use of combination antiretroviral therapy (cART). However, people living with HIV/AIDS have a heightened risk of chronic complications and comorbidities, including neurological disorders. Around 40–60 % of HIV-infected individuals progress to NeuroAIDS, a group of disorders caused primarily by HIV-mediated damage to the central and peripheral nervous systems, despite receiving cART. The detrimental effects of chronic smoking on the cerebrovascular system are also well studied and reported. Addictive behavior, such as smoking, is more common in HIV patients compared to the general population. In this context, given the existing immune suppression, smoking can pose a significant risk for the progression of the disease to NeuroAIDS by disrupting the integrity of the blood-brain barrier (BBB). Here we show that co-treatment with Tobacco Smoke Extract (TSE) and HIV-1 gp120 (HIV envelope glycoprotein) in primary cultures of human brain microvascular endothelial cells promoted heightened cellular stress responses compared to control and individual treatments. Our findings suggest that a potential synergistic effect between smoke exposure and gp120 can worsen the loss of BBB viability, possibly exacerbating NeuroAIDS progression.

## Introduction

The Human Immunodeficiency Virus (HIV) causes Acquired Immune Deficiency Syndrome (AIDS) in humans. AIDS is characterized by a critical depletion of the body's immune cells, considerably increasing susceptibility to infection and malignancy [1, 2]. Beyond systemic immune dysfunction, HIV can also invade the central nervous system (CNS), leading to persistent infection and inflammation [3, 4]. The advent of antiretroviral therapy has significantly reduced the global burden of HIV in recent decades. However, due to increased life expectancy, people living with HIV continue to face a heightened risk of chronic complications and comorbidities, including cardiovascular, renal, hepatic, and neurological disorders [5]. Chronic HIV-1 infection within the CNS can result in a spectrum of neurodegenerative conditions collectively termed NeuroAIDS [6]. HIV may enter the brain either through adsorptive endocytosis across endothelial cells [7] or by exploiting infected T-cells and macrophages that migrate to the brain [8]. Although neurons are not directly infected, neuronal injury occurs indirectly through viral infection of other CNS cell types, particularly microglia and, to a lesser extent, astrocytes [9-11]. The immune-privileged nature of the brain is enforced by the BBB, which plays a critical role in the normal physiology of the CNS by regulating what reaches the brain from the periphery [12]. Compactly arranged brain microvascular endothelial cells (BMECs) are the main constituents of the BBB.

Astrocytes, pericytes, and microglia also support the BBB structurally & biochemically. Tight junctions (TJ) between adjacent BMECs play a major role in forming a gating barrier, one of the most crucial properties of the BBB [13]. Once inside, HIV and its toxic components can induce persistent oxidative stress and inflammation, cause cerebrovascular damage, and eventually lead to neuronal death [14]. The virus consists of a capsid, envelope, single-stranded RNA genome, and various enzymes [15] (Fig.1). The HIV genome codes for various proteins that interfere with CNS homeostasis; the two more important viral proteins that were shown to be cytotoxic are gp120, the virus's envelope protein, and the trans-activator transcription (Tat) protein present in the capsid [16].

The envelope glycoprotein gp120 is exposed on the surface of the HIV envelope and is essential for virus entry into cells by its attachment to the CD4 (cluster of differentiation 4) receptor and co-receptors CCR5 (C-C chemokine receptor type 5) and CXCR4 (C-X-C chemokine receptor type 4) [17]. It comprises two domains, the exterior envelope spike glycoprotein gp120 and the transmembrane glycoprotein gp41 [18]. In the serum of HIV-infected individuals, it can be found as soluble gp120, cell-associated gp120, and virion-associated gp120. HIV gp120 levels in serum and CSF – 500 ng/ml and 5 µg/ml. Each HIV virion can have up to 300 gp120 molecules on its surface [19]. HIV gp120 is a potent neurotoxin and is also known to cause oxidative stress. Looking into the link between HIV/AIDS & high-risk behaviors, it is observed that drug abuse, alcohol consumption, and smoking are highly implicated in reduced response & adherence to the cART regimen and their roles in disease progression [20]. A study published in 2013 reported that around 45 % of HIV-infected participants who smoked showed signs of cognitive impairment [21]. The prevalence of cigarette smoking among adults in the United States is 14 %, whereas it is between 50 % and 70 % in HIV-positive adults [22]. Furthermore, continued smoking in HIV-infected people causes them to lose more life years than the disease itself [23]. Previously, in our lab, we have demonstrated that tobacco smoke is a potent oxidative and inflammatory stress-inducing agent that can facilitate the loss of BBB function and mitochondrial redox balance leading to a host of comorbidities [24, 25]. Similarly, other groups have carried out studies that show HIV-1 envelope glycoprotein (gp120) being responsible for causing oxidative stress with direct implications for BBB impairment [26, 27]. However, whether synergism exists between the two in compromising the BBB is unknown. This study aims to investigate whether tobacco smoke and HIV-1 envelope protein gp120, collectively, may have a contributory effect on aggravating BBB impairment.

## Materials and Methods

### TSE preparation

For the preparation of tobacco smoke extract, we used the standardized ISO/FTC smoking protocol of 35 ml draw, 2-second puff duration, one puff per 60 s using 3R4F (University of Kentucky) standard reference cigarettes in the Single Cigarette Smoking Machine (SCSM, CH Technologies Inc., Westwood, NJ, USA). Smoke from one

cigarette comprising eight puffs was collected in PBS to obtain stock TSE solution. The stock was diluted to the desired concentration as per the study published by our lab previously [28].

**HIV-1 gp120**

HIV-1 gp120, recombinant (Sigma Aldrich # SAE0071), was obtained, and a stock concentration of 100 µg/ml was prepared by reconstituting in ultrapure water. It is estimated that gp120 levels may range from 500 ng/ml to 5 µg/ml in the serum of HIV-infected patients [19]. We performed an MTT assay with varying gp120 concentrations (0, 0.1, 0.2, 0.4, 0.8, 1.6, 3.2 and 5 µg/ml) over a period of 24 h and used 1.6 µg/ml concentration for our treatments.

**Cell culture**

Primary Human Brain Microvascular Endothelial Cells (Cell Systems # ACBRI 376) were expanded in 75 cm2 flasks precoated with Cell Systems Attachment Factor™ (4Z0-210) in the recommended growth medium (Complete Classic Medium - 4Z0-500). Cells were incubated at 37°C with 5% CO2 and 95% air. The primary cultures used in the current study were between passages 3-8. Before treatment, the growth medium was replaced by a medium without serum (4Z3-500) for 24 hours.

**Cell viability**

HBMECs were cultured in a 96 well plate for 24 h and were later assessed for cell viability as per the protocol for Cell Growth Determination Kit MTT based (Sigma Aldrich # CGD-1). After completion of the assay, absorbance was measured at 570 nm in a plate reader.

**Treatment**

HBMECs in cell culture flasks, plates, and transwells were then exposed to 5 % TSE (model of mainstream smoke exposure previously described by our group [24] for 24 h with and without 1.6 µg/ml gp120. HIV-1 gp120 treatment doses for in vitro studies were selected based on an MTT cell viability study.

**Intracellular ROS Detection Assay**

HBMECs were seeded on 96 well plates and treated for 24 h. Intracellular ROS was assessed by employing ROS Detection Cell-Based Assay Kit - DCFDA (Cayman Chemical # 601520) as per the protocol mentioned therein. At the end of the assay, fluorescence was measured in a fluorescent imaging plate reader at excitation (480-500 nm) and emission (510-550 nm) wavelengths.

**Western blotting**

HBMECs were plated on T75 flasks and treated for 24 h. At the end of the treatment period, cells were washed twice with ice-cold phosphate-buffered saline (PBS) and harvested into lysis buffer (Thermo Fisher # 89900) containing protease inhibitors (Thermo Fisher # 78442). The protein content in each sample was determined using BCA Assay (Thermo Fisher # 23225). Equal amounts of protein (30 µg) were loaded in each well and ran on SDS-PAGE. The separated proteins were then transferred onto nitrocellulose membranes using Power Blotter XL (Thermo Fisher # PB0013). 5% nonfat milk in Tris-buffered saline containing 0.1% Tween-20 was used to block the membranes for 45 min at room temperature. The membranes were then incubated with anti-NRF2 antibody (1:500) (Santa Cruz # sc-365949), anti-NFκB (1:1000) (Cell Signaling # 8242S), anti-ZO-1(1:1000) (Invitrogen # 61-7300), anti-Occludin (Invitrogen # 33-1500) (1:1000) anti-β-Actin antibody (1:1000), anti-GAPDH antibody (1:5000) (Cell Signaling # sc-47724) at 4°C overnight, followed by washing and incubation in HRP-conjugated secondary antibodies for one hour (1:10,000). Immuno-reactive bands were visualized using a chemiluminescence system according to the manufacturer's instructions. Band densities were analyzed using ImageJ and expressed as fold change over controls after normalizing them against β-actin and GAPDH.

**Immunostaining**

HBMECs were plated on 6 well plates for immunocytochemistry and treated for 24 h. Cells were then washed twice with ice-cold PBS before being fixed in methanol (HPLC grade) for 5 min. Next, the cells were permeabilized with 0.2% Triton-X in PBS for 5 min. After another round of washing with PBS, cells were blocked with 5% bovine serum albumin (BSA) in PBS for one hour at room temperature (RT). Samples were then incubated overnight at 4°C with anti-NRF2 antibody (Santa Cruz # sc-365949), anti-ZO-1 (Invitrogen # 61-7300), anti-Occludin (Invitrogen # 33-1500) antibodies (1:100) in 10% goat serum in PBS. The following day, cells were washed, stained with Alexa Fluor 488 or 555 conjugated goat anti-rabbit or anti-mouse antibodies, and mounted with DAPI in prolonged gold anti-fade mounting media (Thermo Fisher # P36935). Cells were observed at 20x using an inverted fluorescence microscope. ImageJ software was used to quantify mean fluorescence intensity.

**Real-time quantitative polymerase chain reaction (qPCR)**

HBMECs were plated on T75 flasks and treated for 24 h. In brief, total RNA was extracted from treated cells using the RNeasy Mini Kit (Qiagen # 74104). The RNA concentration and purity were confirmed using the Nanodrop ND-1000 system. High-Capacity RNA-to-cDNA Kit (Thermo Fisher # 4387406) was used to prepare cDNA. The reaction mixture of 12 µl consisted 1µl of cDNA, 0.5 µl of each primer pair, NRF2 forward primer, (5' - GTT GCC CAC ATT CCC AAA TC -3') reverse primer, (5' - CGT AGC CGA AGA AAC CTC AT - 3') and NF□B-p65 forward primer, (5' - TGA GCC CAC AAA GCC TTA TC -3') reverse primer, (5' - ACA ATG CCA GTG CCA TAC A - 3'). The reaction was carried out using a Bio-Rad CFX96 Touch Real-Time PCR detection system. The relative gene expression was calculated by the ΔΔCt method by

normalizing gene of interest expression (Ct value) against house-keeping genes (β-actin or GAPDH).

**Mitochondrial Stress Assay**

HBMECs were seeded as per optimal guidelines suggested in the Agilent Seahorse XF Cell Mito Stress Test Kit User Guide (Agilent # 103015-100). Cells were allowed to attain the desired confluency and then treated for 24h. After treatment, the cell culture medium was replaced by an assay medium (Agilent # 103575-100) supplemented with 10 mM glucose, 10 mM pyruvic acid, and 1 mM L-glutamine. Subsequently, using the Seahorse Bioscience XFe 24 flux analyzer, we measured the basal oxygen consumption rate (OCR) without the addition of stressors.

**Mitochondrial membrane potential**

Mitochondrial membrane potential was evaluated using JC-1 Mitochondrial Membrane Potential Assay Kit (Cayman # 10009172). HBMECs were plated in a 96-well plate, ensuring 5 x 104 cells/well. 24 h following treatment, cells were stained with JC-1 reagent and incubated at 37 °C for 30 minutes. Subsequently, assay buffer was added to each well, and fluorescence intensity was determined using a plate reader (excitation – 485 nm and emission – 535 nm).

**BBB integrity**

HBMECs were seeded on transwells (Corning # 3460) and coated as described before. Following treatments for 24 h, BBB integrity was assessed by measuring TEER and paracellular permeability to sodium fluorescein. TEER values were obtained using EVOM 2 (World Precision Instruments). Paracellular permeability was assessed by adding sodium fluorescein (10 μm) to the apical chamber and sampling 100 μl from the basolateral chamber at 15 min intervals for 60 min while replenishing media therein. Permeability was calculated by using 1/(Pe x S) = 1/(Pt x S) - 1/(Pf x S) where, Pt = clearance slope of sample, Ps = clearance slope of blank and S = surface area of insert (cm2).

**Results**

**TSE and HIV-1 gp120 impact cell viability**

Endothelial cell viability was evaluated using an MTT assay. We observed a marked reduction in cell viability in the TSE-gp120 co-exposure group compared to control and individual treatments (Fig. 2.1A).

**TSE and HIV-1 gp120 increase the intracellular levels of reactive oxygen species (ROS)**

To examine the role of oxidative stress caused by combination treatment of TSE and gp120, intracellular ROS was assessed. Our results show that the combination treatment distinctly increased ROS (Fig. 2.1B) when compared to individual treatments and control.

**TSE and HIV-1 gp120 down-regulates NRF2 expression**

TSE and gp120 are known to cause oxidative stress individually. In response to such stimuli, the cellular antioxidant defense is activated. Nuclear factor-E2 related Factor-2 (NRF2) is a transcription factor that is responsible for cellular redox homeostasis and transcription of various antioxidant genes. The effects of our treatments on NRF2 mRNA expression levels were assessed by qPCR. We observed a significant decrease in NRF2 transcription across all treatments compared to controls (Fig. 2.2B). On the other hand, exposure to TSE upregulated NRF2 protein expression levels, whereas the standalone exposure to gp120 led to a modest decrease. However, combination treatment of TSE and gp120 reduced NRF2 protein levels, as shown by western blotting (Fig. 2.2A).

**TSE and HIV-1 gp120 increase NF-kB expression**

Another transcription factor implicated in oxidative stress events is the nuclear factor kappa-light-chain-enhancer of activated B cells (NFkB). This factor is also critical for regulating the immune response of a cell [29]. The effects of our treatments on NF-kB-p56 subunit mRNA expression levels were assessed by qPCR. As shown in Fig. 2.3A, mRNA expression of NF-kB-p56 was greatly increased in response to co-treatment with TSE and gp120 but remained relatively unchanged with individual treatments. Correspondingly, our western blot data showed elevated NF-κB protein levels in the TSE-gp120 co-treated group (Fig. 2.3B).

**TSE and HIV-1 gp120 disrupt mitochondrial function**

Oxidative stress can adversely impact mitochondrial equilibrium, which may give rise to pro-inflammatory signaling within the cell. Basal oxygen consumption rate (OCR), an indicator of mitochondrial respiration, was assessed using a seahorse flux analyzer. Our results showed that the TSE-gp120 co-treated group had a much-diminished basal oxygen consumption rate than individual treatments and controls (Fig. 2.4A), thereby indicating the disruption of mitochondrial function. A similar trend was observed when we tested mitochondrial membrane potential using JC-1 dye that can selectively enter mitochondria and form aggregates (red = healthy) or remain monomeric (green = unhealthy) based on the mitochondrial membrane potential. The TSE-gp120 co-treatment group exhibited a significantly reduced red/green ratio, meaning more cells with damaged mitochondria than others (Fig. 2.4B).

**TSE and HIV-1 gp120 disrupt the tight junction proteins and impair BBB integrity**

Zonula occludens 1 (ZO1) is a scaffolding protein that links TJ transmembrane proteins such as claudins and occludin to the actin cytoskeleton. Occludin plays a role in the

formation and regulation of the TJs. Both are essential to the maintenance of barrier integrity (Daneman and Prat, 2015; Jiao et al., 2011). Our results showed that exposure to TSE-gp120 negatively impacted the barrier and decreased the expression of ZO1 and Occludin, as shown by western blot and immunofluorescence analyses (Fig. 2.5 A–D). As expected, the downregulation of TJs expression negatively impacted the integrity of the endothelial barrier. As shown in Fig. 5E we observed a significant reduction in TEER values in the TSE-gp120 treated compared to the control group and individual treatments and a corresponding significant increase in fluorescein permeability (Fig. 2.5F).

**Discussion**

Oxidative stress, defined as the loss of physiological redox equilibrium, can have several exogenous and endogenous causative factors [30]. Reactive Oxygen Species or pro-oxidants are normally involved in the maintenance and regulation of cells; however, excess ROS levels can damage DNA, proteins, and lipids leading to a loss of cellular redox homeostasis [31]. Tobacco smoke contains more than 7000 toxic chemicals [32]. The oxidative potential of tobacco smoke is well studied. Our group has previously shown the harmful effects of oxidative damage caused by tobacco smoke on the cerebrovascular system with severe implications for stroke, diabetes, and post-traumatic brain injury [24, 33, 34]. HIV/AIDS is a disease that is characterized by severe loss of the body's inherent immunity leading to increased susceptibility to opportunistic infections. Evidence suggests that HIV-infected individuals are exposed to chronic oxidative stress [35]. Although several components of the virus are implicated in oxidative stress, HIV envelope glycoprotein gp120 is known to cause oxidative stress and is involved in disrupting the BBB [27].

In the present study, we treated HBMECs with TSE and gp120 to study the combined effects on BBB. Our results also show a significant increase in the ROS levels in response to co-treatment. NRF2 is an important transcription factor that regulates the cellular antioxidant stress response to oxidative stress [36]. As seen in our results decrease in NRF2 levels indicates that the expression of many antioxidants and neuroprotective genes may be severely affected in the context of smoking and HIV infection, thereby giving rise to subsequent pathophysiological consequences.

Both NRF2 and NF-kB are interlinked in many ways in neurodegenerative disorders. NF-kB is a nuclear transcription factor in numerous cell types and regulates the expression of many genes mediating an inflammatory response [36]. Our results show elevated NF-kB mRNA and protein levels in response to co-treatment. Activation of NF-kB causes transcription of related inflammatory factors, leading to vascular endothelial cell injury [37].

Next, we wanted to evaluate the effect of our treatments on mitochondrial function. Mitochondria play a key role in generating energy for cells to conduct various activities. Inadequate NRF2 function and the pro-inflammatory role of NF-kB are both implicated in promoting mitochondrial dysfunction [38, 39]. Our results show that the diminished

basal oxygen consumption rate and mitochondrial membrane potential indicate that mitochondrial functioning is severely compromised in the TSE-gp120 treated group. Thus, as seen above, impairment of mitochondrial function could have harmful consequences for the cells involved in maintaining the integrity of BBB and opening a pathway for the onset of neurological diseases. As demonstrated by our results, TSE-gp120 induced disruption in tight junction proteins, ZO-1, and occludin. The same was accompanied by a loss of BBB integrity, as demonstrated by the decrease in TEER values of the endothelial monolayers and the corresponding increase in paracellular permeability. Overall, a significant reduction in HBMEC cell viability was observed in the TSE-gp120 treated group suggesting an amplification of harmful effects when tobacco smoke and HIV gp120 act on the BBB, causing loss of characteristics and function.

## Conclusion

Our results suggest that oxidative stress, inflammation, and mitochondrial dysfunction seem to be the major underlying mechanisms through which tobacco smoke and HIV-1 envelope protein gp120 may synergistically impact the integrity and viability of the BBB. The resulting effect could potentially increase the burden of NeuroAIDS related morbidity and mortality in HIV infected individuals who smoke (Bhalerao and Cucullo, 2020). In the context of HIV/AIDS patients leading otherwise normal lives due to combination antiretroviral therapy (cART), this study could raise awareness of the negative impact of smoking on the onset and/or progression of HIV/AIDS-associated neurological disorders.

REFERENCES


1. Abbott, N.J., et al., 2010. Structure and function of the blood–brain barrier. Neurobiol. Dis. 37 (1), 13–25.
2. Asare, Y., et al., 2013. Endothelial CSN5 impairs NF-kappaB activation and monocyte adhesion to endothelial cells and is highly expressed in human atherosclerotic lesions. Thromb. Haemost. 110 (1), 141–152.
3. Banks, W.A., Akerstrom, V., Kastin, A.J., 1998. Adsorptive endocytosis mediates the passage of HIV-1 across the blood-brain barrier: evidence for a post-internalization coreceptor. J. Cell Sci. 111 (4), 533–540.
4. Bhalerao, A., Cucullo, L., 2019. Impact of tobacco smoke in HIV progression: a major risk factor for the development of NeuroAIDS and associated CNS disorders. J. Public Health 1–12.
5. Bhalerao, A., Cucullo, L., 2020. Impact of tobacco smoke in HIV progression: a major risk factor for the development of NeuroAIDS and associated of CNS disorders. Z. Gesund Wiss. 28 (3), 259–270.
6. Birben, E., et al., 2012. Oxidative stress and antioxidant defense. World Allergy Organ. J. 5 (1), 9–19.
7. Blood, G.A.C., 2016. Human immunodeficiency virus (HIV). Transfus. Med. Hemother. 43 (3), 203.
8. Boiss´e, L., Gill, M.J., Power, C., 2008. HIV infection of the central nervous system: clinical features and neuropathogenesis. Neurol. Clin. 26 (3), 799–819.
9. Burkhalter, J.E., et al., 2018. Participant characteristics and clinical trial decisionmaking factors in AIDS malignancy consortium treatment trials for HIV-infected persons with cancer (AMC# S006). HIV Clin. Trials 19 (6), 235–241.
10. Cross, S., et al., 2013. Identifying risk factors for HIV-associated neurocognitive disorders using the international HIV dementia scale. J. Neuroimmune Pharm. 8 (5), 1114–1122.

11. Cummins, N.W., Rizza, S.A., Badley, A.D., 2010. How much gp120 is there? J. Infect. Dis. 201 (8) (1273-1273).
12. Daneman, R., Prat, A., 2015. The blood–brain barrier. Cold Spring Harb. Perspect. Biol. 7 (1), a020412.
13. Deeks, S.G., Lewin, S.R., Havlir, D.V., 2013. The end of AIDS: HIV infection as a chronic disease. Lancet 382 (9903), 1525–1533.
14. Gilgun-Sherki, Y., Melamed, E., Offen, D., 2001. Oxidative stress induced neurodegenerative diseases: the need for antioxidants that penetrate the blood brain barrier. Neuropharmacology 40 (8), 959–975.
15. Gorry, P.R., et al., 2003. Astrocyte infection by HIV-1: mechanisms of restricted virus replication, and role in the pathogenesis of HIV-1-associated dementia. Curr. HIV Res. 1 (4), 463–473.
16. Helleberg, M., et al., 2015. Smoking and life expectancy among HIV-infected individuals on antiretroviral therapy in Europe and North America. AIDS 29 (2), 221.
17. Holmstrom, K.M., Kostov, R.V., Dinkova-Kostova, A.T., 2016. The multifaceted role of Nrf2 in mitochondrial function. Curr. Opin. Toxicol. 1, 80–91.
18. Jiao, H., et al., 2011. Specific role of tight junction proteins claudin-5, occludin, and ZO1 of the blood–brain barrier in a focal cerebral ischemic insult. J. Mol. Neurosci. 44 (2), 130–139.
19. Kaisar, M.A., et al., 2017. Offsetting the impact of smoking and e-cigarette vaping on the cerebrovascular system and stroke injury: is Metformin a viable countermeasure? Redox Biol. 13, 353–362.
20. Kanmogne, G.D., et al., 2007. HIV-1 gp120 compromises blood–brain barrier integrity and enhance monocyte migration across blood–brain barrier: implication for viral neuropathogenesis. J. Cereb. Blood Flow Metab. 27 (1), 123–134.
21. Letendre, S., 2011. Central nervous system complications in HIV disease: HIV-associated neurocognitive disorder. Top. Antivir. Med. 19 (4), 137.
22. Liu, T., et al., 2017. NF-κB signaling in inflammation. Signal Transduct. Target. Ther. 2 (1), 1–9.
23. Minagar, A., et al., 2008. NeuroAIDS. Mol. Diagn. Ther. 12 (1), 25–43.
24. Mollace, V., et al., 2001. Oxidative stress and neuroAIDS: triggers, modulators and novel antioxidants. Trends Neurosci. 24 (7), 411–416.
25. Naik, P., et al., 2014. Oxidative and pro-inflammatory impact of regular and denicotinized cigarettes on blood brain barrier endothelial cells: is smoking reduced or nicotine-free products really safe? BMC Neurosci. 15 (1), 51.
26. Naik, P., et al., 2015. Effect of full flavor and denicotinized cigarettes exposure on the brain microvascular endothelium: a microarray-based gene expression study using a human immortalized BBB endothelial cell line. BMC Neurosci. 16 (1), 38.
27. Nath, A., et al., 2000. Synergistic neurotoxicity by human immunodeficiency virus proteins Tat and gp120: protection by memantine. Ann. Neurol.: Off. J. Am. Neurol. Assoc. Child Neurol. Soc. 47 (2), 186–194.
28. Nisr, R.B., et al., 2019. Proinflammatory NFkB signalling promotes mitochondrial dysfunction in skeletal muscle in response to cellular fuel overloading. Cell. Mol. Life Sci. 76 (24), 4887–4904.
29. Pace, G.W., Leaf, C.D., 1995. The role of oxidative stress in HIV disease. Free Radic. Biol. Med. 19 (4), 523–528.
30. Prasad, S., et al., 2015. Impact of cigarette smoke extract and hyperglycemic conditions on blood–brain barrier endothelial cells. Fluids Barriers CNS 12 (1), 18.
31. Prasad, S., et al., 2017. Role of Nrf2 and protective effects of Metformin against tobacco smoke-induced cerebrovascular toxicity. Redox Biol. 12, 58–69.
32. Price, T.O., et al., 2005. HIV-1 viral proteins gp120 and Tat induce oxidative stress in brain endothelial cells. Brain Res. 1045 (1–2), 57–63.
33. Reynolds, N.R., 2009. Cigarette smoking and HIV: more evidence for action. AIDS Educ. Prev. 21 (3_suppl.), S106–S121.
34. Rock, R.B., et al., 2004. Role of microglia in central nervous system infections. Clin. Microbiol. Rev. 17 (4), 942–964.
35. Singh, A., Bairy, I., Shivananda, P., 2003. Spectrum of opportunistic infections in AIDS cases. Indian J. Med. Sci. 57 (1), 16–21.

36. Sivandzade, F., et al., 2019. NRF2 and NF-κB interplay in cerebrovascular and neurodegenerative disorders: molecular mechanisms and possible therapeutic approaches. Redox Biol. 21, 101059.
37. Sivandzade, F., et al., 2020. The cerebrovascular and neurological impact of chronic smoking on post-traumatic brain injury outcome and recovery: an in vivo study. J. Neuroinflamm. 17 (1), 133.
38. Sivandzade, F., Alqahtani, F., Cucullo, L., 2021. Impact of chronic smoking on traumatic brain microvascular injury: an in vitro study. J. Cell Mol. Med 25 (15), 7122–7134.
39. Wilen, C.B., Tilton, J.C., Doms, R.W., 2012. HIV: cell binding and entry. Cold Spring Harb. Perspect. Med. 2 (8), a006866.
40. Winstanley, E.L., Gust, S.W., Strathdee, S.A., 2006. Drug abuse and HIV/AIDS: international research lessons and imperatives. Drug Alcohol Depend. 82, S1–S5.
41. Wyatt, R., et al., 1998. The antigenic structure of the HIV gp120 envelope glycoprotein. Nature 393 (6686), 705–711.
42. Yadav, A., Collman, R.G., 2009. CNS inflammation and macrophage/microglial biology associated with HIV-1 infection. J. Neuroimmune Pharm. 4 (4), 430–447.
43. Zayyad, Z., Spudich, S., 2015. Neuropathogenesis of HIV: from initial neuroinvasion to HIV-associated neurocognitive disorder (HAND). Curr. HIV/Aids Rep. 12 (1), 16–24.

FIGURES

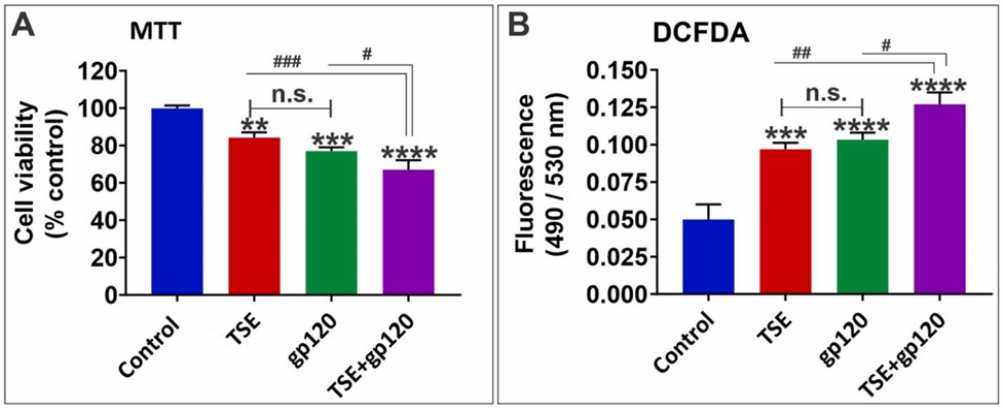


Fig. 2.1. Effects of TS and gp120 exposure on cell viability and oxidative stress. A: MTT cytotoxicity assay for cell viability following TS - gp120 treatments for 24 h. B: DCFDA assay as an indicator for reactive oxygen species (ROS) in cells. n = 3 biological replicates/group. *$p < 0.05$, ** $p < 0.01$, **$p < 0.001$, ****$p < 0.0001$ vs. control; #$p < 0.05$, ##$p < 0.01$, ###$p < 0.001$ vs. TS + gp120 co-treatment. n.s. = non statistical significance.

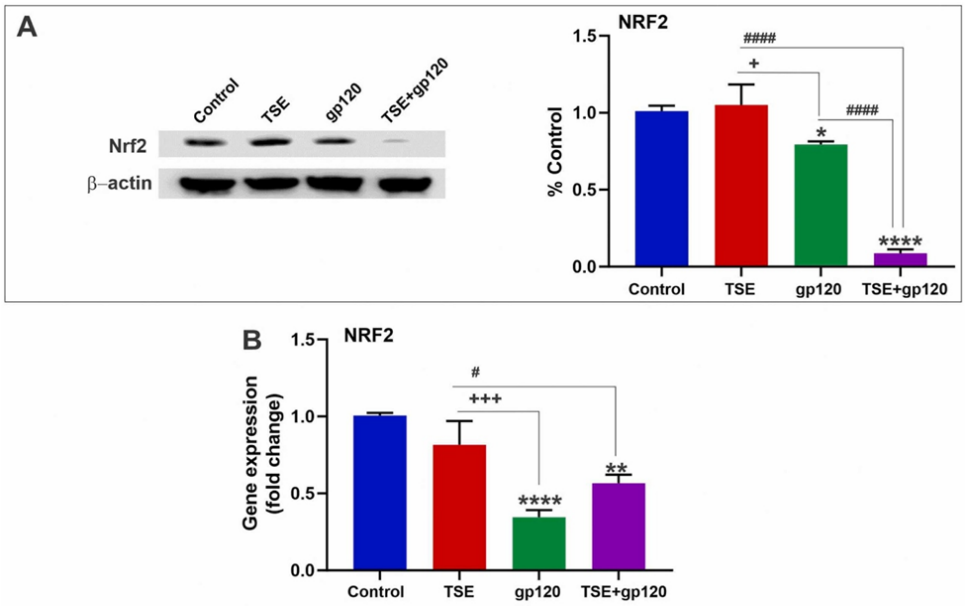


Fig. 2.2. Effects of TSE-gp120 exposure on NRF2 levels. A. Western Blot analysis of NRF2 protein. B. qPCR results show NRF2 mRNA levels. n = 3 biological replicates/group. *p < 0.05, ** p < 0.01, ****p < 0.0001 vs. control; +p < 0.05, +++p < 0.001 vs. gp120; #p < 0.05, ####p < 0.0001 vs. TS + gp120 co-treatment.

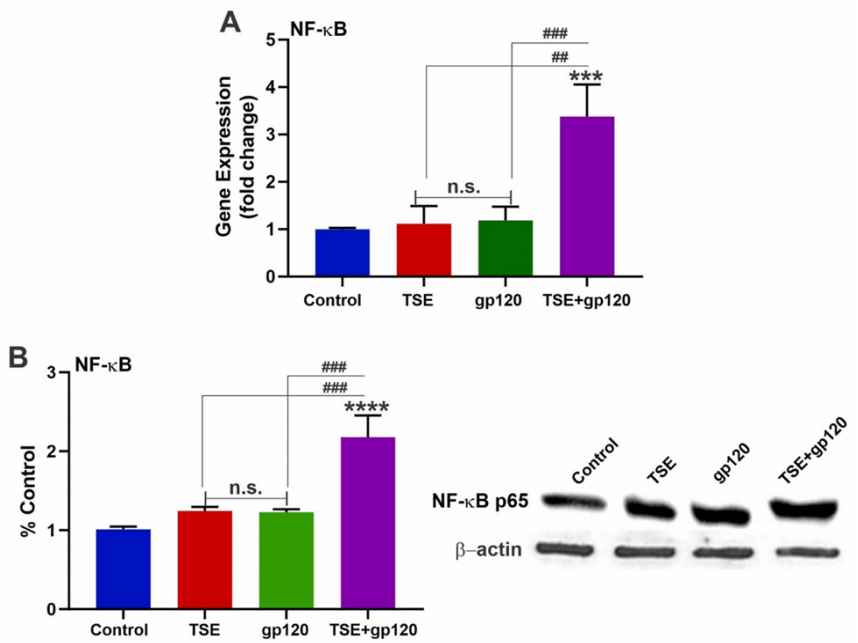


Fig. 2.3. A: NF-κB transcription assessed by qPCR showed substantial increase in NF-κB mRNA levels. B: Western Blot analysis showed elevated levels of NF-κB protein in the TSE-gp120 treated group. n = 3 biological replicates/group. ***p < 0.001, ****p < 0.0001 vs. control); ##p < 0.01, ###p < 0.001 vs. TS + gp120 co-treatment. n.s. = non statistical significance.

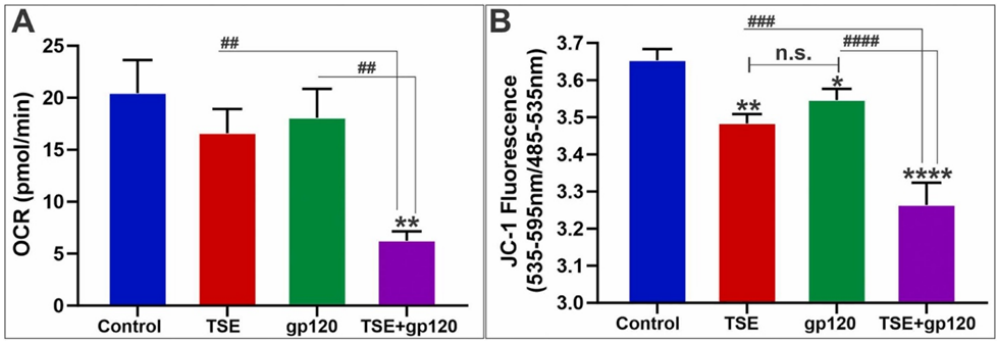


Fig. 2.4. A: Co-treatment of TSE-gp120 diminished basal oxygen consumption rate (OCR) in co-treated group when compared with individual treatments and control. B: Reduced mitochondrial membrane potential in TSE-gp120 combination treatment. n = 3 biological replicates/group. *p < 0.05, **p < 0.01, ****p < 0.0001 vs. control; ##p < 0.01, ###p < 0.001, ####p < 0.0001 vs. TS + gp120 co-treatment. n.s. = non statistical significance.

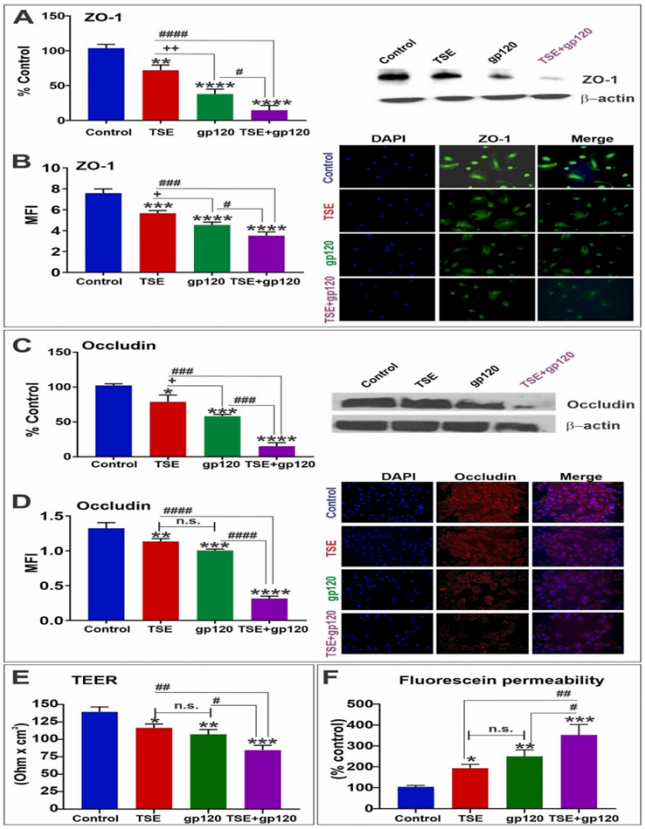


Fig. 2.5. Effects of TSE-Gp120 exposure on tight junction proteins and BBB integrity. Western blotting analysis showing the downregulation of ZO-1 (A) along with the corresponding Immunofluorescence images showing protein expression and distribution (B). Western blotting analysis showing the downregulation of Occludin (C) along with the corresponding Immunofluorescence images showing protein expression and distribution (D). TEER (E) and fluorescein permeability (F) demonstrating a significant decrease of BBB integrity. *p < 0.05, ** p < 0.01, ***p < 0.001, ****p < 0.0001 vs. control; +p < 0.05, ++p < 0.01 vs. gp120; #p < 0.05, ##p < 0.01, ###p < 0.001, ####p < 0.0001 vs. TS + gp120 co-treatment. n.s. = non statistical significance.

# CHAPTER THREE

# A QUASI-PHYSIOLOGICAL MICROFLUIDIC BLOOD-BRAIN BARRIER MODEL FOR BRAIN PERMEABILITY STUDIES

Microfluidics-based organ-on-a-chip technology allows for developing a new class of in-vitro blood-brain barrier (BBB) models that recapitulate many hemodynamic and architectural features of the brain microvasculature not attainable with conventional two-dimensional platforms. Herein, we describe and validate a novel microfluidic BBB model that closely mimics the one in situ. Induced pluripotent stem cell (iPSC)-derived brain microvascular endothelial cells (BMECs) were juxtaposed with primary human pericytes and astrocytes in a co-culture to enable BBB-specific characteristics, such as low paracellular permeability, efflux activity, and osmotic responses. The permeability coefficients of [13C12] sucrose and [13C6] mannitol were assessed using a highly sensitive LC-MS/MS procedure. The resulting BBB displayed continuous tight-junction patterns, low permeability to mannitol and sucrose, and quasi-physiological responses to hyperosmolar opening and p-glycoprotein inhibitor treatment, as demonstrated by decreased BBB integrity and increased permeability of rhodamine 123, respectively. Astrocytes and pericytes on the abluminal side of the vascular channel provided the environmental cues necessary to form a tight barrier and extend the model's long-term viability for time-course studies. In conclusion, our novel multi-culture microfluidic platform showcased the ability to replicate a quasi-physiological brain microvascular, thus enabling the development of a highly predictive and translationally relevant BBB model.

## Introduction

Central nervous system (CNS) disorders have limited treatment options, although they are significant causes of morbidity and mortality worldwide [1]. A considerable obstacle in developing CNS drug therapeutics is the BBB, restricting nearly 98% of small molecules and virtually all macromolecules from entering the brain [2]. The BBB, a unique physiological feature in vertebrates, is responsible for maintaining brain homeostasis [3,4]. Its components are BMECs, astrocytes, pericytes, neurons, and the extracellular matrix (ECM) [5]. The structural and functional unit derived from this grouping of cells and the surrounding matrix is known as the neurovascular unit (NVU) [4]. The BBB is highly selective in controlling the passage of substances between the blood and the CNS. The BMECs that line the vascular bed of the capillaries in the brain possess specialized tight junctions (TJs) that severely limit the paracellular diffusion of polar molecules and efflux pumps that allow for tight control of the transcellular passage of a large variety of lipophilic substances. These gating features allow essential nutrients and molecules to pass through, while preventing harmful substances and most drugs from entering the brain. However, substances can cross the BBB by passive diffusion, adsorptive transcytosis, and receptor- or carrier-mediated transport [6].

BBB impairment is implicated in the pathogenesis and progression of various neurological diseases [7,8,9,10]. Understanding the structural and functional aspects of the BBB assumes utmost clinical importance due to the inability of most drugs to cross the barrier. Traditionally, BBB-related studies have been performed using in vitro models by culturing different cell types individually or together across semi-permeable membranes. However, conventional models cannot recapitulate physiologically relevant conditions, such as blood flow, cell–cell interactions, and the complex three-dimensional (3D) microenvironment of the human BBB [11]. In vivo techniques and animal models have provided more definitive data regarding the BBB. However, these data may not be clinically relevant or translatable due to the interspecies differences between humans and animals [12,13]. In addition, animal studies are expensive and labor intensive and involve ethical considerations [14]. Therefore, modeling the most accurate human representation of the BBB is highly desirable.

Microfluidics-based organ-on-a-chip technology has led to the recent development of a new class of in vitro models [15,16]. These miniature systems are engineered to recreate an environment similar to the microvessels in the human brain [17]. Organs-on-chips enable dynamic growth, function, and interaction of multiple cell types, while enabling perfusion and shear stress. In addition to basic mechanistic and translational studies, microfluidics can be used for drug permeability assessments as a far more accurate alternative to the classic Transwell set-up. Due to their structural advantages, organs-on-chips are usually better for establishing in-vitro–in-vivo correlations for drug permeability measurements. Recent studies have reported the use of iPSC-derived BMECs (iBMECs) in organ-on-a-chip BBB platforms exhibiting near-physiological barrier features [4,18,19,20,21]. However, most research groups have relied on large-molecular-weight dextrans (3–70 kDa) to measure passive permeability [18,19]. This is problematic because the calculation of permeability coefficients without considering the size of the selected dextran may not effectively capture the integrity of the BBB on a chip. The permeability coefficient of dextran reported by Yuan et al. [22] using in vivo fluorescence imaging analysis has been repeatedly cited as a reference point for correlation studies. However, passive diffusion of dextran fluorescent markers crossing the BBB in vivo is highly unlikely due to its molecular weight. In fact, even most of the small-molecular-weight-drug candidates are unable to pass the BBB. As such, it is essential to use small-molecular-weight markers to validate the barrier function in these advanced BBB models. We have previously demonstrated the use of an LCMS method using sucrose (353 Da) and mannitol (187 Da) as superior alternatives for BBB permeability studies [23,24]. They possess high metabolic stability, do not interact with proteins, and are uncharged, enabling precise paracellular BBB permeability measurement [23,24,25,26,27].

This study validated the barrier function of a BBB-on-a-chip platform using [13C12] sucrose and [13C6] mannitol. We co-cultured iBMECs with primary human pericytes and astrocytes on the organ-on-a-chip model to emulate BBB-specific characteristics, such as high barrier function, low permeability, and efflux activity. We also showed that the

organ-on-a-chip model could maintain the barrier function for 1 week, whereas traditional iBMECs Transwell models can maintain the barrier function for only 2 days.

## Materials and Methods

### Cell Culture

Primary human brain astrocytes (ScienCell # 1800, Carlsbad, CA, USA) and primary human brain pericytes (Cell Systems # ACBRI 498, Kirkland, WA, USA) were grown in the recommended growth medium. Primary cells were used at passages 1–3. The iPSC (IMR90) clone cell line (Wicell # iPS(IMR90)-4, Madison, WI, USA) with passage number (40–55) was used to derive BMECs.

### iPSCs Differentiation to iBMECs

iPSCs were differentiated into iBMECs as per existing protocol [28,29]. Briefly, iPS (IMR90)-4 were grown in Essential 8 medium (Thermo Fisher Scientific # A1517001, Waltham, MA, USA) containing 10 µM Y-27632 dihydrochloride (Tocris # 1254). After cells reached 70% confluency, differentiation into iBMECs was initiated using unconditioned medium (Thermo Fisher Scientific # 11330057), 20% knockout serum replacement (Thermo Fisher Scientific # 10828010), 1% non-essential amino acids (Thermo Fisher Scientific # 11140050), 0.5% Glutamax (Thermo Fisher Scientific # 35050079), and 0.1 mM β-mercaptoethanol (Sigma-Aldrich # M6250, St. Louis, MO, USA), which continued for 6 days. Subsequently, the media were changed to EC++ media, i.e., human endothelial SFM (Thermo Fisher Scientific # 11111044) with 1% platelet-poor plasma-derived serum, bovine (Alfa Aesar # 15406419, Haverhill, MA, USA), 20 ng/mL bFGF, and 10 µM retinoic acid (Sigma-Aldrich # R2625). After 2 days, the medium was replaced with EC (SFM without bFGF and retinoic acid). The cells were harvested using Accutase (Corning # 25-058-CI, Corning, NY, USA) for seeding on a BBB on a chip.

### BBB on a Chip

We used a commercially available brain on a chip from Emulate, Inc. (Boston, MA, USA). The chip consists of a polydimethylsiloxane (PDMS)-based microfluidic device containing two overlapping microchannels (1 × 1 mm and 1 × 0.2 mm, brain and blood channel, respectively) separated by a permeable PDMS membrane [18,30,31]. The inner surface of the channels was coated with collagen (Sigma # C5533, Kawasaki, Kanagawa) and fibronectin (Sigma # F1141) solution (4:1) in distilled water and incubated overnight at 37 °C. To mimic the physiological microenvironment in the brain, primary astrocytes and pericytes were co-cultured at a 3:1 ratio in the apical channel ($1 \times 10^6$ $mL^{-1}$ and $3.5 \times 10^5$ cells $mL^{-1}$ for astrocytes and pericytes, respectively). The cells were allowed to adhere to the apical channel in the incubator for 4 h. $1.5 \times 10^7$ cells $mL^{-1}$ of iBMECs were then seeded on the basal channel, and the chip was turned upside down to allow them to adhere to the permeable PDMS membrane. The device was then turned back to

the upright position to allow the remaining iBMECs to adhere to the sides and bottom of the channel, thereby forming a capillary lumen. The flow was introduced the next day with the help of a peristaltic pump (Ismatec, Opfikon, Switzerland) at a rate of 120 µL/h. Experiments were then performed after the cells were adapted to the flow conditions.

**Permeability Measurement of Sucrose and Mannitol**

Barrier integrity of a BBB microfluidic chip was obtained by measuring the permeability coefficients of stable isotopes of [$^{13}C_{12}$] sucrose and [$^{13}C_6$] mannitol. For this purpose, 100 µg/mL of [$^{13}C_6$] mannitol and [$^{13}C_{12}$] sucrose (Omicron Biochemicals, South Bend, IN, USA) was added simultaneously to the vascular (lumen) channel. Samples were collected over specific time intervals from the apical channel (ablumen) and measured using an established UPLC-MS/MS method [23]. Briefly, the collected samples were diluted in LC-MS/MS-grade water in the standard curve range (2–1000 ng/mL). Samples were then subjected to a protein crashing step by diluting at a ratio of 1:9 in acetonitrile:water (80:20) (Fisher Scientific, USA) containing 20 ng/mL of [$^{2}H_8$] mannitol and [$^{2}H_2$] sucrose (Omicron Biochemicals, South Bend, IN, USA) as an internal standard followed by centrifugation at 12,000 rpm for 10 min. The supernatant was transferred into autosampler inserts and then injected into the LC-MS/MS. An Acquity BEH amide column (2.1 mm × 50 mm, 1.7 µm; Waters, Milford, MA, USA) was used for chromatographic separation using acetonitrile:water:ammonium hydroxide (73:27:0.1, v/v) as the mobile phase, at a flow rate of 0.2 mL/min. Electrospray ionization in negative mode was used as the ionization source, and data acquisition and quantification were made using Analyst software.

The concentration measured through LCMS were used to calculate the permeability coefficient (cm/s) as follows based on a previous study [18]:

$$P = Cr \times Va / Cd \times A \times t \quad (1)$$

Here, P is the permeability coefficient (cm/s), Cr is the measured concentration of the marker in the brain effluent at a time (t), and Cd is the measured concentration of the marker in the dosing (vascular) channel effluent at a time (t). Va is the volume of the receiving channel at a time (t). The membrane area (A) is 0.17 $cm^2$ in the microfluidic chip, and the flow rate of 120 µL/h was used for all permeability studies.

**Immunofluorescence Microscopy**

Immunocytochemistry was performed as previously described [18,29]. The channels of the BBB chip were fixed with paraformaldehyde (4% in PBS) for 10 min and then washed. Cells were permeabilized with 0.1% Triton X-100 in PBS and blocked with 10% goat serum in PBS for 30 min. The primary antibodies used to stain the cells are listed in the **Supplementary File** (Table S1). After overnight incubation, the chips were washed and stained with secondary antibodies conjugated to Alexa Fluor-488 and Alexa Fluor-

555. A confocal microscope (A1R, Nikon, NY, USA) was used to obtain the images with a 10× objective.

**Dynamic Flow and Shear Stress**

The confluent endothelial monolayer in the presence of primary human pericytes and astrocytes was exposed to intravascular medium flow using a peristaltic pump to evaluate the effects of shear stress on barrier function. Microfluidic chips were exposed to different flow rates to simulate different levels of shear stress. Initially, the flow rate was set to 120 µL/h for 1 h and then increased to 1200 and 2400 µL/h to produce higher levels of shear stress. The flow rate was maintained for 48 h. Permeability experiments and immunofluorescence were performed after 48 h of exposure to dynamic flow. The shear stress was obtained from the following equation [18], where τ is the shear stress (dyn/cm$^2$) generated in the vascular channel. Q and µ are the flow rate (µL/min) and the viscosity (Pa.s), respectively.

$$\tau = 6Q\mu/Wh^2 \quad (2)$$

The width (W) and height (h) of the vascular channels were, respectively, 1 mm and 200 µm. The viscosity of the cell culture medium was 3–4 cP after adding 3.5% dextran to the medium.

**Efflux Study of the Chip**

The P-gp functionality was evaluated using rhodamine 123 (Sigma-Aldrich), a substrate of the P-gp transporter [19,29]. Both channels were pretreated with 5 µM cyclosporine A (CsA, P-gp inhibitor, Sigma-Aldrich) for 1 h. Rhodamine 123 was added to the vascular channel and incubated in the presence or absence of cyclosporine A at a flow rate of 120 µL/h. [$^{13}C_{12}$] Sucrose (100 µg/mL) was simultaneously added to monitor the barrier integrity. Effluents were collected from the apical and basal channels and quantified using fluorescence intensity. The fluorescence was measured at 485/530 nm to quantify the rhodamine 123 concentration via a SynergyMX2 ELISA plate reader (BioTek Instruments, Winooski, VT, USA). The BBB permeability of rhodamine 123 and sucrose was measured in the presence or absence of the inhibitor.

**BBB Opening Using the Hyperosmolar Solution**

A hypertonic solution containing 25% mannitol was introduced into the vascular channel at a 120 µL/h flow rate for 10 min. Mannitol was then replaced with 100 µg/mL of [$^{13}C_{12}$] sucrose and [$^{13}C_6$] mannitol. The permeability coefficients of the markers were obtained at different time points to evaluate the BBB opening and recovery.

**Statistical Analyses**

Prism 9 (GraphPad Software, La Jolla, CA) was used for the statistical analysis of the data. At least three biological replications were used for all experiments. Student's unpaired two-tailed t-test was used for a comparison of the two groups. Data with more than two groups were analyzed by one-way ANOVA, followed by Tukey's multiple comparisons test. In all cases, a p-value $< 0.05$ was considered significant. Data were presented as the mean ± SD or individual values.

## Results

### Characterization of the Blood-Brain Barrier Microfluid Model

We performed our experiments using the commercially available brain chip (Emulate). It is an in vitro model made of clear PDMS elastomer that artificially recreates a section of the brain vasculature and its surrounding microenvironment. It consists of two superimposed microchannels with a porous membrane in between to allow a cellular interface. We activated and coated the BBB chip as per the manufacturer's instructions. iBMECs were seeded on the basal channel, and primary astrocytes and pericytes (seeding ratio of 3:1) were added to the apical channel. The iBMECs formed a confluent monolayer of tightly packed cells throughout the basal channel, representing the 3D vascular lumen. BBB-endothelial-specific markers, such as the TJ proteins zona occludens-1 (ZO-1), claudin-5, glucose transporter GLUT-1, and efflux transporter P-gp, were expressed in the channel. Figure 3.1 shows the iBMEC expression of these key markers inside the BBB on a chip. Figure S1 reveals that the iBMECs formed a continuous band of ZO-1, Glu-1, and Pg-p lining the entire luminal side, thereby forming a blood-vessel-like structure featuring an uninterrupted cellular layer. Note the 3D cross section of the BBB, also shown in Figure S1.

Astrocytes and pericytes also grew throughout the apical channel. Glial fibrillary acidic protein (GFAP) and alpha-smooth muscle actin (α-SMA) were used as fluorescent markers for astrocytes and pericytes to distinguish them (Figure 3.2) visually. The immunocytochemistry imaging of the ZO-1 distribution showed that the iBMECs formed a uniform monolayer covering the entire luminal side of the vascular channel (Figure 2A). Noteworthy is also the distribution of astrocytes and pericytes in the "brain" channel, clearly distinguishable based on the expression of GFAP and α-SMA, respectively. Observation by confocal microscopy confirmed that the iBMECs, astrocytes, and pericytes remained confined to their corresponding channels. Note also that the astrocytic endfeet extended through the permeable membrane to establish contact with the juxtapose endothelial layer in the vascular channel.

### Assessment of Paracellular Permeability across a BBB Microfluidic Chip

We assessed the passage of [$^{13}C_{12}$] sucrose and [$^{13}C_6$] mannitol, known as one of the ideal paracellular permeability markers [23,32], across iBMEC cell monolayers cultured in single and triculture models under a continuous flow condition (0.15 dyne/cm$^2$) to investigate the difference in barrier properties. Results show that the permeability of

[$^{13}C_{12}$] sucrose and [$^{13}C_6$] mannitol across the single culture of the iBMEC monolayer was $1.883 \times 10^{-6} \pm 3.763 \times 10^{-7}$ and $2.380 \times 10^{-6} \pm 5.738 \times 10^{-7}$ cm/s (n = 3 biological replicates), respectively, after 2 days in the culture, while the permeability of sucrose and mannitol in the triculture was $4.923 \times 10^{-7} \pm 1.187 \times 10^{-7}$ and $6.760 \times 10^{-7} \pm 1.071 \times 10^{-7}$ cm/s (n = 3 biological replicates), respectively (see Figure 3.3A,B). Compared with iBMECs cultured alone, a triculture with human pericytes and astrocytes significantly decreased the blood-to-brain paracellular leakage of sucrose and mannitol ($p < 0.01$ unpaired, two-tailed t-test). Accordingly, our results strongly suggest that a co-culture with primary human astrocytes and pericytes can enhance the barrier function of the BBB on a chip. Furthermore, permeability measurements were performed at 2, 5, 7, and 10 days post-setup (see Figure 3.3C,D) to assess the longitudinal viability of the microfluidic BBB system. Our data show stable BBB integrity up to 7 days, at which point, the permeability coefficients of sucrose and mannitol started increasing. For instance, the permeability coefficient of sucrose was $5.093 \times 10^{-7} \pm 5.395 \times 10^{-8}$ and $5.317 \times 10^{-7} \pm 1.628 \times 10^{-7}$ cm/s on day 2 and day 5 (n = 3 biological replicates), respectively, whereas it was $1.166 \times 10^{-6} \pm 3.277 \times 10^{-7}$ and $2.180 \times 10^{-6} \pm 3.306 \times 10^{-7}$ cm/s on day 7 and day 10 (n = 3 biological replicates), respectively. The permeability on days 2 and 5 was significantly different from that measured on day 10 ($p < 0.001$ one-way ANOVA, followed by Tukey's multiple comparisons test). A similar trend was observed when measuring mannitol permeability (n = 3), which increased from $6.640 \times 10^{-7} \pm 3.651 \times 10^{-8}$ and $6.430 \times 10^{-7} \pm 3.557 \times 10^{-8}$ on day 2 and day 5 to $3.053 \times 10^{-6} \pm 5.258 \times 10^{-7}$ on day 10 ($p < 0.0001$ one-way ANOVA, followed by Tukey's multiple comparisons test).

Previously, we reported the permeability coefficient of these markers in mouse models through IV bolus injection [23]. We observed a correlation between our current in vitro and the ones we obtained in vivo. The permeability coefficient of sucrose and mannitol in-vivo (n = 3) was $1.75 \pm 0.355 \times 10^{-8}$ and $3.71 \pm 0.296 \times 10^{-8}$ cm/s, respectively. Sucrose and mannitol (permeability coefficient values) in microfluidic chips were only 1 log magnitude higher than those assessed in vivo (Figure 3.3E).

**Effect of Microfluidic Shear Stress on BBB Integrity and Barrier Function**

We studied the effect of shear stress on BBB permeability using the microfluidic BBB chip. iBMECs and primary human pericytes and astrocytes were seeded on vascular and brain channels and allowed to attach under static (no flow) conditions for 1 day. After that, platforms were either maintained under static conditions with daily media changes or exposed to flow using a peristaltic pump at a rate of 120, 1200, or 2400 µL/h (equivalent to 0.15, 1.5, and 3 dyn/cm2) for 48 h. Based on permeability measurements, the integrity and tightness of the BBB slightly increased in the presence of flow compared to static conditions. For instance, the permeability coefficient of sucrose (n = 3 biological replicates; see Figure 3.4A, left panel) was $1.521 \times 10^{-6} \pm 4.707 \times 10^{-7}$ cm/s in static conditions without any perfusion on day 3. In contrast, the permeability values decreased to $5.093 \times 10^{-7} \pm 1.595 \times 10^{-8}$, $5.05 \times 10^{-7} \pm 1.125 \times 10^{-7}$, and $8.4 \times 10^{-7} \pm 1.931 \times 10^{-7}$ cm/s in response to the exposure to shear stress of 0.15, 1.5, and 3 dyn/cm$^2$,

respectively. Similar statistically significant results were obtained for mannitol permeability (n = 3 biological replicates), ranging from $1.105 \times 10^{-6} \pm 1.939 \times 10^{-7}$ cm/s in static conditions (see Figure 3.4A right panel) to $6.337 \times 10^{-7} \pm 1.898 \times 10^{-8}$, $5.67 \times 10^{-7} \pm 4.952 \times 10^{-8}$, and $8.713 \times 10^{-7} \pm 5.184 \times 10^{-8}$ cm/s in response to shear stress of 0.15, 1.5, and 3 dyn/cm$^2$, respectively. These results are in agreement with previous work highlighting the role of shear stress in BBB endothelial physiology [33] and support the notion that exposure to shear stress enhances the barrier tightness, resulting in lower paracellular permeability. Figure 4B shows the fluorescence image of the tight-junction protein ZO-1 and f-actin phalloidin on day 3 in static and dynamic conditions. Under static conditions, ZO-1 was localized to cell–cell junctions and showed a polygonal network, consistent with previous reports on the iBMEC monolayer [34]. There were no clear differences between ZO-1 stains under static and flow conditions, suggesting that tight-junction networks are already formed under static conditions. Additional quantitative experiments will be necessary to better understand the effect of shear stress on the tight junctions and the cytoskeleton.

Furthermore, F-actin expression indicated substantial intercellular localization in iBMEC-lined channels. The patterns exhibit the lack of cellular elongation in cells exposed to fluidic shear. This property has been reported previously to be a unique feature of iBMECs [18,34]. F-actin continued to be randomly oriented and did not align parallel to flow in all the groups.

**BBB-on-a-Chip Responds to P-gp Inhibition**

We investigated the ability of the model to replicate the efflux transporter activity and act as a metabolic barrier. P-gp is expressed on the endothelium and acts as an efflux pump to protect the brain from unwanted molecules. To study P-gp efflux inhibition, 5 μM cyclosporine A was supplemented in channels. Then the permeability of sucrose and rhodamine 123 (substrate of P-gp transporter) was evaluated in the presence or absence of the inhibitor. As shown in Figure 3.5, treatment with P-gp inhibitor cyclosporine A (CsA) increased R123 permeability from $3.677 \times 10^{-7} \pm 5.669 \times 10^{-8}$ to $7.876 \times 10^{-7} \pm 6.791 \times 10^{-8}$ cm/s (n = 3) ($p < 0.01$ unpaired, two-tailed t-test), while the permeability of sucrose was not altered by CsA ($p > 0.50$ unpaired, two-tailed t-test).

**Hyperosmolar BBB Opening**

We infused a hyperosmolar mannitol solution into the vascular channel for 10 min. We then immediately perfused the lumen with [$^{13}C_{12}$] sucrose and [$^{13}C_6$] mannitol to assess the impact of the hyperosmolar challenge on BBB integrity as a function of permeability. Figure 3.6A,B shows that the transport of markers increased to the brain channel after exposure to hyperosmolar mannitol. The permeability coefficient of sucrose increased from $6.978 \times 10^{-7} \pm 1.22 \times 10^{-7}$ cm/s pre-opening to $6.910 \times 10^{-6} \pm 2.014 \times 10^{-6}$ cm/s 1 h following the hyperosmolar challenge. A similar trend was observed for mannitol permeability (increasing from $8.253 \times 10^{-7} \pm 1.436 \times 10^{-7}$ cm/s pre-opening to $7.983 \times 10^{-6} \pm 2.398 \times 10^{-6}$ cm/s 1 h post-opening). A longitudinal assessment of paracellular

permeabilities showed that the BBB integrity started recovering at 2.5 h after the hyperosmolar challenge (PSUC = $1.840 \times 10^{-6} \pm 2.800 \times 10^{-7}$ cm/s; PMAN = $2.057 \times 10^{-6} \pm 3.099 \times 10^{-7}$ cm/s) and was fully restored at 24 h (PSUC = $8.163 \times 10^{-7} \pm 2.11 \times 10^{-7}$ cm/s; PMAN = $9.437 \times 10^{-7} \pm 2.097 \times 10^{-7}$ cm/s).

## Discussion

Small-molecular-weight markers, such as sucrose, mannitol, and sodium fluorescein, have naturally low BBB permeability; therefore, these markers have been used widely to assess the integrity of the BBB. Recently published studies have emphasized the alternative use of dextran molecules of relatively large molecular weights (3 to 70 kDa) to assess the integrity and tightness of the BBB [4,18,19]. However, large-molecular-weight markers may not accurately assess the integrity and tightness of the BBB in permeability studies involving small, drug-like molecules. In this study, we used a recently developed method that quantifies the stable isotopes of sucrose and mannitol with high sensitivity and accuracy for measuring BBB integrity [23]. Sucrose and mannitol may be considered the most widely accepted markers for the precise measurement of paracellular BBB permeability in vivo due to their unique characteristics, such as being uncharged and remaining largely unbound from proteins. Therefore, we characterized the structure and barrier function of a novel BBB microfluidic chip established using human iBMECs with or without the presence of additional NVU components, including astrocytes and pericytes. We noticed that the model maintained the barrier function for at least 7 additional days, enabling time-course studies of biologically and clinically relevant variations. [13C12] sucrose and [13C6] mannitol permeability values in a microfluidic chip were $4.923 \times 10^{-7} \pm 1.187 \times 10^{-7}$ and $6.760 \times 10^{-7} \pm 1.071 \times 10^{-7}$ cm/s (see Figure 3A,B), respectively, which were quite close to their corresponding values recorded in vivo [23].

The barrier function of some recently published iPSC-based BBB microfluidic models was reported to be comparable to in vivo values [17,18,21,32]. These data were obtained by correlating the permeability coefficients of dextran in these models against rat pial post-capillaries using imaging studies [22]. The permeability coefficient values of dextran (4–70 kDa) in rat pial post-capillaries were reported in the range of 1 to $9 \times 10^{-7}$ cm/s. For instance, the permeability coefficient of 10 kDa dextran was shown to be $3.1 \times 10^{-7}$ cm/s in rat cerebral microvessels. A drawback of such imaging techniques is the lack of quantitative uptake measurement and vessel damage resulting from the grounding of the skull. As a result, these techniques could lead to the overestimation of dextran permeability levels. Studies, for example, by Mehvar et al., have demonstrated that even with 4 kDa dextran, there is no fluorescein-labeled dextran concentration in brain tissue [35]. Similarly, Linville et al. also developed an advanced BBB microvessel, demonstrating that 10 kDa dextran does not pass across the BBB and that the permeability is below the detection limit [21].

We also found that a co-culture with human pericytes and astrocytes significantly decreases the permeability values of sucrose and mannitol compared to iBMECs alone.

This finding exemplifies the notion that our multi-culture model provides a realistic cellular environment for the iBMECs to form a viable and effective BBB in vitro. Vatine et al. and Park et al. found similar results when comparing the permeability of 3 kDa dextran in a monoculture and a triculture in microfluidic chips [18,19]. Moreover, Park et al. found that the mRNA levels of ZO-1, VE-cadherin, and MRP1 are remarkably higher in iBMECs when co-cultured with brain astrocytes and pericytes on a chip [19].

The morphology of iBMECs is not changed in the presence of laminar flow, which indicates that these cells do not elongate and align as a response to shear stress. Furthermore, immunofluorescence images of tight junctions show similar patterning and expression levels, implying that laminar flow is unnecessary for iBMECs to establish a tight barrier. DeStefano et al. confirmed that shear stress does not induce any changes in the expression of several BBB markers at the protein or gene level [34], whereas Vatine et al. showed that ZO-1 gene expression is increased in all laminar flow conditions, including low shear stress (0.01 dyn/cm$^2$) [18]. We confirmed that shear stress decreases the permeability values of mannitol and sucrose. The effect is not drastic but still statistically significant when compared to static conditions. These findings are in agreement with DeStefano et al.'s conclusions, which suggests that iBMECs can establish a barrier function under static conditions, but also are in agreement with previous studies from our group supporting a positive barrier modulatory role of shear stress [33]. However, additional studies will be required to determine the environmental contribution of astrocytes and/or pericytes to the iBMECs expression and distribution of the TJs and further confirm the role of shear stress in the process since results from prior studies using iBMECs have yielded controversial results [18,34,36]. In addition, whether and to what degree the observed phenomenon applies to primary BMEC under similar multi-culture conditions will need to be determined. Human brain microvascular endothelial cells (HBMECs) in the presence of shear stress demonstrate upregulation of tight and adherens junction proteins and the development of a more stringent (high TEER values) barrier compared to static conditions [33].

iBMECs in a monoculture exhibit many human BBB properties, including well-organized tight junctions, polarized efflux transporter activity, and high TEER values (1000–3000 Ω·cm$^2$). However, a significant limitation of these cells hindering their usability for targeted CNS drug delivery and time-course studies is the short-lived BBB viability, which is maintained for about 2 days [29,37]. Our study clearly showed that using a dynamic multi-culture setting encompassing astrocytes, pericytes, and intraluminal flow can further extend the barrier viability up to 5–7 days.

Systemic intravenous injection of the hyperosmolar agent mannitol is used clinically to reduce cerebral edema in acute conditions [38]. In contrast, at a high concentration (25% w/v), bolus intra-arterial injection of mannitol results in endothelial cell shrinkage, leading to a transient opening of the BBB [39,40,41]. Hyperosmolar BBB opening has been used in clinical and translational settings to facilitate the delivery of chemotherapeutics, stem cells, and viral vectors into the brain [40,42,43]. Herein, we tested the response of our BBB-on-a-chip model to similar osmotic challenges. Following

a 10 min infusion of a bolus 25% mannitol, we recorded an eightfold increase in $^{13}[C_{12}]$ sucrose permeability, which closely mimics previous results obtained by our group in vivo using a mouse model undergoing transient BBB opening by hyperosmolar mannitol [44]. Four hours post-hyperosmolar opening, the integrity of the BBB was restored, as indicated by sucrose and mannitol permeability measurement (see Figure 6). Our data are in line with previous results from Linville et al. reporting that hyperosmolar mannitol causes transient focal leaks that result in a significant permeability increase of Lucifer yellow and 10 kDa dextran [21,45]. They also confirmed the recovery of barrier integrity 3 h post-infusion [45]. Higher penetration of both 10 kDa dextran and the cetuximab antibody into the brain channel was also reported by Park et al. in response to the osmotic opening of the BBB in a microfluidic chip. Within 4 h post-opening, the permeability of dextran and the antibody declined to the normal (pre-opening) range, indicating a recovery of the barrier integrity [19].

ATP-binding cassette efflux transporters, including P-glycoprotein (P-gp), limit the penetration of many lipophilic compounds into the brain parenchyma by actively transporting them out of the brain [45]. Hence, modulation of efflux transporters plays a crucial role in controlling CNS drug delivery. Accordingly, numerous reports have demonstrated that iBMECs possess active efflux activity as determined by substrate inhibition assays [19,21,29,37]. Here, we sought to characterize this efflux activity in a 3D microfluidic chip. The permeability of rhodamine 123 (a P-gp substrate) was evaluated in the presence or absence of cyclosporin A (a P-gp inhibitor) in iBMECs. Cyclosporine A is a P-gp inhibitor used in human studies to assess P-gp activities [46,47]. We showed that the permeability of R123 increases by about twofold, while the barrier's paracellular permeability to sucrose remains unaltered. These results indicate that our microfluidic model can reproduce a crucially important feature of the BBB affecting the passage of drugs into the brain, thus playing a significant role in determining drug permeability tests' predictive value and reliability. Additional testing will be required to further assess the viability of other major efflux transporters, including BCRP and MRP1, and more permeability testing using clinically relevant CNS drugs with known permeability coefficients will be required to better assess the predictive value of our model.

**Conclusions and Future Studies**

This study validated the barrier function of a human iPSC-derived blood-brain barrier microfluidic chip by using small-molecular-weight markers. Sucrose and mannitol are known as ideal standard markers for the measurement of BBB integrity in in vivo studies. We showed low permeability coefficient values for [13C12] sucrose and [13C6] mannitol in the microfluidic model. The BBB microfluidic model displays critical tight-junction proteins, an efflux pump, and transporters. Moreover, the physiological barriers were maintained until day 7, which could be used for any chronic disease studies. We also demonstrated successful modulation of both transcellular and paracellular permeability using the P-gp inhibitor and hyperosmolar agent mannitol. Our results suggest that the multi-culture microfluidic model can effectively reproduce a quasi-physiological

microenvironment, allowing for developing a highly predictive and translationally relevant BBB model. This novel platform can be a valuable tool for screening putative CNS-targeting drugs and assess the feasibility and effectiveness of novel delivery methods across the BBB.

## REFERENCES


1. Lozano, R.; Naghavi, M.; Foreman, K.; Lim, S.; Shibuya, K.; Aboyans, V.; Abraham, J.; Adair, T.; Aggarwal, R.; Ahn, S.Y.; et al. Global and regional mortality from 235 causes of death for 20 age groups in 1990 and 2010: A systematic analysis for the Global Burden of Disease Study 2010. Lancet 2012, 380, 2095–2128. [Google Scholar] [CrossRef]
2. Pardridge, W.M. Blood-brain barrier delivery. Drug Discov. Today 2007, 12, 54–61. [Google Scholar] [CrossRef] [PubMed]
3. Kadry, H.; Noorani, B.; Cucullo, L. A blood-brain barrier overview on structure, function, impairment, and biomarkers of integrity. Fluids Barriers CNS 2020, 17, 69. [Google Scholar] [CrossRef] [PubMed]
4. Bhalerao, A.; Sivandzade, F.; Archie, S.R.; Chowdhury, E.A.; Noorani, B.; Cucullo, L. In vitro modeling of the neurovascular unit: Advances in the field. Fluids Barriers CNS 2020, 17, 22. [Google Scholar] [CrossRef] [PubMed]
5. Abbott, N.J.; Patabendige, A.; Dolman, D.E.; Yusof, S.R.; Begley, D.J. Structure and function of the blood-brain barrier. Neurobiol. Dis. 2010, 37, 13–25. [Google Scholar] [CrossRef] [PubMed]
6. Grabrucker, A.; Ruozi, B.; Belletti, D.; Pederzoli, F.; Forni, F.; Vandelli, M.A.; Tosi, G. Nanoparticle transport across the blood brain barrier. Tissue Barriers 2016, 4, e1153568. [Google Scholar] [CrossRef] [PubMed]
7. Zivadinov, R.; Alexander, S.J.; Minagar, A. Vascular pathology of multiple sclerosis. Neurol. Res. 2012, 34, 735–737. [Google Scholar] [CrossRef]
8. Marchi, N.; Granata, T.; Ghosh, C.; Janigro, D. Blood-brain barrier dysfunction and epilepsy: Pathophysiologic role and therapeutic approaches. Epilepsia 2012, 53, 1877–1886. [Google Scholar] [CrossRef]
9. Brouns, R.; De Deyn, P. The complexity of neurobiological processes in acute ischemic stroke. Clin. Neurol. Neurosurg. 2009, 111, 483–495. [Google Scholar] [CrossRef]
10. Sweeney, M.; Sagare, A.P.; Zlokovic, B.V. Blood-brain barrier breakdown in Alzheimer disease and other neurodegenerative disorders. Nat. Rev. Neurol. 2018, 14, 133–150. [Google Scholar] [CrossRef]
11. Van Der Helm, M.W.; van der Meer, A.; Eijkel, J.C.; Berg, A.V.D.; Segerink, L.I. Microfluidic organ-on-chip technology for blood-brain barrier research. Tissue Barriers 2016, 4, e1142493. [Google Scholar] [CrossRef] [PubMed]
12. Perrin, S. Preclinical research: Make mouse studies work. Nature 2014, 507, 423–425. [Google Scholar] [CrossRef]
13. Pamies, D.; Hartung, T.; Hogberg, H.T. Biological and medical applications of a brain-on-a-chip. Exp. Biol. Med. 2014, 239, 1096–1107. [Google Scholar] [CrossRef] [PubMed]
14. Huh, D.; Torisawa, Y.-S.; Hamilton, G.A.; Kim, H.J.; Ingber, D.E. Microengineered physiological biomimicry: Organs-on-chips. Lab Chip 2012, 12, 2156–2164. [Google Scholar] [CrossRef]
15. Zheng, F.; Fu, F.; Cheng, Y.; Wang, C.; Zhao, Y.; Gu, Z. Organ-on-a-Chip Systems: Microengineering to biomimic living systems. Small 2016, 12, 2253–2282. [Google Scholar] [CrossRef]
16. Bhise, N.S.; Ribas, J.; Manoharan, V.; Zhang, Y.S.; Polini, A.; Massa, S.; Dokmeci, M.R.; Khademhosseini, A. Organ-on-a-chip platforms for studying drug delivery systems. J. Control. Release 2014, 190, 82–93. [Google Scholar] [CrossRef] [PubMed]
17. Kaisar, M.A.; Sajja, R.K.; Prasad, S.; Abhyankar, V.; Liles, T.; Cucullo, L. New experimental models of the blood-brain barrier for CNS drug discovery. Expert Opin. Drug Discov. 2017, 12, 89–103. [Google Scholar] [CrossRef] [PubMed]
18. Vatine, G.D.; Barrile, R.; Workman, M.; Sances, S.; Barriga, B.K.; Rahnama, M.; Barthakur, S.; Kasendra, M.; Lucchesi, C.; Kerns, J.; et al. Human iPSC-derived blood-brain barrier chips enable disease modeling and personalized medicine applications. Cell Stem Cell 2019, 24, 995–1005.e6. [Google Scholar] [CrossRef]

19. Park, T.-E.; Mustafaoglu, N.; Herland, A.; Hasselkus, R.; Mannix, R.; Fitzgerald, E.A.; Prantil-Baun, R.; Watters, A.; Henry, O.; Benz, M.; et al. Hypoxia-enhanced Blood-Brain Barrier Chip recapitulates human barrier function and shuttling of drugs and antibodies. Nat. Commun. 2019, 10, 2621. [Google Scholar] [CrossRef]
20. Oddo, A.; Peng, B.; Tong, Z.; Wei, Y.; Tong, W.Y.; Thissen, H.; Voelcker, N.H. Advances in microfluidic blood-brain barrier (BBB) models. Trends Biotechnol. 2019, 37, 1295–1314. [Google Scholar] [CrossRef]
21. Linville, R.M.; DeStefano, J.G.; Sklar, M.B.; Xu, Z.; Farrell, A.M.; Bogorad, M.I.; Chu, C.; Walczak, P.; Cheng, L.; Mahairaki, V.; et al. Human iPSC-derived blood-brain barrier microvessels: Validation of barrier function and endothelial cell behavior. Biomaterials 2018, 190–191, 24–37. [Google Scholar] [CrossRef]
22. Yuan, W.; Lv, Y.; Zeng, M.; Fu, B.M. Non-invasive measurement of solute permeability in cerebral microvessels of the rat. Microvasc. Res. 2009, 77, 166–173. [Google Scholar] [CrossRef]
23. Noorani, B.; Chowdhury, E.A.; Alqahtani, F.; Ahn, Y.; Patel, D.; Al-Ahmad, A.; Mehvar, R.; Bickel, U. LC-MS/MS-based in vitro and in vivo investigation of blood-brain barrier integrity by simultaneous quantitation of mannitol and sucrose. Fluids Barriers CNS 2020, 17, 61. [Google Scholar] [CrossRef]
24. Chowdhury, E.A.; Alqahtani, F.; Bhattacharya, R.; Mehvar, R.; Bickel, U. Simultaneous UPLC-MS/MS analysis of two stable isotope labeled versions of sucrose in mouse plasma and brain samples as markers of blood-brain barrier permeability and brain vascular space. J. Chromatogr. B Analyt. Technol. Biomed. Life Sci. 2018, 1073, 19–26. [Google Scholar] [CrossRef]
25. Alqahtani, F.; Chowdhury, E.A.; Bhattacharya, R.; Noorani, B.; Mehvar, R.; Bickel, U. Brain uptake of [13C] and [14C] sucrose quantified by microdialysis and whole tissue analysis in mice. Drug Metab. Dispos. 2018, 46, 1514–1518. [Google Scholar] [CrossRef] [PubMed]
26. Miah, M.K.; Chowdhury, E.A.; Bickel, U.; Mehvar, R. Evaluation of [14C] and [13C] sucrose as blood-brain barrier permeability markers. J. Pharm. Sci. 2017, 106, 1659–1669. [Google Scholar] [CrossRef] [PubMed]
27. Miah, M.K.; Bickel, U.; Mehvar, R. Development and validation of a sensitive UPLC-MS/MS method for the quantitation of [13C] sucrose in rat plasma, blood, and brain: Its application to the measurement of blood-brain barrier permeability. J. Chromatogr. B Analyt. Technol. Biomed. Life Sci. 2016, 1015–1016, 105–110. [Google Scholar] [CrossRef][Green Version]
28. Nozohouri, S.; Noorani, B.; Al-Ahmad, A.; Abbruscato, T.J. Estimating brain permeability using in vitro blood-brain barrier models. Methods Mol. Biol. 2021, 2367, 47–72. [Google Scholar] [CrossRef]
29. Lippmann, E.S.; Al-Ahmad, A.; Azarin, S.M.; Palecek, S.P.; Shusta, E.V. A retinoic acid-enhanced, multicellular human blood-brain barrier model derived from stem cell sources. Sci. Rep. 2014, 4, 4160. [Google Scholar] [CrossRef] [PubMed]
30. Sances, S.; Ho, R.; Vatine, G.; West, D.; Laperle, A.; Meyer, A.; Godoy, M.; Kay, P.S.; Mandefro, B.; Hatata, S.; et al. Human iPSC-derived endothelial cells and microengineered organ-chip enhance neuronal development. Stem Cell Rep. 2018, 10, 1222–1236. [Google Scholar] [CrossRef]
31. Jain, A.; Barrile, R.; Van der Meer, A.; Mammoto, A.; Mammoto, T.; De Ceunynck, K.; Aisiku, O.; Otieno, M.; Louden, C.; Hamilton, G.; et al. Primary human lung alveolus-on-a-chip model of intravascular thrombosis for assessment of therapeutics. Clin. Pharmacol. Ther. 2018, 103, 332–340. [Google Scholar] [CrossRef]
32. Kadry, H.; Noorani, B.; Bickel, U.; Abbruscato, T.J.; Cucullo, L. Comparative assessment of in vitro BBB tight junction integrity following exposure to cigarette smoke and e-cigarette vapor: A quantitative evaluation of the protective effects of metformin using small-molecular-weight paracellular markers. Fluids Barriers CNS 2021, 18, 28. [Google Scholar] [CrossRef]
33. Cucullo, L.; Hossain, M.; Puvenna, V.; Marchi, N.; Janigro, D. The role of shear stress in Blood-Brain Barrier endothelial physiology. BMC Neurosci. 2011, 12, 40. [Google Scholar] [CrossRef] [PubMed]
34. DeStefano, J.G.; Xu, Z.S.; Williams, A.J.; Yimam, N.; Searson, P.C. Effect of shear stress on iPSC-derived human brain microvascular endothelial cells (dhBMECs). Fluids Barriers CNS 2017, 14, 20. [Google Scholar] [CrossRef] [PubMed]
35. Mehvar, R.; Robinson, M.A.; Reynolds, J.M. Molecular weight dependent tissue accumulation of dextrans: In vivo studies in rats. J. Pharm. Sci. 1994, 83, 1495–1499. [Google Scholar] [CrossRef]

36. Faley, S.L.; Neal, E.H.; Wang, J.; Bosworth, A.M.; Weber, C.; Balotin, K.M.; Lippmann, E.S.; Bellan, L.M. iPSC-derived brain endothelium exhibits stable, long-term barrier function in perfused hydrogel scaffolds. Stem Cell Rep. 2019, 12, 474–487. [Google Scholar] [CrossRef] [PubMed]
37. Lippmann, E.S.; Azarin, S.M.; E Kay, J.; A Nessler, R.; Wilson, H.K.; Alahmad, A.; Palecek, S.P.; Shusta, E.V. Derivation of blood-brain barrier endothelial cells from human pluripotent stem cells. Nat. Biotechnol. 2012, 30, 783–791. [Google Scholar] [CrossRef]
38. Diringer, M.N. New trends in hyperosmolar therapy? Curr. Opin. Crit. Care 2013, 19, 77–82. [Google Scholar] [CrossRef]
39. Koopaei, N.N.; Chowdhury, E.A.; Jiang, J.; Noorani, B.; Da Silva, L.; Bulut, G.; Hakimjavadi, H.; Chamala, S.; Bickel, U.; Schmittgen, T.D. Enrichment of the erythrocyte miR-451a in brain extracellular vesicles following impairment of the blood-brain barrier. Neurosci. Lett. 2021, 751, 135829. [Google Scholar] [CrossRef]
40. Gonzales-Portillo, G.S.; Sanberg, P.R.; Franzblau, M.; Gonzales-Portillo, C.; Diamandis, T.; Staples, M.; Sanberg, C.D.; Borlongan, C.V. Mannitol-enhanced delivery of stem cells and their growth factors across the blood-brain barrier. Cell Transplant. 2014, 23, 531–539. [Google Scholar] [CrossRef]
41. Rapoport, S.I. Osmotic opening of the blood-brain barrier: Principles, mechanism, and therapeutic applications. Cell. Mol. Neurobiol. 2000, 20, 217–230. [Google Scholar] [CrossRef]
42. Joshi, S.; Ergin, A.; Wang, M.; Reif, R.; Zhang, J.; Bruce, J.N.; Bigio, I. Inconsistent blood brain barrier disruption by intraarterial mannitol in rabbits: Implications for chemotherapy. J. Neuro Oncol. 2010, 104, 11–19. [Google Scholar] [CrossRef]
43. Foley, C.P.; Rubin, D.G.; Santillan, A.; Sondhi, D.; Dyke, J.; Gobin, Y.P.; Crystal, R.G.; Ballon, D. Intra-arterial delivery of AAV vectors to the mouse brain after mannitol mediated blood brain barrier disruption. J. Control. Release 2014, 196, 71–78. [Google Scholar] [CrossRef]
44. Löscher, W.; Potschka, H. Blood-brain barrier active efflux transporters: ATP-binding cassette gene family. NeuroRX 2005, 2, 86–98. [Google Scholar] [CrossRef] [PubMed]
45. Linville, R.M.; DeStefano, J.G.; Sklar, M.B.; Chu, C.; Walczak, P.; Searson, P.C. Modeling hyperosmotic blood-brain barrier opening within human tissue-engineered in vitro brain microvessels. J. Cereb. Blood Flow Metab. 2019, 40, 1517–1532. [Google Scholar] [CrossRef] [PubMed]
46. Muzi, M.; Mankoff, D.A.; Link, J.M.; Shoner, S.; Collier, A.C.; Sasongko, L.; Unadkat, J.D. Imaging of cyclosporine inhibition of P-glycoprotein activity using 11C-verapamil in the brain: Studies of healthy humans. J. Nucl. Med. 2009, 50, 1267–1275. [Google Scholar] [CrossRef]
47. Sasongko, L.; Muzi, M.; Mankoff, D.A.; Yang, X.; Collier, A.C.; Link, J.M.; Shoner, S.C.; Unadkat, J.D. Imaging P-glycoprotein transport activity at the human blood-brain barrier with positron emission tomography. Clin. Pharmacol. Ther. 2005, 77, 503–514. [Google Scholar] [CrossRef] [PubMed]

FIGURES

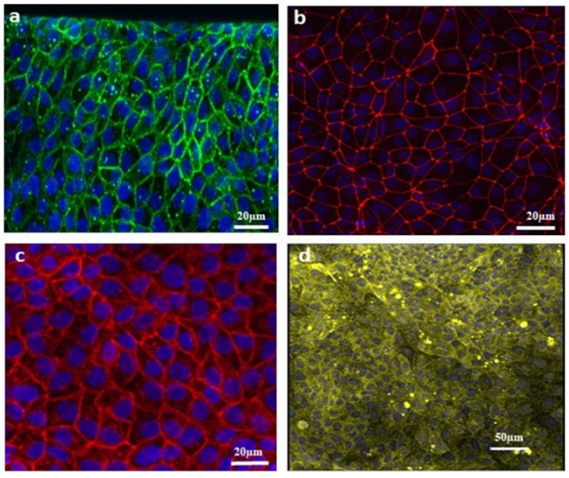

Fig. 1. Immunofluorescence images presenting key markers of iBMECS microfluidic chip on day 3, a) claudin-5, (b) ZO-1, (c) Glucose transporter-1 (GLUT1), (d) P-glycoprotein (P-gp) Nuclei visualized with DAPI (blue).

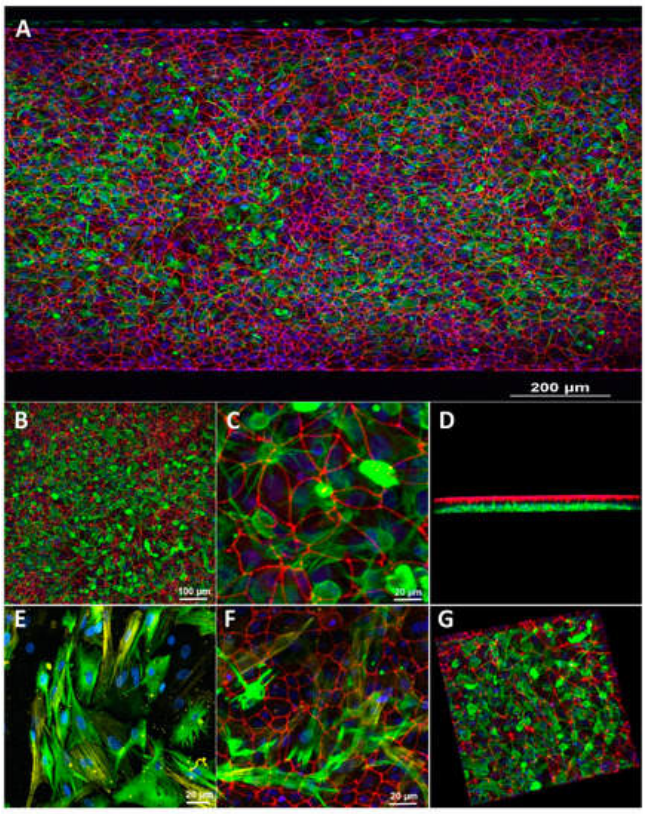


Fig. 2. Immunofluorescence images demonstrating the co-culture and triculture of the BBB on a chip. iBMECs cultured on all surfaces of the blood channel, and primary human brain pericytes and astrocytes on the apical brain channel. (A–C) Different magnifications of iBMECs stained with ZO-1 (red); iBMECs form a tight barrier on the blood side; astrocytes were stained with GFAP (green). (D,G) 3D structure of the co-culture. (E) Co-culture staining of primary human astrocytes (GFAP, green) and primary human pericytes (α-SMA, yellow) in the brain channel. (F) Triculture staining of the BBB on a chip (red, iBMECs-ZO-1; green, astrocytes (GFAP); yellow, pericytes (α-SMA)).

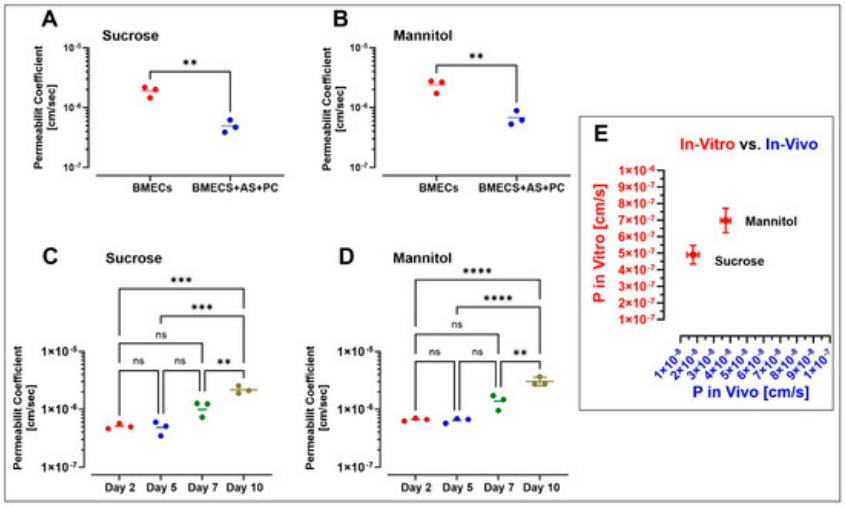


Fig. 3. The permeability coefficient of sucrose (A) and mannitol (B) in BBB on a chip with iBMECs alone and iBMECs with primary human astrocytes and pericytes cultured under continuous flow (0.15 dyne/cm2) for 2 days. Student's t-test ($p < 0.01$); n = 3 biological replicates. Long-term stability of the barrier function by a comparison of the permeability coefficients of sucrose (C) and mannitol (D) on different days under continuous flow (0.15 dyne/cm2). ** $p < 0.01$, *** $p < 0.001$, and **** $p < 0.0001$, assessed by one-way ANOVA, followed by Tukey's multiple comparisons test (n = 3 biological replicates). (E) Comparison of sucrose and mannitol permeability assessed in our BBB microfluidic model with previously reported in vivo data in mice (n = 3 biological replicates).

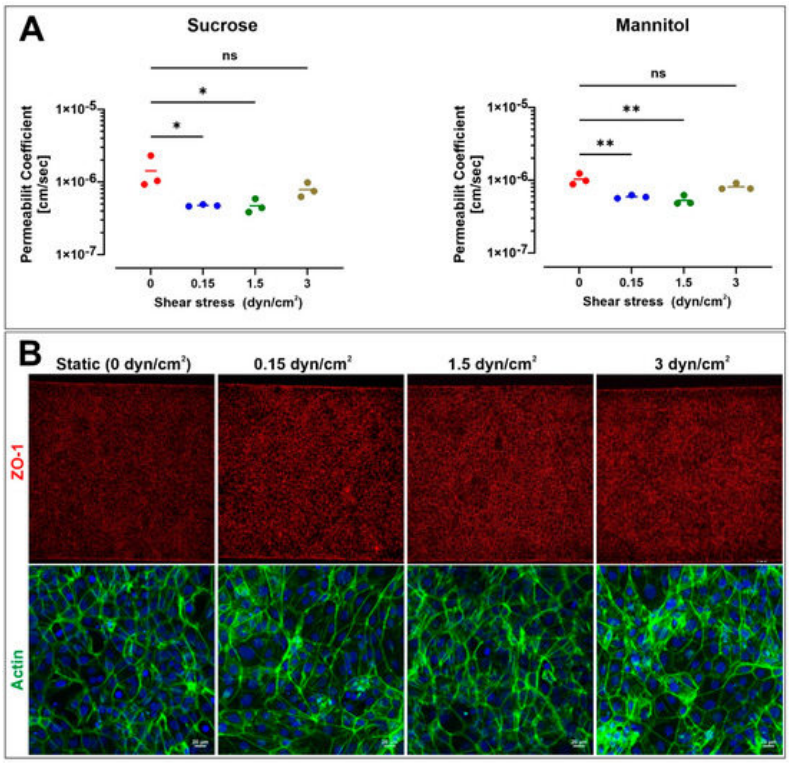


Fig. 4. Effect of shear stress on the permeability coefficient of sucrose and mannitol in a microfluidic chip. (A) Note the effect of shear stress on the permeability of both paracellular markers. (B) Representative immunofluorescence images of iBMEC monolayers fixed and stained after 48 h at 0, 0.15, 1.5, and 3

dyne/cm2. ZO-1 (red) and F-actin phalloidin (green). n = 3 biological replicates. * $p < 0.05$ and ** $p < 0.001$ assessed by one-way ANOVA, followed by Tukey's multiple comparisons test.

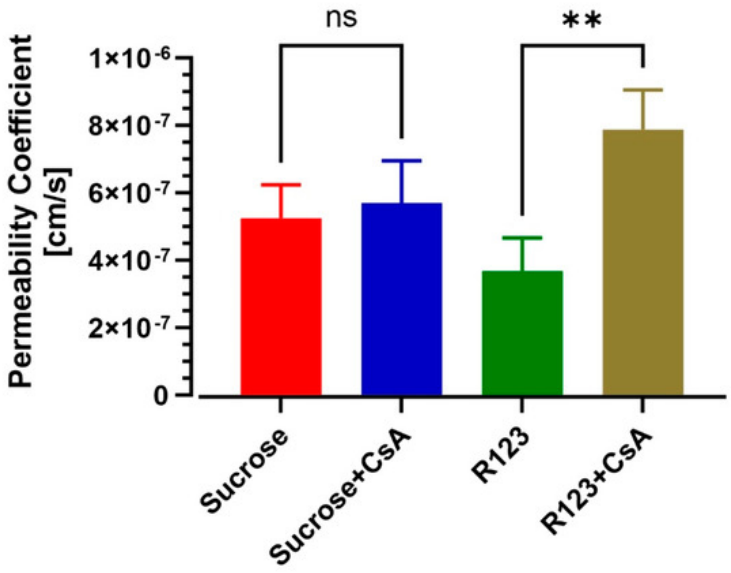


Fig. 5. Assessment of efflux transporter functionality of iBMECs in BBB on a chip with and without cyclosporine A treatment. Note the permeability coefficient of rhodamine 123 (substrate of P-gp transporter) and sucrose in the presence or absence of the P-gp inhibitor (n = 3 biological replicates). ** $p < 0.01$, assessed by one-way ANOVA, followed by Tukey's multiple comparisons test.

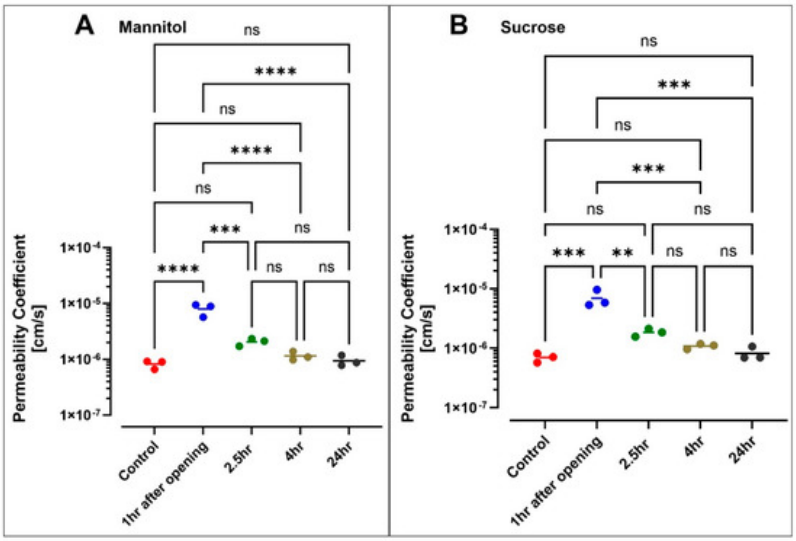


Fig. 6. Evaluation of the barrier integrity of the BBB chip after exposure to hyperosmolar mannitol for 10 min. Monitoring the permeability of sucrose (A) and mannitol (B) over a 24 h window after exposure to hyperosmolar mannitol revealed a significant increase in their respective permeability values at 1 h post-opening. Sucrose and mannitol permeability then returned progressively to normal over the 24 h period (n = 3 biological replicates). ** $p < 0.01$, *** $p < 0.001$, and **** $p < 0.0001$ assessed by one-way ANOVA, followed by Tukey's multiple comparisons tests.

CHAPTER FOUR

# ASSAY DEVELOPMENT FOR EVALUATING NANOCARRIER PERMEABILITY ACROSS AN IN VITRO BLOOD–BRAIN BARRIER MODEL

## Introduction

The blood-brain barrier (BBB) is arguably the most significant consideration for brain drug delivery technologies. This highly specialized, multilayer cellular interface separates the systemic circulation from the brain parenchyma and serves to maintain homeostasis by selectively regulating molecular transport. While the BBB facilitates the uptake of essential nutrients required for neuronal activity, it simultaneously restricts the influx of potentially harmful xenobiotics, toxins, and most pharmacological agents. Consequently, nearly 100% of large molecule biologics and approximately 98% of small molecules fail to cross an intact BBB [1, 2].

Drug nanocarriers (NCs) have been explored as delivery vehicles to improve CNS penetration. However, unmodified NCs generally do not cross the non-disrupted BBB. To address this limitation, surface functionalization with so-called “Trojan horse” ligands, typically receptor-specific peptides, viral proteins, or monoclonal antibodies (mAbs), has emerged as a promising strategy [3]. These ligands engage endogenous transport pathways within the brain capillary endothelium, enabling nanocarrier trafficking across the BBB via either absorptive-mediated transcytosis (AMT) or receptor-mediated transcytosis (RMT) [4]. While AMT approaches exploiting cationic ligands, they often result in undesirable endothelial sequestration and toxicity. RMT has therefore become the preferred mechanism for BBB-targeted delivery. Over the past three decades, Trojan horse nanocarriers have been investigated in both in vitro and in vivo models, employing diverse platforms such as liposomes [4, 5], gold nanoparticles, synthetic polymer nanoparticles, and virus-like particles [6]. Despite this extensive research, no nanocarrier formulations have yet achieved FDA approval for CNS indications [3], highlighting the pressing need for improved preclinical models and translational strategies. DNA nanocarriers have recently gained interest as a versatile class of delivery vehicles with potential advantages in programmability, biocompatibility, and payload flexibility [6]. To accelerate innovation in this field, there is a critical requirement for robust in vitro BBB assays that can accurately predict nanocarrier transport properties before advancing to animal models. Transwell-based BBB models, while simplified relative to in vivo conditions, offer a scalable and reproducible platform for assessing permeability under controlled conditions. This chapter describes the systematic development of a transwell-based BBB permeability assay optimized for the evaluation of ligand-functionalized DNA nanocarriers and related nanoplatforms. In this study, the nanocarriers were synthesized by a collaborating laboratory and functionalized with receptor-specific ligands designed to engage receptor-mediated transcytosis pathways at the BBB. Our role was to establish and validate an in vitro assay capable of sensitively and reproducibly

quantifying their permeability across a physiologically relevant BBB model. Specifically, we tested assay detection limits, transport kinetics, transwell membrane and coating conditions, and implemented rigorous quality control (QC) steps such as TEER monitoring, live-cell imaging, and microscopy to rule out membrane entrapment artifacts. Together, these efforts establish a reproducible framework for nanocarrier permeability studies and lay the foundation for subsequent in vivo validation.

## Materials and Methods

### Nanocarrier Preparation and Labeling

DNA nanocarriers were synthesized by a collaborating laboratory. These nanocarriers were surface-functionalized with ligands designed to engage specific receptor-mediated transcytosis pathways within brain endothelial cells. Nanocarriers were subsequently labeled with fluorescent dyes to enable quantitative detection. Serial dilutions of labeled nanocarriers were prepared to generate calibration curves and define the detection range on the fluorescence plate reader. Experimental controls included non-functionalized nanocarriers, dye-only solutions, and small-molecule tracers with known permeability profiles.

### In Vitro BBB Model in Transwell Format

Mouse brain microvascular endothelial cells (BMECs) were seeded at an optimized density of $1 \times 10^5$ cells/cm² on the apical side of collagen-coated polyester transwell inserts (0.4 μm pore size, 6.5 mm diameter). Cells were maintained at 37°C with 5% $CO_2$, with daily media changes, until TEER measurements stabilized, indicating the formation of a tight, confluent monolayer. 3 kDa fluorescein-dextran was applied to the donor compartment, and fluorescence in the receiver compartment was measured to confirm low paracellular flux. Monolayer confluence and tight junction formation were verified using immunofluorescence staining for ZO-1 and claudin-5.

### Assay Development and Optimization

*Nanocarrier Reconstitution and Initial Quantification* - The DNA nanocarriers were received from collaborators in lyophilized form and were reconstituted in 1.2 mL of nuclease-free water, yielding an approximate concentration of 10 μM. To confirm the concentration, nanocarriers were quantified using a NanoDrop spectrophotometer (A260 nm). Molar concentration was calculated by dividing the absorbance at 260 nm by the extinction coefficient of Cy5-labeled nanocarriers (197,900 $M^{-1}cm^{-1}$), as shown below:

$$Concentration\ (\mu M) = (A260 / 197{,}900)\ X\ 10^6$$

This calculation verified that the reconstituted stock was ~10 μM, which was then used as the starting concentration for assay calibration.

**Establishing the Detection Limit**

To determine the sensitivity of the assay, a calibration curve was generated using serial dilutions of Cy5-labeled DNA nanocarriers. The stock solution was diluted into serum-free media to prepare a 10-point series starting from 10μM with a blank control. Fluorescence was measured on a plate reader, and the resulting curve confirmed a linear relationship between nanocarrier concentration and Cy5 fluorescence intensity across this range. Initial attempts at detection using a 20 nm bandwidth for excitation/emission failed to yield measurable signal, suggesting that the broad spectral window contributed to background interference. To improve resolution, narrower bandwidths were systematically tested. At 5, 7.5, and 10 nm, signal intensity improved markedly, with the 5 nm setting providing the most stable and reproducible readings.

**Time-Course Kinetics of Permeability**

To identify the optimal sampling window for permeability experiments, a cell-free permeability assay was first established using 6.5mm Transwell® inserts with 0.4μm pore polyester membranes. Cy5-labeled DNA nanocarriers were diluted in serum-free media to a working concentration of 0.6μM and applied to the donor (apical) compartment of the Transwell system. The initial assay volumes were as follows: 200μL in the top (donor) chamber and 600 μL in the bottom (receiver) chamber. At each sampling time point (ranging from 15 minutes to 48 hours), a 50μL aliquot was collected from the receiver chamber for quantification by plate reader. To maintain constant hydrostatic pressure and receiver volume, each 50μL sample withdrawal was immediately replaced with 50 μL of pre-warmed fresh media. At the final 48-hour time point, a 50 μL sample was also collected from the donor chamber to assess the remaining concentration of nanocarriers in the apical compartment. All samples were collected in triplicate, and fluorescence was measured under optimized detection conditions (5 nm bandwidth).

**Influence of Transwell Membrane Material and Coating**

The material and surface treatment of transwell membranes were systematically tested, as both can influence cell attachment, barrier integrity, and nonspecific binding of nanocarriers. Polyester and polycarbonate membranes were compared, each with a variety of extracellular matrix coatings, including collagen IV and fibronectin. Morphological assessment and baseline permeability measurements revealed that collagen-coated polyester membranes provided the most consistent endothelial monolayer formation, while also minimizing nonspecific nanocarrier adherence. These findings guided the standardization of membrane conditions for all further studies.

**Assessing Nanocarrier Entrapment on Membranes**

An additional concern in transwell assay is the possibility of nanocarrier entrapment or adsorption within the membrane itself, which could confound apparent permeability measurements. To address this, transwell membranes were imaged post-experiment using fluorescence microscopy and confocal z-stacks. These analyses revealed modest retention of nanocarriers within certain membrane types, emphasizing the need to carefully control for this effect. Based on these findings, baseline correction for membrane retention was incorporated into the data analysis pipeline.

**Permeability of Non-Targeting Nanocarriers**

To establish baseline permeability, Cy5-labeled non-targeting DNA nanocarriers were applied to confluent brain endothelial cell monolayers cultured on Transwell inserts. Permeability of non-targeting nanocarriers was assessed using 6.5 mm collagen-coated polyester transwell inserts (0.4 μm pore size) under two conditions: cell-seeded and no-cell controls. Mouse brain microvascular endothelial cells (BMECs) were seeded on the apical surface at a density of $1 \times 10^5$ cells/cm². Monolayer integrity was confirmed by trans endothelial electrical resistance (TEER >150 Ω·cm² after blank subtraction) and nanocarriers were added to the apical chamber in serum-free media, while the basolateral chamber contained fresh media. Samples from the basolateral chamber were collected at predetermined time intervals. Fluorescence intensity of Cy5 was measured using a microplate reader. Apparent permeability coefficients (Papp) were calculated according to the standard equation.

**Results**

**Establishing the Detection Limit**

The calibration curve confirmed a linear relationship between Cy5 nanocarrier concentration and fluorescence intensity across the tested range (10–0.0195 μM). Initial measurements using a 20 nm bandwidth failed to yield detectable signals, likely due to high background noise. Narrower bandwidths enhanced resolution, with the 5 nm setting producing the most stable and reproducible signal. Under these optimized conditions, the assay achieved reliable detection down to 0.001 μM, establishing the lower limit of detection (LOD) (Fig. 4.1). For subsequent permeability assays, a working concentration of 0.6 μM was selected to ensure robust signal intensity while minimizing potential artifacts associated with higher concentrations.

**Time-Course Kinetics of Permeability**

A gradual increase in Cy5 tagged nanocarrier fluorescence was observed in the basolateral (receiver) compartment over time, accompanied by a corresponding decrease in the apical (donor) compartment (Figure 4.2). Cy5 signal became detectable in the receiver chamber after approximately one hour, indicating the onset of transport across the membrane. The rate of accumulation in the receiver compartment remained slow, with fluorescence levels approaching equilibrium only after more than 48 hours. These

results demonstrate that Cy5 transport across the Transwell membrane occurs primarily through passive diffusion in cell-free transwells, reflecting limited permeability and slow equilibration kinetics under the tested conditions.

**Quality Control of Barrier Integrity**

Robust barrier integrity was confirmed using multiple complementary approaches. TEER measurements were collected daily to monitor the establishment and of a tight barrier, with only cultures exceeding threshold resistance values ≥150–200 $\Omega \cdot cm^2$ included in downstream experiments. Immunostaining of tight junction markers like ZO-1 and claudin-5 was performed and confocal microscopy was employed to assess endothelial morphology and confluence, revealing intact monolayers (Fig. 4.3). These quality control measures ensured that permeability data reflected active transport across an intact barrier rather than passive leakage through compromised cultures. We also observed challenges related to membrane composition and pore size. Given DNA's propensity to absorb onto certain polymer surfaces, we hypothesized that the polyester membranes may restrict transport through nonspecific binding effects. To address this, future experiments are planned to use uncoated polyethylene terephthalate (PET) membranes with a larger pore size (1 μm), which may improve construct passage and provide a more permissive platform for transport studies.

**Baseline Permeability of Non-Targeting Nanocarriers**

To establish baseline transport characteristics, non-targeting nanocarrier formulations (NC-1 and NC-2) were evaluated in the Transwell system. Both formulations showed minimal transfer of Cy5 signal from the apical (donor) to the basolateral (receiver) compartment over 48 hours (Figure 4.4). Fluorescence in the donor chamber remained largely constant, while only a marginal increase was detected in the receiver chamber. Calculated permeability coefficients were $3.55 \times 10^{-7}$ cm/s for NC-1 and $8.03 \times 10^{-7}$ cm/s for NC-2, indicating limited diffusion across the membrane. These values define the baseline permeability for subsequent comparison with targeted nanocarrier formulations to assess the impact of targeting on transwell transport efficiency.

**Permeability of Targeted Nanocarriers**

To evaluate the influence of targeting on blood–brain barrier (BBB) transport, six nanocarrier (NC) variants were subsequently tested under identical conditions. Compared to the non-targeting controls, most targeted formulations demonstrated substantial increases in Cy5 signal transfer across the Transwell membrane, with permeability enhancements ranging from 29% to 294%. These findings indicate that the inclusion of targeting ligands significantly improved BBB penetration efficiency. Notably, one NC variant did not exhibit permeability beyond baseline control levels, suggesting that ligand specificity and surface modification play critical roles in determining transport performance

## Discussion

Through systematic optimization, we developed a transwell-based BBB permeability assay that balances reproducibility with physiological relevance. By first confirming the detection sensitivity, we ensured that the assay was capable of measuring low-abundance nanocarrier flux. Time-course analysis defined an optimal experimental window, while membrane comparison highlighted the importance of material and coating in supporting barrier formation and minimizing artifacts. Incorporation of QC measures such as TEER and live-cell imaging safeguarded against spurious results due to barrier disruption, and microscopy confirmed that apparent transport was not confounded by entrapment within the transwell membrane.

This study evaluated the permeability of receptor-targeted nanocarriers across an in vitro BBB model and demonstrated that peptide functionalization substantially enhanced nanocarrier transport relative to non-targeted controls. Importantly, the data highlights both the promise of receptor-mediated strategies and the influence of carrier backbone properties on overall transport efficiency.

Together, these optimizations created a workflow that is sensitive, reproducible, and adaptable for comparative testing of nanocarrier formulations. Nonetheless, limitations remain. Transwell systems lack the dynamic flow and shear stress present in vivo and therefore may underestimate the complexity of BBB transport mechanisms. Future iterations of this work may benefit from transitioning to microfluidic organ-on-chip platforms, where physiological flow conditions and multicellular interactions can be more faithfully reproduced.

## Conclusion

The assay development process outlined in this chapter yielded a validated transwell-based BBB permeability assay suitable for evaluating nanocarrier transport. By systematically interrogating detection, kinetics, membrane properties, and barrier integrity, we established a protocol that minimizes artifacts and maximizes reproducibility. This platform provides a foundation for screening novel nanocarrier systems and serves as a bridge toward more advanced dynamic BBB models in subsequent studies.

## Future Directions

To further substantiate the observed transport differences and elucidate underlying mechanisms, several follow-up experiments are planned. Inhibitor-based validation studies will be conducted using known receptor or transporter blockers (e.g., TfR, CD98hc inhibitors) to confirm the specificity of nanocarrier-mediated BBB transport. Complementary binding and uptake assays, including ELISA, flow cytometry, confocal microscopy, and TEM, will quantify receptor engagement and distinguish surface binding

from active transcytosis. Orthogonal readouts such as live-cell imaging and endosomal tracking will be incorporated to visualize intracellular trafficking pathways. To establish translational relevance, in vitro permeability results will be correlated with in vivo brain/plasma distribution data, and cross-species benchmarking using both human and mouse BMECs will be performed. Collectively, these studies aim to validate transport mechanisms and enhance predictive modeling of nanocarrier performance across the BBB.

## REFERENCES


1. Pardridge, W.M., The blood-brain barrier: bottleneck in brain drug development. NeuroRx, 2005. **2**(1): p. 3-14.
2. Tong, X., et al., Blood–brain barrier penetration prediction enhanced by uncertainty estimation. Journal of Cheminformatics, 2022. **14**(1): p. 44.
3. Pardridge, W.M., Advanced Blood-Brain Barrier Drug Delivery. Pharmaceutics, 2022. **15**(1).
4. Wu, D., et al., The blood–brain barrier: Structure, regulation and drug delivery. Signal Transduction and Targeted Therapy, 2023. **8**(1): p. 217.
5. Pardridge, W.M., Brain delivery of nanomedicines: trojan horse liposomes for plasmid DNA gene therapy of the brain. Frontiers in Medical Technology, 2020. **2**: p. 602236.
6. Luo, Q., et al., Utilization of nanotechnology to surmount the blood-brain barrier in disorders of the central nervous system. Materials Today Bio, 2025. **31**: p. 101457.

FIGURES

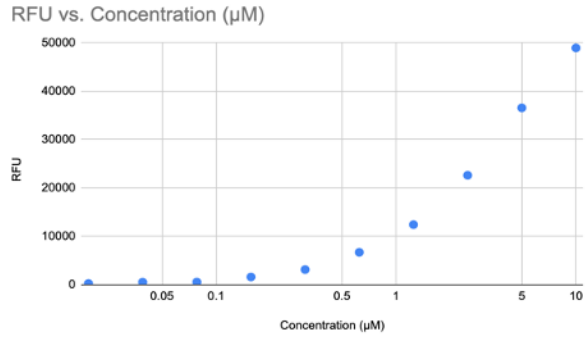


Figure 1: LOD determined at ~0.01 µM, where fluorescence intensity becomes indistinguishable from blank

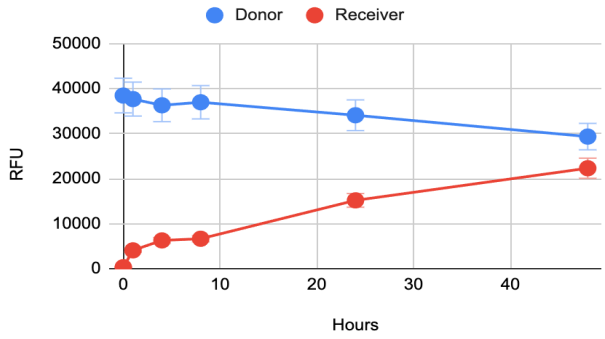


Figure 2: Kinetics of Cy5-labeled nanocarrier transport across the cell free Transwell system.
Cy5-labeled nanocarriers were added to the apical (donor) chamber and fluorescence in the basolateral (receiver) chamber was measured at defined time points (0, 6, 12, 24, and 48 h). Fluorescence intensity (RFU) decreased slightly in the donor chamber while progressively increasing in the receiver chamber, indicating gradual transfer across the membrane. Cy5 signal was first detected in the receiver chamber after approximately 1 h, with equilibration requiring more than 48 h, consistent with slow passive diffusion across the Transwell.

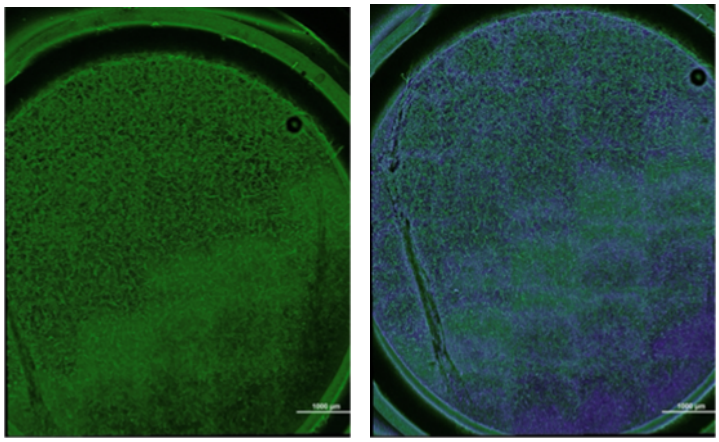

Figure 3. Confocal microscopy verification of confluent BMEC monolayers and Cy5-labeled nanocarrier distribution. Confocal imaging was performed to confirm monolayer integrity and assess nanocarrier

localization on brain microvascular endothelial cells (BMECs). Tight junction protein ZO-1 (green) delineates continuous cell borders, confirming the formation of a confluent barrier. Cy5-tagged nanocarriers (magenta) are visible on the cell surface, indicating association with the endothelial monolayer. Scale bar = 100 µm.

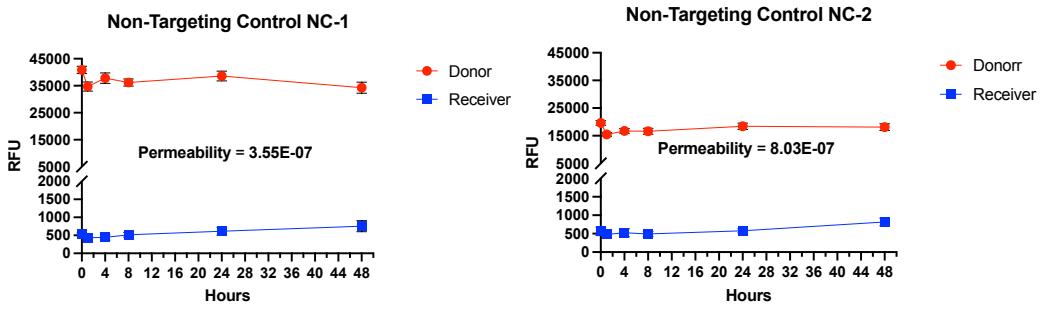


Figure 4. Baseline permeability of non-targeting nanocarrier formulations (NC-1 and NC-2) across BMEC monolayers. Non-targeting Cy5-labeled nanocarriers (NC-1 and NC-2) were evaluated in the Transwell system to establish baseline permeability. Fluorescence intensity (RFU) was measured in the apical (donor) and basolateral (receiver) chambers over 48 hours. Both formulations showed minimal Cy5 transfer, indicating limited passive diffusion across the endothelial monolayer. Calculated apparent permeability coefficients (P_app) were $3.55 \times 10^{-7}$ cm/s for NC-1 and $8.03 \times 10^{-7}$ cm/s for NC-2. Data represent mean ± SD from n = 6 biological replicates per group.